Universidad del Valle

Trabajo de Grado

Simulación de las propiedades de un sistema unidimensional de bosones de espín-1 en presencia de un acople espín-órbita utilizando Matrix Product States

Simulation of the properties of a one-dimensional spin-1 bosonic system in presence of spin-orbit coupling by means of Matrix Product States

Trabajo de grado como requisito parcial para optar al título de Físico

Presentado por

Andres Felipe Galindo Salgado

galindo.andres@correounivalle.edu.co

Dirigido por

Dr. rer. Nat. Karen Cecilia Rodríguez Ramírez

Facultad de Ciencias Naturales y Exactas

Departamento de Física-3146

2025

To my mom, father, grandfather and sisters.

Agradecimientos

Este trabajo es el fruto de un esfuerzo profundo por comprender y explorar el mundo que me rodea. Ha sido un largo camino, lleno de altibajos y desafíos que han representado un enorme reto. A lo largo de este año, este proyecto ha sido testigo de mi transformación personal y profesional, marcando un nuevo grado de madurez tanto como físico como ser humano. Nada de esto hubiese sido posible sin el apoyo incondicional de las personas que me rodean, quienes han sido una pieza clave en la formulación y culminación de este trabajo de grado.

Desde el inicio, conté con la guía invaluable de mi directora, Karem Rodríguez, quien, además de ser una excelente profesional, es una persona excepcional. Siempre estuvo dispuesta a acompañarme en este proceso, y estoy profundamente agradecido por las innumerables charlas que compartimos, las cuales me ayudaron a superar obstáculos tanto académicos como personales. La mentoría de alguien como Karem es una experiencia que todo estudiante de pregrado debería vivir.

Mi familia ha sido mi motivación y la fuente de mis más profundos deseos de superación. Agradezco a mi madre, Claudia, por su apoyo constante y por aligerar la carga durante este arduo proceso de convertirme en físico; a mi padre, Jorge, por sus sabios consejos y por ayudarme a ser cada día una mejor persona; a mi hermana, Diana, por las conversaciones enriquecedoras, su aporte en la elección del estilo visual de este trabajo y su compañía incondicional; y a mi tía Patricia y su familia, por su apoyo constante. Mi familia es parte inherente de mi ser y los llevo siempre presentes, dondequiera que vaya.

También quiero expresar mi gratitud a mis amigos y compañeros de carrera: Sebastián Moreno, Ferney Jiménez, Santiago Olave, Juanito, Argiro Garro, Camilo Revelo y Carlos Rodallega, quienes enriquecieron este trabajo con sus opiniones, discusiones y sugerencias. Ellos son para mí una fuente de inspiración, y me siento orgulloso de haber compartido estos años junto a ellos. Agradezco enormemente a mi mejor amigo Sebastián Gómez, por acompañarme siempre en esta larga (y a veces dolorosa) aventura; él es una de las grandes motivaciones por las que sigo luchando por mis sueños.

Es imposible mencionar a todas las personas que me han acompañado en este camino en una sola página. Sin embargo, la esencia de mi gratitud no se limita a estas palabras: cada gesto, cada conversación y cada instante compartido ha dejado una huella imborrable en mi vida.

Finalmente, dedico este trabajo a la memoria de mi abuelo Emilio, quien partió tan solo dos semanas antes de la culminación de este gran logro. Su recuerdo permanecerá siempre conmigo.

Resumen

En este trabajo, desarrollado en el marco teórico detrás de los Matrix Product States (*MPS*) y Matrix Product Operators (*MPO*) con un enfoque en su implementación numérica en un lenguaje de programación de bajo nivel como lo es **C++**, tiene como resultado una librería que integra ambos métodos para computar eficientemente observables locales, correladores y operadores no triviales que involucran múltiples sitios, tales como los hamiltonianos que incluyen términos de Hopping o de interacción. La implementación es general y puede ser empleada para una variedad de sistemas. En este trabajo se hace el planteamiento teórico de un sistema conformado por un arreglo unidimensional de bosones de espín-1 en el régimen superfluido, descrito por el hamiltoniano de Bose-Hubbard en presencia de un acoplamiento espin-orbita efectivo (SOC) modelado por un campo magnético externo. Expresar el sistema en la base del operador $\hat{S}_y$ para alinear el sistema con la orientación del campo externo introduce una nueva base de estados helicoidales, haciendo emerger propiedades físicas novedosas cuyo estudio es de interés en el campo de los átomos ultra-fríos. Adicionalmente se implementan las técnicas de *MPS* y *MPO* en el estudio del modelo de Heisenberg cuadrático y un sistema de spin-$\frac{1}{2}$ sujeto a interacción espín-órbita como prueba preliminar para la futura implementación en el sistema de spin-1 en el régimen superfluido.

El análisis de estados base de múltiples sistemas dentro de distintos regímenes de parámetros provee información física relevante a través de correlaciones, operadores locales y energías de estado base, permitiendo indagar en los detalles característicos de cada una de las fases y modelos estudiados.

Este trabajo demuestra que la inclusión del formalismo del *MPO* a la técnica convencional del *MPS* permite representar de manera eficiente operadores no triviales que exhiben diferentes rangos de complejidad, todo esto mientras se reduce el coste computacional de las simulaciones. Este formalismo abre direcciones prometedoras para futuros desarrollos, incluyendo algoritmos paralelizados de time evolution block decimation *(TEBD)* y protocolos de contracción optimizados para sistemas de mayor dimensión.

Palabras Clave: Acoplamiento espín-órbita, hamiltoniano de Bose-Hubbard, Matrix Product States, Matrix Product Operators, Tensor Networks, espín-1.

Abstract

In this work, we develop the theoretical framework of Matrix Product States (*MPS*) and Matrix Product Operators (*MPO*) with a focus on their numerical implementation in a low level programming language as **C++**. The outcome is a library that integrates both methods to efficiently compute local observables, correlation functions, and non-trivial operators involving multiple sites such as Hamiltonians with hopping and interaction terms. The implementation is general and can be applied to a variety of systems. In this work we propose the theoretical description of a system formed by a one-dimensional array of spin-1 bosons in the superfluid regime, described by the Bose-Hubbard Hamiltonian in presence of an effective spin orbit coupling (*SOC*) modeled by an external magnetic field. Expressing the system in the $\hat{S}_y$ basis to align the system with the external field orientation introduces a new basis of helical states with novel physical properties of interest in the ultra-cold atom field. In addition, we implement the *MPS* and *MPO* techniques for studying the bilinear-biquadratic Heisenberg model and a spin-$\frac{1}{2}$ system in presence of spin-orbit coupling as a preliminary test for the future implementation in the spin-1 system in the superfluid regime.

The analysis of ground states across different systems within different parameter regimes provides detailed physical insights into correlations, local operators and ground-state energies, enabling to delve into the characteristic details of each of the phases and models employed.

Overall, this works demonstrates that the inclusion of the *MPO* formalism to the conventional *MPS* techniques enables to efficiently represent non-trivial operators exhibiting different ranges of complexity, all this while reducing the computational effort of the simulations. This framework opens promising directions for future developments, including parallelized time evolution block decimation (*TEBD*) algorithms and optimized contraction protocols for higher-dimensional systems.

Key words: Bose-Hubbard Hamiltonian, spin orbit coupling, Matrix Product States, Matrix Product Operators, Tensor Networks, spin-1.

Contents

Chapter 1

Introduction

The early 20th century marked a profound shift in the field of physics with the emergence of quantum mechanics, a revolutionary framework that introduced a whole new set of counter-intuitive interpretations for microscopic phenomena. Concepts such as superposition [1], quantum entanglement [2] and wave-particle duality [3] reshaped our understanding of the physical world and challenged the classical perspective that had prevailed for centuries. Within this emerging paradigm, in 1925, physicist Albert Einstein and Satyendra N. Bose proposed the theoretical existence of a novel phase of matter constituted by a system of bosonic atoms occupying the lowest quantum state when cooled at ultra-low temperatures [4]. This new quantum state, now known as the Bose-Einstein condensate (BEC), exhibits collective behavior attributable to that of a single "super atom" due to the overlapping of the individual wavefunctions.

Despite the early theoretical insights, the condensate had to wait some years for the advancement of atomic manipulation techniques. It was until 1995 when it was experimentally realized for the first time using gases of rubidium [5] and sodium [6] isotopes by the American physicists E. Cornell and C. Wieman, at JILA, and Wolfgang Ketterle at MIT respectively. Cornell and Wieman were able to prepare rubidium atoms at 170 nK through laser cooling techniques [7] such as Doppler cooling [8], and magnetic traps [9] with evaporative cooling [10]. This breakthrough earned them the Nobel prize in physics in 2001 and marked the foundation of the field of ultra-cold atom physics, which continues to thrive and evolve, offering a highly controllable platform for exploring quantum many-body phenomena [11].

The advances on laser control techniques made by V.S. Lethokov [12] and his group in 1968 lead to the first experimental realization of optical lattices [13], generated by means of the interference of counter-propagating lasers. The experimental possibility of loading ultra-cold atoms into spatially periodic lattices provided a clean and tunable environment in which ultra-cold atoms can be arranged in crystal-like structures [14], enabling analogies with solid-state systems [15] and allowing the study of relevant phenomena such as quantum phase transitions [16], correlations [17], and emergent collective behavior [18].

In recent years, there has been growing interest in studying novel quantum phases of matter, such

as topologically ordered phases [19] or quantum spin liquids [20]. A widely used approach to model these systems involves the formulation of simplified theoretical models that retain the relevant physical features. One such example is the Hubbard model [21], originally formulated for fermionic particles [22]. Its bosonic analogue [21], the Bose–Hubbard model [22], plays a central role in the study of strongly correlated bosons in optical lattices.

The Bose-Hubbard model describes a system of interacting bosons confined in a one dimensional harmonic potential treated within the tight-binding approximation [15]. In this framework, particles have the possibility to interact when occupying the same site and are allowed to tunnel to adjacent sites [23], both processes governed by competitive parameters. The interplay between these two parameters gives rise to a rich phase diagram [24], most notably featuring the superfluid [25] and Mott insulator phases. The quantum phase transition [16] between these two regimes was first experimentally observed by Markus Greiner and collaborators in 2002 [26], marking a turning point in the study of ultra-cold atomic systems. This breakthrough also catalyzed the development of quantum simulators [27], an emerging field in quantum physics that aims to simulate quantum mechanical properties of complex systems through highly controllable experimental platforms. Examples include ultra-cold atomic gases [28], polar molecules [29], superconducting circuits [30], photonic systems [31], and trapped ions [32], which allow precise tuning of internal parameters such as currents, interaction strengths, and spin. Within this context, spinorial systems, in which each atom possess internal spin degrees of freedom, offer a rich structure to study novel quantum phases of matter and properties of magnetically ordered states. Of particular current interest are the systems with spin-orbit coupling [33], in which an external magnetic field [34] or a laser configuration can mimic relativistic effects that allows to study new topological matter properties and interesting novel quantum features exhibited exclusively in this types of systems [35].

However, finding analytical solutions for these kind of models still remains a challenge due to the exponential growth of the Hilbert space with the system size [23] and the presence of additional internal degrees of freedom as spin. This motivates the use of complex analytical approaches [36, 37, 38], numerical methods [39, 40, 41] and computational tools [40]. In this context, the development of the Density Matrix Renormalization Group (*DMRG*) by Steven R. White in 1992 [39], combined with the earlier diagrammatic tensor formalism introduced in 1971 by Roger Penrose [42], laid in the foundation of the new branch of tensor networks methods. In 2004, Frank Verstraete and Ignacio Cirac developed the theory of Matrix Product States (*MPS*) [43] for one dimensional spin systems, enabling efficient classical simulations of quantum spin chains [44].

The field of tensors networks has been in constant expansion since its foundation, with major contributions including Guifré Vidal's work on methods for simulating systems with periodical boundary conditions [45] and Román Orús research, which in 2014 introduced tensor networks theories of symmetries, holography [46] and entanglement [47], with applications in quantum systems simulations. These developments have extended the applicability of tensor network methods to fields such as quantum machine learning and data compression [48], broadening their relevance beyond the boundaries of physics.

The main goal of this work is to implement the Matrix Product Operator (*MPO*) formalism together with the Matrix Product State (*MPS*) representation in a low-level programming language (**C++**). This approach exploits the efficiency of tensor network methods to address the exponential growth of the Hilbert space, enabling a compact description of complex operators such as the Hamiltonian and substantially reducing the computational cost of calculations including expectation values, imaginary-time evolution, and variational algorithms optimizations due to the site-invariant form introduced with the *MPO*.

However, it is important to note that the efficiency of the *MPS* formalism is not universal. The *MPS* approach provides an efficient description for systems whose correlations are compatible with a low-entanglement, 1-D structure (such as the ground states of gapped local Hamiltonians) while systems with strong or long-range entanglement may require different approaches.

This work is organized as follows: In Chapter 2 we introduce models such as the spinless Bose-Hubbard Hamiltonian describing particles trapped in a one dimensional harmonic potential within the superfluid regime. Then we introduce the spin degree of freedom, where we include an effective spin-orbit coupling modeled by a spin-dependent hopping strength parameter, which, after a rotation transformation on the system introduces a new basis of helical states used for describing relevant properties of our system, such as magnetization. There is complementary material related to the theoretical details of the derivations of the model in second quantization and the rotation transformation contained in Appendices A and B. Chapter 3 presents an introduction to the field of tensor networks, focusing specifically in the formalism of Matrix Product States (*MPS*) and Operators (*MPO*), describing all the theoretical background and advantages of this formulations for simulating many-body one-dimensional systems, specifying important processes such as local observables expectation values, norm of a state and non-local correlations. Further details on the theoretical insight of the *MPS* formalism are contained in Appendix C. Chapter 4 constitutes the core of the present work, setting the numerical implementation of the *MPS* and *MPO*, following a

low-level programming language compatible logic and introducing all the numerical equivalents of the theoretical background presented in Chapter 3, centering on the algorithms and optimization in the computational handling. In Chapter 4 we present the results of measurements of local and non-local observables in multiple ground states. Finally, in Chapter 5 a general review is presented together with general conclusions and perspectives on future applications.

Chapter 2

Many-body spin models

This research focuses aims to study a one-dimensional system of reticular spin-1 bosons in presence of a synthetic spin-orbit coupling *(SOC)* with a magnetic field oriented in the y-axis. First we introduce the spinless Bose-Hubbard model from first to second quantization, subsequently adding the spin degree of freedom, which introduces charge and spin scattering processes when particles interact with each other, finally we focus on the effect of the *SOC* in the dispersion relation in momentum space, performing the previous transformation to $\hat{S}_y$ basis in absence of interactions. All this deep inside the superfluid phase regime where the system displays its collective behavior.

We start this chapter by introducing the spinless Bose-Hubbard model by writing its Hamiltonian in second quantization formalism, then focusing on the phases that govern the physics of the system, introducing relevant concepts such as spin preserving and spin changing collisions. Later on, we make an introduction of the synthetic spin-orbit coupling, expressing the system in terms of a new transformed basis, which will set the environment for the future work related to the *MPS* and *MPO* formalisms.

2.1 Spinless Bose-Hubbard Model

Spinless bosonic particles arranged in a periodic potential via an optical trap are well described by the Bose-Hubbard Hamiltonian, which form in first quantization is expressed as

$$\hat{H}_{BH} = \sum_{i=1}^{N} \left(\underbrace{\frac{\hat{p}_i^2}{2m}}_{\textbf{(1)}} + \underbrace{\hat{V}_{\text{lat}}(x_i)}_{\textbf{(2)}} + \underbrace{\sum_{j \neq i}^{N} \hat{V}_{\text{int}}(x_i - x_j)}_{\textbf{(3)}} \right), \tag{2.1}$$

where **(1)** represents the kinetic energy of the particles, **(2)** the lattice periodic potential and **(3)** the interaction potential given by $V_{\text{int}}(x_i - x_j) = g\,\delta(x_i - x_j)$. Second quantization formalism is optimal for the treatment of this kind of many body systems. Defining our field operators in terms of the Wannier functions, $W_i(x)$, which forms a single-particle basis, and the bosonic creation ($\hat{b}_i^\dagger$) and annihilation ($\hat{b}_i$) operators obeying the commutation relation $\left[\hat{b}_i, \hat{b}_j^\dagger\right] = \delta_{i,j}$, at the i-th

site:

$$\hat{\Psi}^\dagger(x) = \sum_i W_i^*(x)\,\hat{b}_i^\dagger \quad \text{and} \quad \hat{\Psi}(x) = \sum_i W_i(x)\,\hat{b}_i, \tag{2.2}$$

with the Wannier functions given by the following expression:

$$W_j(x) = \frac{1}{\sqrt{L}} \sum_k e^{-ijkR/\hbar}\phi_k(x), \tag{2.3}$$

where L is the lattice site number, R the lattice parameter, $\phi_k(x)$ the Bloch functions, and k the quasi-momenta taking values in the first Brillouin zone. Wannier functions obey the orthogonality relation

$$\int dx\; W_i^*(x) W_j(x) = \delta_{ij}. \tag{2.4}$$

Hence the field operators adhere to the following commutation relations:

$$\left[\hat{\Psi}_i^\dagger(x), \hat{\Psi}_i^\dagger(x')\right] = \left[\hat{\Psi}_i(x), \hat{\Psi}_i(x')\right] = 0, \quad \left[\hat{\Psi}_i(x), \hat{\Psi}_j^\dagger(x')\right] = \delta_{ij}\,\delta(x-x').$$

The interaction between particles can be appropriately modeled as pair collisions at the s-wave lowest energy orbital, with all the information being contained in the scattering length a that quantifies the interaction strength [49]. Consequently the g parameter present in the interaction strength of Eq. [2.1] is given by $g = \frac{4\pi\hbar^2 a}{m}$, being m the reduced mass of the particles. We can calculate the Hamiltonian in second quantization using the constructed field operators:

$$\hat{H} = \int dx\; \hat{\Psi}_i^\dagger(x) \left(-\frac{\hbar^2\nabla^2}{2m} + V_{\text{lat}}(x)\right) \hat{\Psi}_j(x) + \frac{g}{2}\int dx\; dx' \hat{\Psi}_i^\dagger(x)\hat{\Psi}_j^\dagger(x')\delta(x-x')\hat{\Psi}_k(x')\hat{\Psi}_l(x). \tag{2.5}$$

Finally, considering the tight-binding approximation due to the Wannier functions localization in position space, the Hamiltonian is expressed as follows:

$$\hat{H} = \underbrace{-J\sum_i \left(\hat{b}_i^\dagger \hat{b}_{i+1} + \hat{b}_{i+1}^\dagger \hat{b}_i\right)}_{\textbf{(1)}} + \underbrace{\frac{U}{2}\sum_i \hat{n}_i(\hat{n}_i - 1)}_{\textbf{(2)}} \underbrace{-\mu\sum_i \hat{n}_i}_{\textbf{(3)}}, \tag{2.6}$$

where **(1)** describes the tunneling of bosons between neighboring sites with probability J, often referred to as hopping strength. This term is the same for all lattice sites and is given by the

expression derived from the second quantization transformation:

$$-J = \int dx\ W_i^*(x) \left(-\frac{\hbar^2 \nabla^2}{2m} + V_{\text{lat}}(x) \right) W_j(x). \tag{2.7}$$

The restriction of the hopping term to nearest neighbors arises from the strong spatial localization of the Wannier functions. As long as the overlap between Wannier functions beyond adjacent sites is negligible, this approximation for the hopping term is well justified.

Analogously, **(2)** in Eq. (2.6) represents the contact interaction, where $\hat{n}_i = \hat{b}_i^\dagger \hat{b}_i$ is the number operator at the i-th site. The parameter U quantifies the interaction strength, and is given by

$$U = \frac{g}{2} \int dx\ |W(x)|^4, \tag{2.8}$$

where we have considered all Wannier functions with different indices at the same site due to the predominance of the intra-atomic interaction (U_{iiii}) compared to the inter-atomic (U_{ijkl}) interaction, as a consequence of the tight-binding approximation.

Finally, **(3)** in Eq. (2.6) is included to allow the system to adjust the number of particles in order to minimize its energy, resulting in a grand canonical ensemble. Parameter μ is the chemical potential, which controls the average number of particles in the system.

2.2 System phases

Contrary to classical systems, quantum systems exhibit fluctuations even at zero temperatures due to Heisenberg's uncertainty relation, this can lead to phase transitions inducing macroscopic changes in the system [50]. The Bose-Hubbard model Eq. (2.1) is characterized by two competing parameters, the hopping strength (J), which characterizes the tunneling of bosons between neighboring lattice sites, and the interaction term (U), quantifying the repulsive ($U > 0$) or attractive ($U < 0$) atom-atom interactions. It is common to rescale the parameters in terms of U, i.e. $\bar{J} = {}^{J}/_{U}$, such that the variation of the competitive parameters leads to a phase transition of the system. We identify a division between two well characterized regimes, namely the Mott-insulator ($U >> J$) and the Superfluid ($U << J$) phases, which are represented in Fig. (2.1).

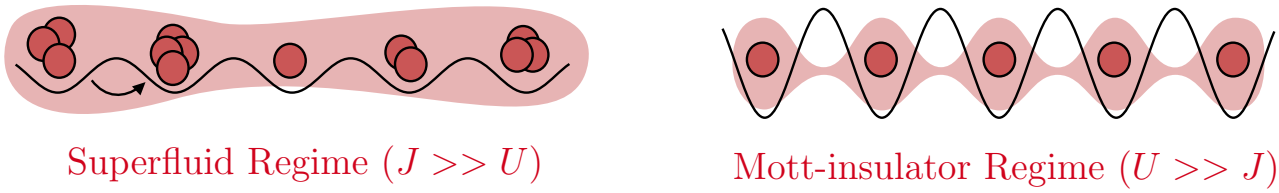

Superfluid Regime ($J >> U$) Mott-insulator Regime ($U >> J$)

Figure 2.1: Schematization of the superfluid and Mott-insulator phases of the Bose-Hubbard model.

2.2.1 Mott-insulator phase

When the interaction term predominates over the hopping term ($U >> J$), the system is said to be in a Mott-insulator phase. In this regime the particles do not tunnel between neighboring sites, and instead remain *frozen* in the lattice. The ground state of the system will consist of atomic wavefunctions highly localized in space with a fixed number of atoms per site, thus the many-body ground state is a tensor product of local Fock states at each physical site,

$$|\psi_{MI}\rangle \propto \bigotimes_{i}^{L} (\hat{b}_i^\dagger)^n \, |\varnothing\rangle \,, \tag{2.9}$$

where n is the number of particles per site and $|\varnothing\rangle$ is the bosonic vacuum state.

2.2.2 Superfluid phase

If the hopping term predominates over the interaction term ($J >> U$) the system is said to be in a superfluid phase. In this regime particles tunnel freely between lattice sites, causing the ground state wave functions of the system to become highly delocalized in position space, thus the collective ground state is a superposition of all possible occupation states,

$$|\psi_{SF}\rangle \propto \left(\sum_{i}^{L} \hat{b}_i^\dagger \right)^N |\varnothing\rangle \,, \tag{2.10}$$

where N is the number of particles in the lattice.

2.3 Spin-1 Bose-Hubbard Model

We now move on including the spin-1 degree of freedom, this is performed by modifying the interaction potential in order to describe the spin interactions. This motivates the introduction of the theory of addition of angular momenta considering the coupled and uncoupled basis of the spin-1 system. Coupled basis $|s_1, s_2, F, M\rangle$ where s_i is the spin of the i_{th} particle, F is the total spin and M the total magnetic projection on the z-axis of the particles. Uncoupled basis $|s_1, s_2, \sigma_1, \sigma_2\rangle$ where now the individual magnetic projections on the z-axis (σ_i) are considered. In the spin-1 system that we aim to describe σ_i takes values $\{-1, 0, 1\}$ and we have the basis elements related via the Glebsch-Gordan coefficients.

2.3.1 Spin-1 Interacting Potential

Collisions involving spin interactions can only occur in symmetric channels, due to this we discard the total spin value $F = 1$, due to its anti-symmetric nature. We can include the spin term in the interaction expressing it as the sum over all processes associated with the values of total spin F. Using the coupled basis we have:

$$\hat{V}_{\text{int}} = \sum_F g_F \hat{P}_F \delta(x - x'), \quad \text{with} \quad g_F = \frac{4\pi\hbar^2 a_F}{m}, \tag{2.11}$$

where a_F is the scattering length associated with the process involving a total spin F, and $\hat{P}_F = |F, M\rangle\langle M, F|$ is the projector associated to the total spin F taking values $\{0, 2\}$. It is possible to directly express the interaction term in second quantization, in this case we first write the projectors in terms of spin operators for convenience, as detailed in Appendix A, yielding in Eq. (2.12).

$$\hat{V}_{\text{int}} = \left(\underbrace{c_0}_{\textbf{(1)}} + \underbrace{c_2 \hat{\boldsymbol{S}}_1 \cdot \hat{\boldsymbol{S}}_2}_{\textbf{(2)}} \right) \delta(x - x') \quad \text{with} \quad c_0 = \frac{g_0 + 2g_2}{3} \quad \text{and} \quad c_2 = \frac{g_2 - g_0}{3}. \tag{2.12}$$

Scattering processes are classified as those independent of the spin nature, **(1)**, responsible for *charge scattering*, and others dependent of the spin **(2)**, responsible for *spin scattering*. It is possible

to express the spin-one interaction potential in second quantization form as

$$\hat{V}_{\text{int}} = \frac{1}{2}\sum_{\{\sigma\}}\int dx\; dx' \hat{\Psi}^{\dagger}_{\sigma_1}(x)\hat{\Psi}^{\dagger}_{\sigma_2}(x')\langle\sigma_1,\sigma_2|\hat{V}_{\text{int}}|\sigma_3,\sigma_4\rangle\hat{\Psi}_{\sigma_3}(x')\hat{\Psi}_{\sigma_4}(x), \tag{2.13}$$

so the interaction term reads

$$\hat{H}_I = \frac{U_0}{2}\sum_{i,\sigma}\hat{n}_{i,\sigma}(\hat{n}_{i,\sigma}-1) + \frac{U_2}{2}\sum_i\left(\hat{\boldsymbol{F}}_i^2 - 2\sum_\sigma \hat{n}_{i,\sigma}\right), \tag{2.14}$$

where $\hat{\boldsymbol{F}}_i = \left(\hat{F}_i^x, \hat{F}_i^y, \hat{F}_i^z\right)$ is the total spin operator at site i, with $\hat{F}_i^\nu = \sum_{\sigma,\sigma'}\hat{b}^\dagger_{i,\sigma}[\hat{S}^\nu]_{\sigma,\sigma'}\hat{b}_{i,\sigma'}$, being $[\hat{S}^\nu]_{\sigma,\sigma'}$ the matrix elements of the spin-one matrices. Respectively, $\hat{b}^\dagger_{i,\sigma}$ and $\hat{b}_{i,\sigma}$ are the bosonic creation and annihilation operators, which create and annihilate a particle with a given magnetic projection σ at site i. The interaction strength in the channel F is denoted as U_F and is defined as

$$U_F = c_F\int dx\; |W(x)|^4. \tag{2.15}$$

The interaction strength usually characterizes the spin behavior of the system in the case of the alkali atoms commonly used in for this ultra-cold trapping [51], with $U_2 > 0$, the systems usually display antiferromagnetic behaviors (E.g.^{23}Na). And with $U_2 < 0$ (E.g.^{87}Rb), the systems exhibit ferromagnetic properties [52]. After the inclusion of the spin degree of freedom to the model, we are able to distinguish two types of spin-1 interactions, namely spin preserving and spin changing collisions. Fig. (2.2) schematizes the three principal terms of the spin-1 Bose-Hubbard model in Eq. (2.6).

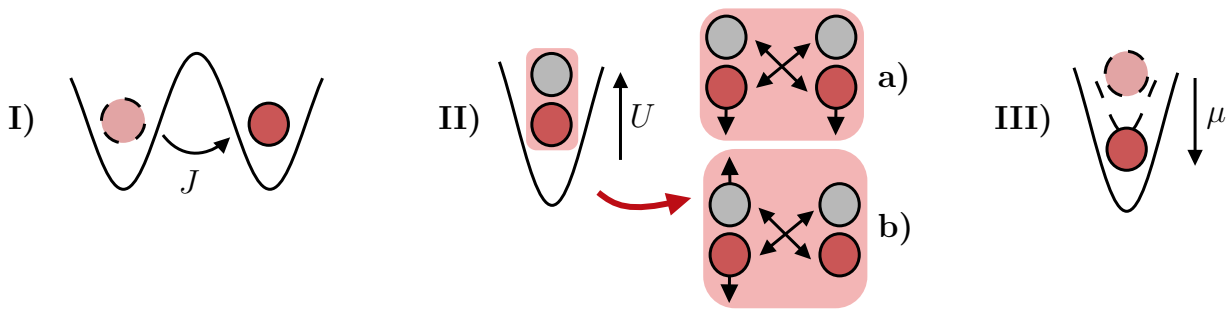

Figure 2.2: **I)** Hopping process. **II)** Interaction processes: **a)** spin preserving collisions and **b)** spin changing collisions. **III)** Chemical potential.

2.4 Synthetic Spin-Orbit Coupling

As a particle moves inside a potential related typically to an electric field $\vec{E}$, it experiences an effective magnetic field $\vec{B} \backsim \vec{k} \times \vec{E}$ in its frame of reference according to classical electrodynamics [33], as shown in Fig. (2.3). The appearing magnetic field interacts with its spin internal degree of freedom, leading to a Zeeman-type interaction that produces a splitting of the energy levels. In this sense, we can consider the *SOC* couples the spin internal degree of freedom of the particle with the external linear momentum that the particle possess as it moves. We consider a synthetic

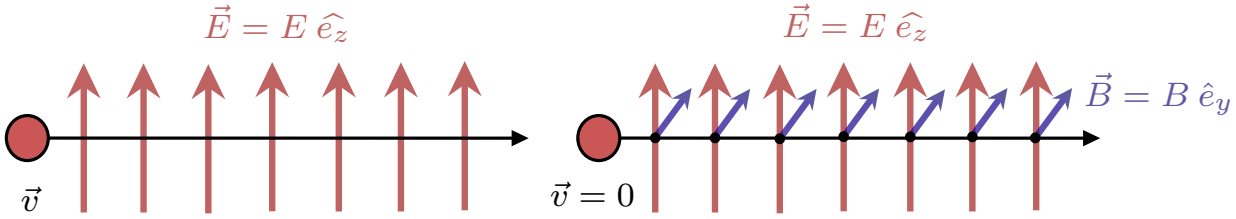

Figure 2.3: Spin-orbit coupling effect of a particle moving through an electric field in the inertial frame of reference **(left)** and in the particle's frame of reference **(right)**.

spin orbit coupling modeled by an effective magnetic field, this can be done by introducing the first quantized Hamiltonian

$$\hat{H}_{SO} \backsim \vec{\sigma} \cdot (\vec{k} \times \vec{E}) = \vec{E} \cdot (\vec{\sigma} \times \vec{k}). \tag{2.16}$$

By choosing $\vec{E} = E\vec{e_z}$ and the particles moving in the $\vec{e_y}$ direction, the Hamiltonian reduces to

$$\hat{H}_{SO} = \alpha(\hat{k}\,\hat{\sigma_k}), \tag{2.17}$$

where α gathers the information of the magnetic field strength along with other constants and their respective units.

Our next step is to elucidate the effects the spin-orbit coupling *(SOC)* has on the system, this can be easily visualized in the dispersion relation while the interactions are neglected. The first step to tackle this problem is to perform a transformation to $\hat{S}_y$ basis due to the orientation of the introduced magnetic field that we are interested in studying (as seen in Fig. (2.4)), followed by a Fourier transform of the Hamiltonian to the momentum space.

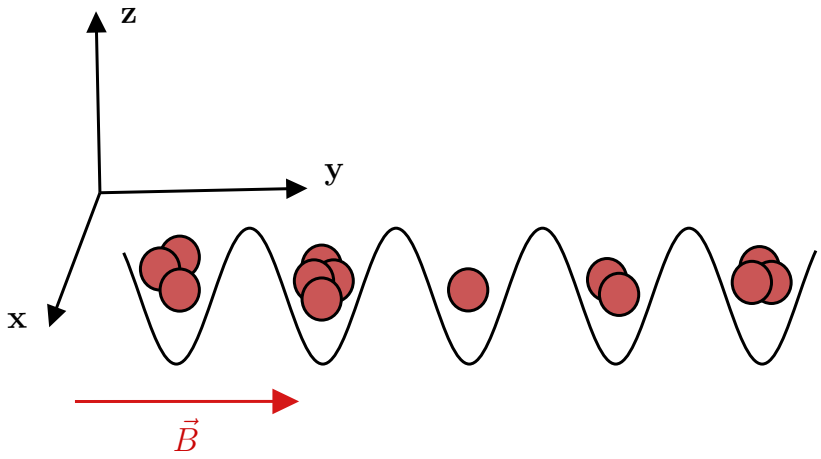

Figure 2.4: Physical system in presence of a magnetic field oriented in y-direction.

2.4.1 Generalized Hopping Term

We are considering that just the lowest energy bands are occupied, and under this approximation let us consider first the hopping term together with the effect of the *SOC* within the tight-binding approximation, which results in the Hamiltonian

$$\hat{H}_0 = -J \sum_{i,\sigma} \left(\hat{b}^{\dagger}_{i,\sigma} \mathbb{R}^{\sigma,\sigma'}_{i,i+1} \hat{b}_{i+1,\sigma} + \text{h.c.} \right), \tag{2.18}$$

where J is the site-independent hopping strength parameter, and matrix $\mathbb{R}^{\sigma,\sigma'}_{i,i+1}$ describes the hopping along with a flipping of a boson with spin σ' from site $i+1$ to the spin state σ on the neighbor site i and vice-versa, these processes are depicted in Fig. (2.5). This hopping matrix basically introduced a spin-dependent hopping parameter, in the case where a single quasi-momentum component is non-trivially coupled to the spin, it can be expressed as

$$\mathbb{R}_{l,l+1} = \cos(\alpha) + i \sin(\alpha) \hat{S}_y = \begin{bmatrix} \cos(\alpha) & \sin(\alpha) & 0 \\ -\sin(\alpha) & \cos(\alpha) & \sin(\alpha) \\ 0 & -\sin(\alpha) & \cos(\alpha) \end{bmatrix}, \tag{2.19}$$

where $\hat{S}_y$ is the usual spin-1 operator and parameter α quantifies the strength of the synthetic *SOC*, satisfying $-\frac{\pi}{2} < \alpha < \frac{\pi}{2}$.

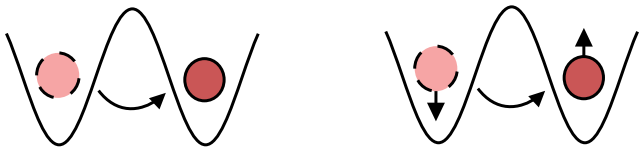

Figure 2.5: Conventional hopping term **(left side)** and hopping-flipping term **(right side)**.

Change from $\hat{S}_z$ to $\hat{S}_y$ basis.

Performing a change to the $\hat{S}_y$ basis on Eq. (2.18) results in a diagonalized free Hamiltonian of the form

$$\hat{H}_0 = -J \sum_{i,\bar{\sigma}} \left(\hat{b}^{\dagger}_{i,\bar{\sigma}} \mathbb{D}^{\bar{\sigma}}_{i,i+1} \hat{b}_{i+1,\bar{\sigma}} + \text{h.c.} \right), \tag{2.20}$$

where $\bar{\sigma}$ specifies the sum over the *helical projections* as the $\hat{S}_y$ internal projections, which account for the introduction of a new set of bosonic operators represented in terms of the magnetic operators as

$$\hat{b}_{l,\circlearrowleft} = \frac{-\hat{b}_{l,1} + i\sqrt{2}\hat{b}_{l,0} + \hat{b}_{l,-1}}{2}, \quad \hat{b}_{l,|} = \frac{\hat{b}_{l,1} + \hat{b}_{l,-1}}{\sqrt{2}}, \quad \text{and} \quad \hat{b}_{l,\circlearrowright} = \frac{-\hat{b}_{l,1} - i\sqrt{2}\hat{b}_{l,0} + \hat{b}_{l,-1}}{2},$$

with the corresponding helical projections ($\bar{\sigma}$) taking value 1 for the left state ($\circlearrowleft$), 0 for the linear state ($|$) and -1 for the right state ($\circlearrowright$). The new helical hopping matrix is expressed as

$$\mathbb{D}^{\bar{\sigma}}_{l,l+1} = \begin{bmatrix} \cos(\alpha) - i\sqrt{2}\sin(\alpha) & 0 & 0 \\ 0 & \cos(\alpha) & 0 \\ 0 & 0 & \cos(\alpha) + i\sqrt{2}\sin(\alpha) \end{bmatrix}. \tag{2.21}$$

Transformation to quasi-momentum space.

Hopping Hamiltonian in Eq. (2.18) can be transformed into k-space due to translational symmetry by employing

$$\hat{b}^{\dagger}_{l,\bar{\sigma}} = \frac{1}{\sqrt{L}} \sum_{k} e^{ikl} \hat{b}^{\dagger}_{k,\bar{\sigma}}, \tag{2.22}$$

resulting in

$$\hat{H}_0 = -2J \sum_{k,\bar{\sigma}} \hat{b}^{\dagger}_{k,\bar{\sigma}} \mathbb{D}^{\bar{\sigma}}_{k} \hat{b}_{k,\bar{\sigma}}, \tag{2.23}$$

where

$$\mathbb{D}_k^{\bar{\sigma}} = \cos(\alpha) \begin{bmatrix} \cos(k) - \sqrt{2}\tan(\alpha)\sin(k) & 0 & 0 \\ 0 & \cos(k) & 0 \\ 0 & 0 & \cos(k) + \sqrt{2}\tan(\alpha)\sin(k) \end{bmatrix}. \tag{2.24}$$

For explicit calculation the reader is addressed to Appendix B. Due to its diagonal form, we can express Eq. (2.23) in terms of the helical projections as:

$$\hat{H}_0 = \sum_{k,\bar{\sigma}} \underbrace{-2J\left(\cos(\alpha)\cos(k) - \bar{\sigma}\sqrt{2}\sin(\alpha)\sin(k)\right)}_{\epsilon_{\bar{\sigma}}(k)} \hat{b}^{\dagger}_{k,\bar{\sigma}}\hat{b}_{k,\bar{\sigma}}. \tag{2.25}$$

The effect of the *SOC* on the system is visualized in the dispersion relation $\epsilon_{\bar{\sigma}}(k)$ for every helical projection, this is illustrated in Fig. (2.6).

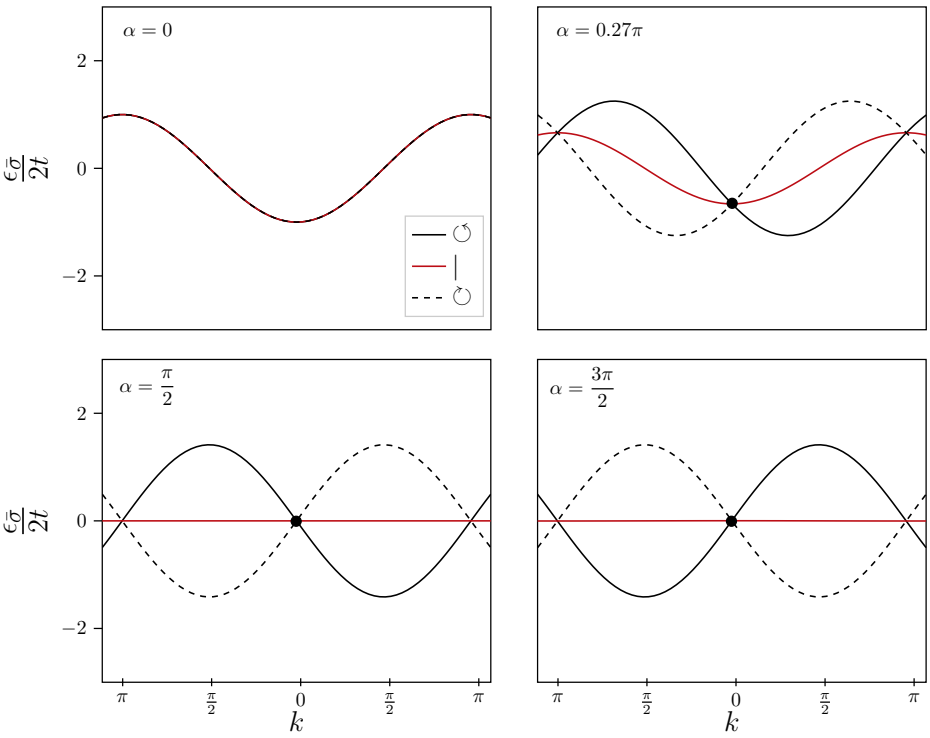

Figure 2.6: Dispersion relation for the hopping term with different α values.

There is a particular interest in the crossing points in Fig. (2.6), the middle one is known as Rashba-crossing point. In these crossing points the energy gap between the different spin states

disappears and lead to interesting phenomena such as spin currents [53], which are out of the scope of this work. The chemical potential term is given by $\hat{H}_\mu = -\mu \sum_{i,\sigma} \hat{n}_{i,\sigma} = -\mu \sum_{i,\sigma} \hat{b}^\dagger_{i,\sigma} \hat{b}_{i,\sigma}$. Performing the basis transformation defined by matrix $\mathbb{U}$ in Eq. (B.2), results in

$$\hat{H}_\mu = -\mu \sum_{i,\sigma} \hat{b}^\dagger_{i,\sigma} (\mathbb{U}^\dagger \mathbb{U}) \hat{b}_{i,\sigma} = -\mu \sum_{i,\bar{\sigma}} \hat{b}^\dagger_{i,\bar{\sigma}} \hat{b}_{i,\bar{\sigma}}. \tag{2.26}$$

Now applying the Fourier transform (Eq. (2.22)) one gets,

$$\hat{H}_\mu = -\mu \sum_{k,\bar{\sigma}} \hat{b}^\dagger_{k,\bar{\sigma}} \hat{b}_{k,\bar{\sigma}}, \tag{2.27}$$

where the helical-independent chemical potential parameter is added to the hopping dispersion relation, leading just to a vertical energy shift that does not alter the relevant physics of the system.

2.4.2 Interaction term

The interaction term is given by:

$$\hat{H}_I = \underbrace{\frac{U_0}{2} \sum_{i,\sigma} \hat{n}_{i,\sigma}(\hat{n}_{i,\sigma} - 1)}_{\textbf{(1)}} + \underbrace{\frac{U_2}{2} \sum_i \left(\hat{\boldsymbol{F}}_i^2 - 2 \sum_\sigma \hat{n}_{i,\sigma} \right)}_{\textbf{(2)}}, \tag{2.28}$$

starting with **(1)**:

$$\textbf{(1)} = \frac{U_0}{2} \sum_{i,\sigma} \hat{n}_{i,\sigma} \hat{n}_{i,\sigma} - \frac{U_0}{2} \sum_{i,\sigma} \hat{n}_{i,\sigma}, \tag{2.29}$$

where the last term transforms into the $\hat{S}_y$ basis, akin to the chemical potential term in Eq. (2.26). A similar argument applies to the Fourier transform, resulting in a vertical energy shift in the dispersion relation by a factor of $\frac{U_0}{2}$. Let's focus on the first term, this is:

$$\frac{U_0}{2} \sum_{i,\sigma} \hat{n}_{i,\sigma} \hat{n}_{i,\sigma} \xrightarrow{\hat{S}^y \text{ basis}} \frac{U_0}{2} \sum_{i,\sigma} \hat{b}^\dagger_{i,\sigma} (\mathbb{U}^\dagger \mathbb{U}) \hat{b}_{i,\sigma} \hat{b}^\dagger_{i,\sigma} (\mathbb{U}^\dagger \mathbb{U}) \hat{b}_{i,\sigma} = \frac{U_0}{2} \sum_{i,\bar{\sigma}} \hat{n}_{i,\bar{\sigma}} \hat{n}_{i,\bar{\sigma}}. \tag{2.30}$$

Now applying the Fourier transform given by Eq. (2.22):

$$\begin{aligned}\frac{U_0}{2}\sum_{i,\bar{\sigma}}\hat{n}_{i,\bar{\sigma}}\hat{n}_{i,\bar{\sigma}} &= \frac{U_0}{2}\sum_{l,\bar{\sigma}}\hat{b}^{\dagger}_{l,\bar{\sigma}}\hat{b}_{l,\bar{\sigma}}\hat{b}^{\dagger}_{l,\bar{\sigma}}\hat{b}_{l,\bar{\sigma}} \\ &= \frac{U_0}{2}\sum_{k_1,\,k_2,\,k_3,\,k_4,\bar{\sigma}}\frac{1}{L}\left(\sum_{l}\frac{1}{L}e^{i[(k_1+k_3)-(k_2+k_4)]l}\right)\hat{b}^{\dagger}_{k_1,\bar{\sigma}}\hat{b}_{k_2,\bar{\sigma}}\hat{b}^{\dagger}_{k_3,\bar{\sigma}}\hat{b}_{k_4,\bar{\sigma}} \\ &= \frac{U_0}{2L}\sum_{k_1,\,k_2,\,k_3,\,k_4,\bar{\sigma}}\delta_{k_1+k_3,\,k_2+k_4}\quad\hat{b}^{\dagger}_{k_1,\bar{\sigma}}\hat{b}_{k_2,\bar{\sigma}}\hat{b}^{\dagger}_{k_3,\bar{\sigma}}\hat{b}_{k_4,\bar{\sigma}}.\end{aligned}$$

The quasi-momenta satisfies the condition $k_1 + k_3 = k_2 + k_4$, hence renaming $k_2 = k$ and $k_4 = k'$, we may introduce the transferred momentum q by choosing $k_1 = k + q$ and $k_3 = k' - q$, therefore the term is rewritten as

$$\implies \frac{U_0}{2L}\sum_{k,\,k',\bar{\sigma}}\hat{b}^{\dagger}_{k+q,\bar{\sigma}}\hat{b}_{k,\bar{\sigma}}\hat{b}^{\dagger}_{k'-q,\bar{\sigma}}\hat{b}_{k',\bar{\sigma}} = \frac{U_0}{2L}\sum_{k,\,k',\bar{\sigma}}\hat{b}^{\dagger}_{k+q,\bar{\sigma}}\hat{b}^{\dagger}_{k'-q,\bar{\sigma}}\hat{b}_{k,\bar{\sigma}}\hat{b}_{k',\bar{\sigma}}. \tag{2.31}$$

This is equivalent to a scattering process between two particles with initial momenta k and k', after the interaction one results with momenta $k + q$ and the other $k' - q$, conserving the total momentum in the elastic collision, as represented in Fig. (2.7).

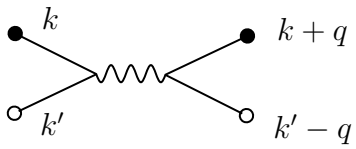

Figure 2.7: Elastic collision between two particles with transferred momentum q .

Now focusing on **(2)** from Eq. (2.28):

$$\mathbf{(2)} = \frac{U_2}{2}\sum_{i}\hat{\boldsymbol{F}}_i^2 - U_2\sum_{i,\,\sigma}\hat{n}_{i,\sigma}. \tag{2.32}$$

Last term transforms exactly as the previous expression calculated in the chemical potential case, both to the $\hat{S}_y$ basis and to the momentum space, adding just a vertical energy shift given by the parameter U_2. First term remains unchanged when transforming to the $\hat{S}_y$ basis, this transformation

yields in a permutation of the previous spin operators given in $\hat{S}_z$ basis as follows:

$$\hat{S}_z \to \hat{S}_y, \quad \hat{S}_x \to \hat{S}_y, \quad \text{and} \quad \hat{S}_y \to \hat{S}_z, \tag{2.33}$$

thus leaving the total spin operator $\hat{\boldsymbol{F}}_i^2$ invariant under the transformation.

Collecting all of the results we can write the spin-1 Bose-Hubbard model in the $\hat{S}_y$ basis in term of the helical states, as follows:

$$\hat{H} = -J \sum_{i,\bar{\sigma}} \left(\hat{b}_{i,\bar{\sigma}}^{\dagger} \mathbb{D}_{i,i+1}^{\bar{\sigma}} \hat{b}_{i+1,\bar{\sigma}} + \text{h.c.} \right) + \frac{U_0}{2} \sum_{i,\bar{\sigma}} \hat{n}_{i,\bar{\sigma}} (\hat{n}_{i,\bar{\sigma}} - 1) + \frac{U_2}{2} \sum_i \hat{\boldsymbol{F}}_i^2 - \left(\mu + \frac{U_2}{2} \right) \sum_{i,\bar{\sigma}} \hat{n}_{i,\bar{\sigma}} \tag{2.34}$$

Last Hamiltonian can be expressed in an alternative form (Eq. (2.35)) by taking the explicit representation of the projection operators in the coupled basis when expressing it in second-quantization formalism. This form, despite not being compact, is more convenient for the purpose of this work since it displays directly the spin changing and preserving local interaction terms, facilitating the representation in the Matrix Product Operators (MPO) formalism introduced in Chapter 3 and, therefore the implementation in the numerical method. Details on the derivation of the Hamiltonian are presented in Appendix A.

$$\begin{aligned} \hat{H} = & -J \sum_{i,\bar{\sigma}} \left(\hat{b}_{i,\bar{\sigma}}^{\dagger} \mathbb{D}_{i,i+1}^{\bar{\sigma}} \hat{b}_{i+1,\bar{\sigma}} + \text{h.c.} \right) + \sum_i \Bigg[\left(\frac{g_0 + 2g_2}{6} \right) \hat{b}_{|}^{\dagger} \hat{b}_{|}^{\dagger} \hat{b}_{|} \hat{b}_{|} + \left(\frac{2g_0 + g_2}{3} \right) \hat{b}_{\circlearrowleft}^{\dagger} \hat{b}_{\circlearrowleft}^{\dagger} \hat{b}_{\circlearrowleft} \hat{b}_{\circlearrowleft} \\ & + \left(\frac{g_2 - g_0}{3} \right) \left(\hat{b}_{\circlearrowleft}^{\dagger} \hat{b}_{\circlearrowleft}^{\dagger} \hat{b}_{|} \hat{b}_{|} + \hat{b}_{|}^{\dagger} \hat{b}_{|}^{\dagger} \hat{b}_{\circlearrowleft} \hat{b}_{\circlearrowleft} \right) \\ & + \frac{g_2}{2} \left(\hat{b}_{\circlearrowleft}^{\dagger} \hat{b}_{\circlearrowleft}^{\dagger} \hat{b}_{\circlearrowleft} \hat{b}_{\circlearrowleft} + 2\hat{b}_{\circlearrowleft}^{\dagger} \hat{b}_{|}^{\dagger} \hat{b}_{\circlearrowleft} \hat{b}_{|} + 2\hat{b}_{\circlearrowleft}^{\dagger} \hat{b}_{|}^{\dagger} \hat{b}_{\circlearrowleft} \hat{b}_{|} + \hat{b}_{\circlearrowleft}^{\dagger} \hat{b}_{\circlearrowleft}^{\dagger} \hat{b}_{\circlearrowleft} \hat{b}_{\circlearrowleft} \right) \Bigg]_i , \end{aligned} \tag{2.35}$$

Chapter 3 is entirely devoted to the introduction of the theoretical formalism of Matrix Product States *(MPS)* and Operators *(MPO)*. Additionally, Chapter 4 centers on the numerical techniques and algorithmic implementations of the formalism previously introduced to address this problem. Chapter 5 is devoted to the measurements and results performed over two test models, together with the discussions. Finally, the conclusions and perspectives are presented in Chapter 6.

Chapter 3

Matrix Product States And Operators

Tensor networks formalism offers a powerful and versatile framework for simulating quantum systems ranging from trivial Hamiltonians to complex models exhibiting topological order [54]. This formalism can be considered as a symbiosis of theoretical and numerical methods, which are combined for simulating various systems in one or more dimensions. In one dimension, Matrix Product States (*MPS*) have emerged as the most widely used approach systems that might exhibit translational invariance, addressing the challenge of exponential Hilbert space growth by providing efficient representations of quantum states, and are particularly well-suited for approximating ground states and simulating dynamics in one-dimensional systems using methods such as Time Evolution Block Decimation (*TEBD*) [55] and variational methods [56].

The Matrix Product Operators (*MPO*) formalism originates as a natural extension of the Matrix Product State (*MPS*) representation, it was introduced in the early 2000s, particularly through the work of Verstraete, Cirac, and collaborators [57], who generalized tensor network techniques to efficiently represent not only quantum states but also many-body operators. The key idea behind *MPOs* is to express global operators such as Hamiltonians or observables as products of local tensors with bounded bond dimensions. This structure allows for efficient storage and manipulation of operators that would otherwise require exponentially large memory in a naive representation. The *MPO* framework retains essential physical features like locality and symmetry and, in combination with *MPS*, enables efficient numerical simulations of strongly correlated one-dimensional systems with high accuracy and scalability.

In this chapter, we introduce the Matrix Product States *(MPS)* and Operators *(MPO)* formalisms as advantageous tools within the family of tensor networks for the simulation of many-body quantum-systems, allowing to perform truncations and exploit the properties of translational symmetry present in many systems, therefore reducing the overall computational cost for the simulations. First, we start by reviewing the concept of entanglement and how it is measured, then introducing the *MPS* form of a quantum state, then reviewing the basics on tensor networks and Penrose's graphical representation, finally highlighting some relevant considerations when choosing the right representation for the state. Next we move on to the Matrix Product Operator *(MPO)*

representation, specifying the procedure for measuring expectation values.

Information of a quantum system is stored in the state $|\Psi\rangle \in \mathcal{H}$, which can be expressed as a superposition of a given basis elements of the corresponding Hilbert space, this is:

$$|\Psi\rangle = \sum_{i}^{N} a_i \, |\psi_i\rangle \, , \tag{3.1}$$

where N is the amount of basis elements, and $a_i = \langle\psi_i|\, \Psi\rangle$ is the probability amplitude coefficient that quantifies the probability of finding state $|\Psi\rangle$ in the basis element $|\psi_i\rangle$.

Considering a generic bipartite system where it can be separated in two subsystems A and B, Eq. (3.1) yields on:

$$|\Psi\rangle = \sum_{i}^{N_A} \sum_{j}^{N_B} a_{ij} \, |A_i\rangle \otimes |B_j\rangle \quad \text{with} \quad N = N_A + N_B, \tag{3.2}$$

where $\{|A_i\rangle\} \in \mathcal{H}_A$ and $\{|B_j\rangle\} \in \mathcal{H}_B$ form a complete set of orthonormal basis elements and $\mathcal{H} = \mathcal{H}_A \otimes \mathcal{H}_B$ is the total Hilbert space of the system. If the state can be expressed as $|\Psi\rangle = |\psi\rangle_A \otimes |\psi\rangle_B$, we say our system is **separable**, if not we say it is **entangled**.

Entanglement is one of the most relevant features exhibited in quantum mechanics, intuitively gives an insight on how the system information is mixed or separated within its components. It can be quantified using the Von Neumann entanglement entropy, given by

$$S_{\text{VN}} = -\sum_{n} p_n \ln(p_n), \tag{3.3}$$

where p_n are the eigenvalues of the density matrix $\hat{\rho} = |\Psi\rangle \langle\Psi|$.

One of the main problems encountered when studying many-body quantum-systems is the exponential growth of the Hilbert space with the size of the system, this is reflected in the computational cost required for simulating larger systems, thus motivating the scientific community to look for alternatives that allow to perform truncations on the Hilbert space dimension while still approximating the physical behavior of the system. As a solution to this problem emerges the family of tensor network methods, with different approaches to simulate different kind of systems, for example Projected Entangled Pair States (*PEPS*) [47] for 2-D systems and the so called Matrix Product States *(MPS)* [47] for 1-D systems, which is one of the two main topics on this chapter.

It was proved by M. Hastings in 2007 [58] that for one-dimensional local gapped Hamiltonians, the entanglement entropy of a bipartition given by Eq. (3.3) is independent of the system size (L) as it reaches the thermodynamical limit ($L \to \infty$). This is known as the **area law**, and justifies the advantages of studying these type of systems using the one-dimensional *MPS* method. It is important to note, however, that this behavior holds only for systems out of criticality.

3.1 Tensor networks and Penrose graphical notation

A tensor is defined as a mathematical object that follows a certain transformation rule, it can be described as a multidimensional array of complex numbers. The rank of a tensor is defined as the number of indices. Hence, a number is a rank-0 tensor, a vector is a rank-1 tensor and a matrix is a rank-2 tensor. An useful tool for visualizing tensors is Penrose's graphical representation [42], shown in Fig. (3.1). A tensor contraction is a sum over one or more equal indices of different tensors,

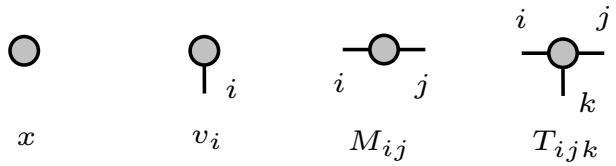

Figure 3.1: Penrose graphical representation for tensors of different rank. From left to right, scalar, vector, matrix and rank three tensor.

the non contracted indices are called open indices. In graphical representation, the contracted tensors are connected with the legs corresponding to the contracted indices, and the open indices are represented by the non-connected legs, as presented in Fig. (3.2). In this research we focus

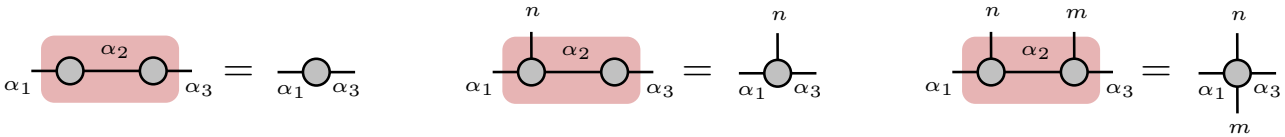

$$C_{\alpha_1,\alpha_3} = \sum_{\alpha_2} A_{\alpha_1,\alpha_2} B_{\alpha_2,\alpha_3} \qquad C^{n}_{\alpha_1,\alpha_3} = \sum_{\alpha_2} A^{n}_{\alpha_1,\alpha_2} B_{\alpha_2,\alpha_3} \qquad C^{n,m}_{\alpha_1,\alpha_3} = \sum_{\alpha_2} A^{n}_{\alpha_1,\alpha_2} B^{m}_{\alpha_2,\alpha_3}$$

Figure 3.2: Multiple contraction examples of different rank tensors.

on tensors where the indices have no geometrical relevance, thus we do not require to distinguish between covariant and contra-variant forms, nevertheless this distinction is relevant in other tensor network methods.

Tensor networks refers to a network structure formed by multiple tensors connected following certain contraction rules, it provides an useful formalism for modeling systems arranged in certain geometries, allowing to deal with large amounts of data while reducing computational cost of the simulations with operations like truncations, contractions and reshaping over the tensors. Tensor networks have emerged in the physics community as a novel tool employed in multiple fields like quantum machine learning [59], gravitation [60] and condensed matter physics [61], being the last one the case of the present work. There are multiple types of tensor networks with different properties that vary depending on the dimension and geometry of the physical system, some of the most important tensor networks used in 1-D and 2-D condensed matter physics are shown in Fig. (3.3), the reader is invited to review further literature on those examples [62].

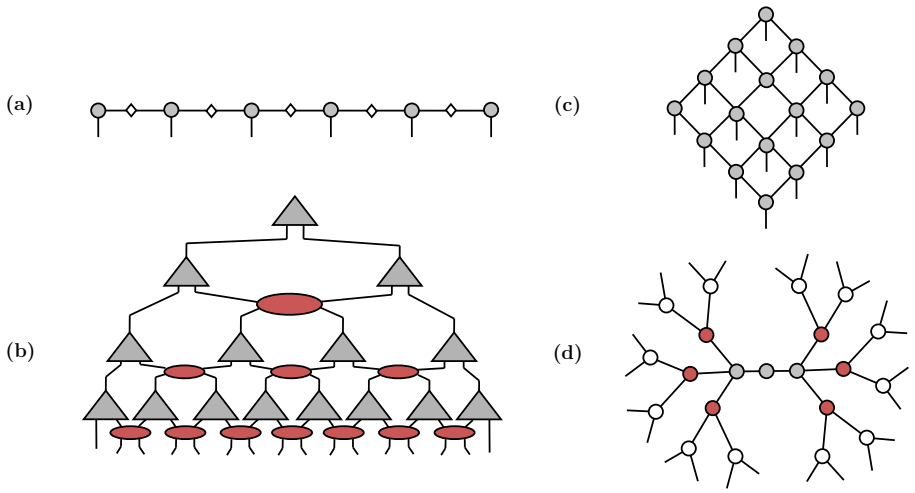

Figure 3.3: Some widely used tensor network representations . **(a)** Matrix product state *(MPS)* [47]. **(b)** Projected entangled pair state *(PEPS)* [47]. **(c)** Hierarchical tucker [63]. **(d)** Tree tensor Network *(TTN)* [64].

3.2 Matrix product states (MPS)

Among the variety of quantum systems that can be modeled using different tensor network methods, we focus on one-dimensional systems such as atoms trapped in an optical lattice and other physical lattice systems that can be seen as an array of L physical sites, we iteratively perform a set of decompositions and transformations over the state in order to reach the desired *MPS* representation.

3.2.1 Construction of the MPS

In order to construct the *MPS* representation, we use the singular value decomposition *(SVD)* [65] (also called Schmidt decomposition) , this is a linear algebra technique for factorizing real or complex matrices. Suppose we have a $m \times n$ matrix M, the *SVD* is given by:

$$M_{m\times n} = U_{m\times m} D_{m\times n} V^*_{n\times n}, \tag{3.4}$$

where U is a left-unitary matrix ($U^\dagger U = 1$), V is a right-unitary matrix ($VV^\dagger = 1$) and D is a diagonal matrix $M_{\alpha,\alpha'} = \lambda_\alpha \delta_{\alpha,\alpha'}$, where λ_α correspond to the singular values of matrix M, which in this context are commonly referred as the Schmidt coefficients.

Let us start by separating the L lattice sites into a bipartite system formed by the first $L-1$ sites and the last L site, as in Fig. (3.4). We perform a Schmidt decomposition to the probability

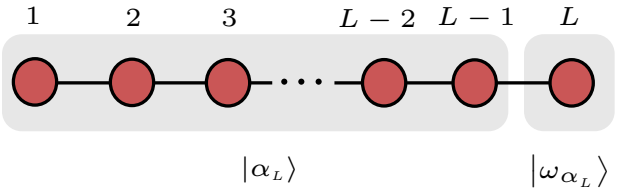

$$|\Psi\rangle = \sum_{\alpha_L}^{N_A} \sum_{\omega_{\alpha_L}}^{N_B} a_{\alpha_L,\omega_{\alpha_L}} |\alpha_L\rangle \otimes |\omega_{\alpha_L}\rangle \tag{3.5}$$

Figure 3.4: Expression of the state $|\Psi\rangle$ as a bipartite system formed by first $L-1$ left sites and last site L.

amplitude coefficients in Eq. (3.5), resulting in

$$|\Psi\rangle = \sum_{\alpha_L}^{N_B} \lambda_{\alpha_L} |\alpha_L\rangle^{[A]} \otimes |\omega_{\alpha_L}\rangle^{[B]}, \tag{3.6}$$

where we made the consideration $N_A > N_B$. Note that $\{|\alpha_L\rangle^{[A]}\}$ (left block) and $\{|\omega_{\alpha_L}\rangle^{[B]}\}$ are two new orthonormal basis sets with N_B elements, and the Schmidt coefficients are positive real numbers satisfying the normalization condition $\sum_{\alpha_L} \lambda_{\alpha_L} = 1$. We project the last-site basis element in a suitable basis for second quantization formalism as it is the Fock basis, $|\omega_{\alpha_L}\rangle^{[B]} = \sum_{n_L} \Gamma^{n_L}_{\alpha_L} |n_L\rangle$, where $\Gamma^{n_L}_{\alpha_L}$ are the transformation matrix elements and $\{|n_L\rangle\}$ are the elements of the Fock basis,

also known as occupation basis. Therefore, $|\Psi\rangle$ is given by:

$$|\Psi\rangle = \sum_{\alpha_L,\, n_L} \lambda_{\alpha_L} \Gamma^{n_L}_{\alpha_L} |\alpha_L\rangle^{[A]} \otimes |n_L\rangle \,. \tag{3.7}$$

We now focus on state $|\alpha_L\rangle^{[A]}$, we again separate this $L-1$ lattice sites system into a bipartite system and perform the Schmidt decomposition as shown in Fig. (3.5). Note that $\left|\omega^{\alpha_L}_{\alpha_{L-1}}\right\rangle^{[B]}$

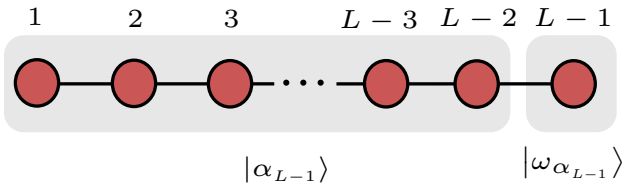

$$|\alpha_L\rangle = \sum_{\alpha_{L-1}} \lambda_{\alpha_{L-1}} |\alpha_{L-1}\rangle^{[A]} \otimes \left|\omega^{\alpha_L}_{\alpha_{L-1}}\right\rangle^{[B]}, \tag{3.8}$$

Figure 3.5: Expression of the state $|\alpha_L\rangle^{[A]}$ as a bipartite system formed by first $L-2$ sites and last site $L-1$.

depends also on index α_L, this is due to its connection (entanglement sharing) with the last site of the chain L. Projecting this state in the Fock basis and replacing in Eq. (3.8) we obtain

$$|\alpha_L\rangle = \sum_{\alpha_{L-1},\, n_L} \lambda_{\alpha_{L-1}} \Gamma^{n_{L-1}}_{\alpha_{L-1},\, \alpha_L} |\alpha_{L-1}\rangle^{[A]} \otimes |n_{L-1}\rangle \,, \tag{3.9}$$

replacing this in Eq. (3.7) results in

$$|\Psi\rangle = \sum_{\substack{\alpha_{L-1},\, \alpha_L \\ n_{L-1},\, n_L}} \lambda_{\alpha_{L-1}} \Gamma^{n_{L-1}}_{\alpha_{L-1},\, \alpha_L} \lambda_{\alpha_L} \Gamma^{n_L}_{\alpha_L} |\alpha_{L-1}\rangle^{[A]} \otimes |n_{L-1},\, n_L\rangle \,. \tag{3.10}$$

We perform the same procedure with $|\alpha_{L-1}\rangle^{[A]}$ and the following elements of the left block until we reach the last two sites as shown in Fig. (3.6), after performing the process iteratively we end up with the state written as follows:

$$|\Psi\rangle = \sum_{\substack{\alpha_2,\ldots,\alpha_L \\ n_1,\ldots,n_L}} \Gamma^{n_1}_{\alpha_2} \lambda_{\alpha_2} \Gamma^{n_2}_{\alpha_2,\, \alpha_3} \ldots \lambda_{\alpha_{L-1}} \Gamma^{n_{L-1}}_{\alpha_{L-1},\, \alpha_L} \lambda_{\alpha_L} \Gamma^{n_L}_{\alpha_L} |n_1, \ldots, n_L\rangle \,. \tag{3.11}$$

We group terms in order to simplify the representation, this is shown in Fig. (3.7). We have defined $A^{n_s}_{\alpha_s,\alpha_{s+1}} \equiv \lambda_{\alpha_s} \Gamma^{n_s}_{\alpha_s,\alpha_{s+1}}$ in order to simplify the expressions. The α_1 and α_{L+1} coefficients in red are

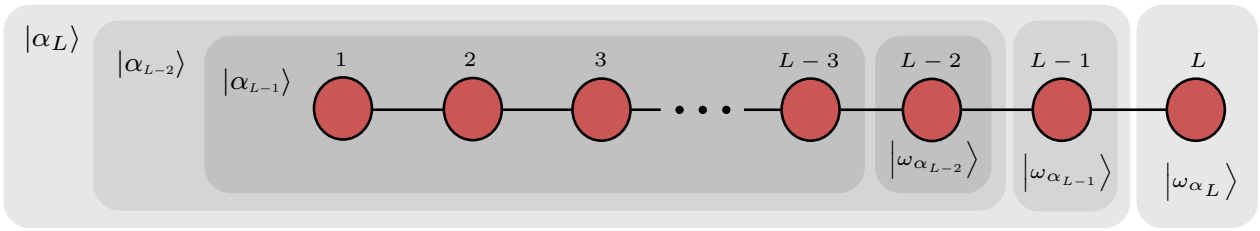

Figure 3.6: Splitting scheme for the lattice system.

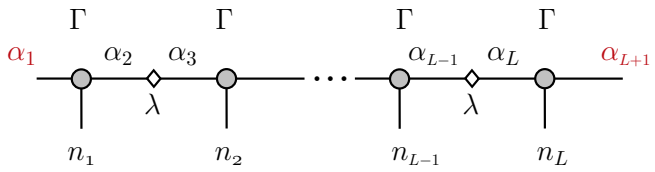

$$|\Psi\rangle = \sum_{\substack{\alpha_2,\ldots,\alpha_L \\ n_1,\ldots,n_L}} A^{n_1}_{\alpha_1,\,\alpha_2} \ldots A^{n_L}_{\alpha_L,\,\alpha_{L+1}} |n_1,\ldots,n_L\rangle\,.$$

Figure 3.7: Simplified expression and graphical Penrose diagram of the *MPS*.

introduced to keep all the matrices expressed as tensors of the same rank ($\alpha_1 = \alpha_{L+1} = 1$), we will discuss this thoroughly in Chapter 4 when specifying the numerical details. The expression shown in Fig. (3.7) is the Matrix Product Representation *(MPS)* of the state $|\Psi\rangle$. Later on we detail how this *MPS* constitutes an advantageous representation of the state, allowing to perform computational truncations without loosing relevant information about the system, we also encounter how this state, along with the Matrix Product Operators *(MPO)* enables us to perform relevant physical calculations, such as computing expectation values of local operators, finding the ground state of a system and measuring correlations in an infinite system or a system with periodic boundary conditions.

Truncations

One of the most important properties the *MPS* possess is that it's dimension can be truncated up to a certain point while retaining relevant physical features of the system, thus reducing considerably the dimensionality of the data needed to represent and simulate a given problem. It is demonstrated that the Schmidt coefficients λ_s decay exponentially with α_s [66]. Therefore, we can keep only the information associated with the first and larger coefficients without loosing too much relevant contributions to the overall description of a system, this is, we can choose a restriction $\alpha_s = 1, \ldots, \chi_s$, where it is possible to choose an equal parameter $\chi_s = \chi$ for every site. Under this considerations the number of matrix elements for every $A^{n_s}_{\alpha_s\,\alpha_{s+1}}$ would be given by $N_s = d\chi^2$, where d is the number of degrees of freedom of the system, this would still represent faithfully the original state

while reducing the amount of required parameters for representing the state. Parameter χ could be updated every iteration of the numerical method for guaranteeing the representation of the state remains close to the original one (adaptive truncation [67]), nevertheless, in the present work this further consideration is not going to be implemented.

3.2.2 Orthogonalization process

The *MPS* form shown in Fig. (3.7) may be subjected to a simplification with the aim of performing calculations as expectation values, hence the next step is to write the *MPS* in an orthogonal way such that we reduce the computational cost of these calculations. For this, we have done an entire procedure described explicitly on Section C.1 of Appendix C, where the resulting state is given by:

$$|\Psi\rangle = \sum_{n_k,\alpha_k,\alpha_{k+1}} A^{n_k}_{\alpha_k,\alpha_{k+1}} |\alpha_k\rangle |n_k\rangle \left|\omega_{\alpha_{k+1}}\right\rangle , \tag{3.12}$$

where

$$|\alpha_k\rangle = \sum_{\alpha_1 \ldots \alpha_{k-1}} \prod_{s=1}^{k-1} U^{n_s}_{\alpha_s,\alpha_{s+1}} |n_s\rangle , \quad \text{and} \quad \left|\omega_{\alpha_{k+1}}\right\rangle = \sum_{\alpha_{k+2} \ldots \alpha_{L+1}} \prod_{s=k+1}^{L} V^{n_s *}_{\alpha_s,\alpha_{s+1}} |n_s\rangle . \tag{3.13}$$

Due to the left and right unitary properties of matrices U and V, we have $\langle \alpha_k | \alpha'_k \rangle = \delta_{\alpha_k,\alpha'_k}$ and $\langle \omega_{\alpha_k} | \omega'_{\alpha_k} \rangle = \delta_{\alpha_k,\alpha'_k}$, therefore state $|\Psi\rangle$ is orthogonalized.

The *MPS* in Eq. (3.12) is said to be written in the canonical form, in particular a *mixed canonical form* where the k-th site matrix is often referred as the orthogonality center or active site, which gathers all the information describing the state. Different canonical forms of the *MPS* on graphical representation are presented on Fig. (3.8), where the only difference is the location of the active site and therefore the numerical process to perform measurements over the state.

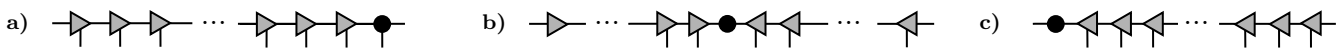

Figure 3.8: Canonical *MPS* representations. **(a)** Left canonical form. **(b)** Mixed canonical form. **(c)** Right canonical form.

Left (right) canonical forms are obtained performing the same procedure as depicted for the mixed canonical form but performing just the *SVD* over the matrices on left (right) side until the last (first) of the tensors .

On next section we see how the canonical form representation is advantageous for several essential calculations such as the norm of the state or expectation values of local operators.

3.2.3 Calculation of expectation values

Calculating expectation values is important, as it allows us to extract information about relevant physical quantities that describe the behavior of our system. We review how to calculate the expectation value of a general local operator using the canonical form of the *MPS* , introducing the concept of transfer matrix and then using this to express another relevant calculations like the norm of the state and correlation functions.

Local operators.

We are going to calculate the expectation value of a local operator $\hat{O}_k$ acting on k-th site. We proceed with the *MPS* given in the mixed canonical form where the orthogonality point is in k-th site, as in Eq. (3.12).

$$\begin{aligned}
\langle\Psi|\,\hat{O}_k\,|\Psi\rangle &= \left(\sum_{n'_k,\alpha'_k,\alpha'_{k+1}} A^{n'_k *}_{\alpha'_k,\alpha'_{k+1}}\,\langle\alpha'_k|\,\langle n'_k|\,\left\langle\omega'_{\alpha_{k+1}}\right|\right)\hat{O}_k\left(\sum_{n_k,\alpha_k,\alpha_{k+1}} A^{n_k}_{\alpha_k,\alpha_{k+1}}\,|\alpha_k\rangle\,|n_k\rangle\,\left|\omega_{\alpha_{k+1}}\right\rangle\right)\\
&= \sum_{\substack{n_k,\alpha_k,\alpha_{k+1}\\ n'_k,\alpha'_k,\alpha'_{k+1}}} A^{n'_k *}_{\alpha'_k,\alpha'_{k+1}}\,\langle n'_k|\,\hat{O}_k\,|n_k\rangle\,A^{n_k}_{\alpha_k,\alpha_{k+1}}\underbrace{\langle\alpha'_k|\,\alpha_k\rangle}_{\delta_{\alpha_k,\alpha'_k}}\underbrace{\left\langle\omega_{\alpha_{k+1}}\right|\,\omega_{\alpha_k}\rangle}_{\delta_{\alpha_{k+1},\alpha'_{k+1}}}\\
&= \sum_{\substack{n_k,n'_k\\ \alpha_k,\,\alpha_{k+1}}} A^{n'_k *}_{\alpha_k,\alpha_{k+1}}\,\langle n'_k|\,\hat{O}_k\,|n_k\rangle\,A^{n_k}_{\alpha_k,\alpha_{k+1}} = \sum_{\substack{n_k,n'_k\\ \alpha_k,\,\alpha_{k+1}}} A^{n'_k *}_{\alpha_k,\alpha_{k+1}}\mathcal{O}^k_{n'_k,\,n_k}A^{n_k}_{\alpha_k,\alpha_{k+1}},
\end{aligned} \tag{3.14}$$

where we used the orthogonality properties previously defined. We are now able to introduce the concept of transfer matrix $\mathbb{E}$ of the operator $\hat{O}_k$ acting on the site k as shown in Fig. (3.9).

$$\mathbb{E}(\hat{O}_k) \equiv \textstyle\sum_{n_k,\,n'_k} B^{n'_k *}_{\alpha'_k,\,\alpha'_{k+1}}\,\mathcal{O}_{n'_k,\,n_k}B^{n_k}_{\alpha_k,\,\alpha_{k+1}} \quad =$$

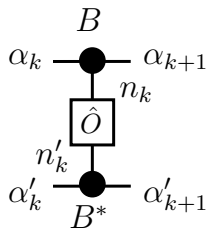

Figure 3.9: General transfer matrix for a local operator $\hat{O}_k$ acting on the site k of a *MPS*.

This constitutes the core of the *MPS* numerical method and contains all the local information when performing any type of measurement over the tensor chain representing a physical system. For extracting this overall calculation over the system it is necessary to propagate the contribution of the local transfer matrices, for this we trace over the connecting indices resulting in a complex number corresponding to the expectation value of the local operator over the system state. It is much easier to visualize how this is expressed in the transfer matrix language using the graphical representation, as shown in Fig [3.10]. Note that Fig. (3.10) corresponds to $\mathbf{Tr}\left[\delta_{\alpha_k}^{\alpha'_k}\mathbb{E}(\hat{O}_k)\delta_{\alpha_{k+1}}^{\alpha'_{k+1}}\right]$,

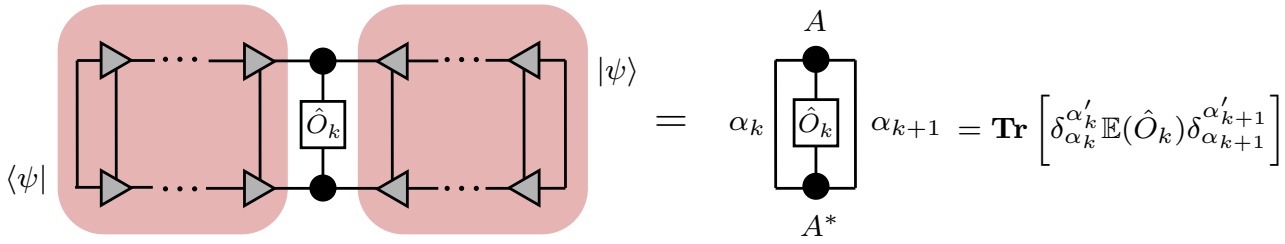

Figure 3.10: Graphical representation of the expectation value $\langle\Psi|\,\hat{O}_k\,|\Psi\rangle$ using a mixed-canonical state form and a local operator.

where we identified $B = A$ and we are tracing over indices α_k and α_{k+1}. Last result proves how the *MPS* in the orthogonal form simplifies the amount of tensor contractions necessary to compute an expectation value due to the reduction of the left and right orthogonal tensors in the chain.

Norm of the state.

The norm of the state is equivalent to taking the local operator as the identity in Eq. (3.10), this is

$$\langle\Psi|\,\Psi\rangle = \mathbf{Tr}\left[\delta_{\alpha_k}^{\alpha'_k}\mathbb{E}(\hat{I}_k)\delta_{\alpha_{k+1}}^{\alpha'_{k+1}}\right]. \tag{3.15}$$

Having the norm of the state, we are now able to write the state in the more convenient orthonormal form by taking a orthogonalized representation as in Fig. (3.8) and dividing each site tensor elements by the square root of the norm, resulting in a more suitable form for performing calculations such as dynamical evolution of the system.

Correlation functions.

In 1D strongly correlated systems, it is desirable to perform measurements using non-local operators such as in the case of correlations, which in general have the form $G_\Delta = \langle\hat{O}_1^k\hat{O}_2^{k+\Delta}\rangle$, where operators $\hat{O}_1^k$ and $\hat{O}_2^{k+\Delta}$ are different operators acting on different sites of the system,. We choose the

orthogonality center of the state in k-th site such that it matches with the site of first observable. The correlation function, whose numerical resources increases notoriously with respect to any other local observable written in terms of the canonical *MPS* is given by

$$\langle \hat{O}_1^k \hat{O}_2^{k+\Delta} \rangle = \mathbf{Tr}\left[\mathbb{E}(\hat{O}_1^k) \left(\prod_{i=k+1}^{k+\Delta-1} \mathbb{E}(\hat{I}^i) \right) \mathbb{E}(\hat{O}_2^{k+\Delta}) \right]. \tag{3.16}$$

The graphical representation of the correlation function is presented in Fig. (3.11). The amount of

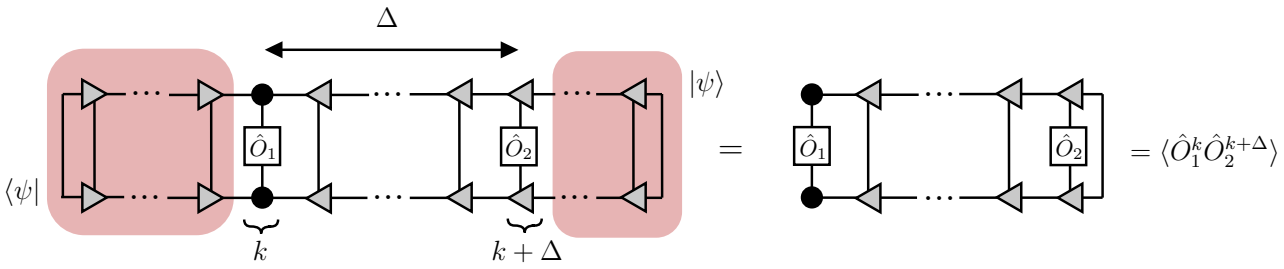

Figure 3.11: Graphical representation of the correlation function $\langle \hat{O}_1^k \hat{O}_2^{k+\Delta} \rangle$.

tensor contractions necessary to compute the correlation function gives an insight on the complexity of this procedure. This problem can be tackled by recurring to tools such as the Matrix Product Operators (*MPO*), which allows us to express non-local operators as a product of local operators, significantly reducing the required computational effort to perform measurements. On the next chapter we will focus on exploring this new formalism, highlighting its details and advantages in the process of extracting information from our physical system.

3.3 Matrix Product Operators

So far, we have discussed some of the advantages of working with the *MPS* representation when performing measurements over local-acting observables, now consider we have a system described by a Hamiltonian $\hat{H}$, we aim to find a representation that allows us to simplify the calculation of expectation values involving the Hamiltonian. This lead us to the Matrix Product Operators (*MPOs*), a form of representing an operator similar to the *MPS*, that allows us to express the Hamiltonian or any operator as a product of local operators each acting on one site of the *MPS*, simplifying a lot the way of calculating expectation values by reducing the computational effort needed and creating an optimal numerical environment for parallelization improvements in the numerical method.

Let us consider an operator written in its most general form in the Fock basis:

$$\hat{O} = \sum_{\substack{n_1,\ldots,n_L \\ n'_1,\ldots,n'_L}} c_{n_1,\ldots,n_L,n'_1,n'_L} |n_1,\ \ldots,\ n_L\rangle\langle n'_L,\ \ldots,\ n'_1|. \tag{3.17}$$

We perform the same procedure as in the *MPS*, iteratively applying the *SVD* on the probability amplitude coefficient and taking similar considerations. The resulting *MPO* and its graphical representation are presented in Fig. (3.12).

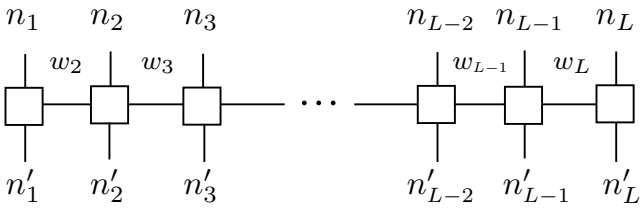

$$, \quad \hat{O} = \sum_{\substack{n_1,\ldots,n_L \\ n'_1,\ldots,n'_L \\ w_2,\ldots,w_{L-1}}} W^{n'_1,\,n_1}_{w_1,\,w_2} \ldots W^{n'_L,\,n_L}_{w_L,w_{L+1}} |\boldsymbol{n}'\rangle\langle\boldsymbol{n}|.$$

Figure 3.12: Simplified expression and graphical Penrose diagram of the *MPO*. $w_1 = w_{L+1} = 1$ as in the *MPS*.

With the *MPO* representation of the operator given by Fig. (3.12) and the *MPS* form of the state given by Fig. (3.7) we can express the expectation value of the operator as follows:

$$\begin{aligned}\langle\psi|\hat{O}|\psi\rangle = &\left(\sum_{\substack{\alpha'_1,\ldots,\alpha'_L \\ n'_1,\ldots,n'_L}} A^{n'_1 *}_{\alpha'_1,\alpha'_2} A^{n'_2 *}_{\alpha'_2,\alpha'_3} \ldots A^{n'_L *}_{\alpha'_L,\alpha'_{L+1}} \langle\boldsymbol{n}'|\right)\left(\sum_{\substack{n_1,\ldots,n_L \\ n'_1,\ldots,n'_L \\ w_2,\ldots,w_L}} W^{n'_1,\,n_1}_{w_1,\,w_2} \ldots W^{n'_L,\,n_L}_{w_L,w_{L+1}} |\boldsymbol{n}''\rangle\langle\boldsymbol{n}'''|\right) \\ &\times\left(\sum_{\substack{\alpha_1,\ldots,\alpha_L \\ n_1,\ldots,n_L}} A^{n_1}_{\alpha_1,\alpha_2} A^{n_2}_{\alpha_2,\alpha_3} \ldots A^{n_L}_{\alpha_L,\alpha'_{L+1}} |\boldsymbol{n}\rangle\right).\end{aligned} \tag{3.18}$$

After considering the orthogonality of the basis elements and grouping terms we have

$$\begin{aligned}\langle\psi|\hat{O}|\psi\rangle = \sum_{\substack{\alpha_1,\ldots,\alpha_L \\ \alpha'_1,\ldots,\alpha'_L \\ w_1,\ldots,w'_L}} &\left(\sum_{n_1,n'_1} A^{n'_1 *}_{\alpha'_1,\alpha'_2} W^{n'_1,n_1}_{w_1,w_2} A^{n_1}_{\alpha_1,\alpha_2}\right)\left(\sum_{n_2,n'_2} A^{n'_2 *}_{\alpha'_2,\alpha'_3} W^{n'_2,n_2}_{w_2,w_3} A^{n_1}_{\alpha_2,\alpha_3}\right) \\ &\ldots\left(\sum_{n_L,n'_L} A^{n'_L *}_{\alpha'_L,\alpha'_{L+1}} W^{n'_L,n_L}_{w_L,w_{L+1}} A^{n_L}_{\alpha_L,\alpha_{L+1}}\right).\end{aligned} \tag{3.19}$$

We define the general transfer matrix for the *MPO* acting on site k as shown in Fig. (3.13). Note

$$\mathbb{E}(\hat{O}_k) \equiv \sum_{n_k,\, n'_k} A^{n'_k *}_{\alpha'_k,\, \alpha'_{k+1}} W^{n'_k, n_k}_{w_k, w_{k+1}} A^{n_k}_{\alpha_k,\, \alpha_{k+1}} \quad =$$

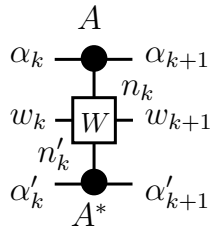

Figure 3.13: General transfer matrix for a MPO contraction with a MPS.

that, despite appearing to be similar to the regular transfer matrix, this general form has six non-contracted indices. This marks a huge difference in the contractions needed to calculate an expectation value when considering the product of neighbor-sites transfer matrices and thus in the numerical method implementation logic. The handling of this six-indices object is part of the main results of this work, creating a **C++** library for handling *MPO* implementations in *MPS* algorithms. All the expressions with the general transfer matrix adopt the same form as with the regular case with the consideration that **Tr** also acts over the virtual indices of the *MPO*. The graphical representation of the expectation value of Eq. (3.19) is presented in Fig. (3.14). We can

$$\langle\psi|\,\hat{O}\,|\psi\rangle =$$

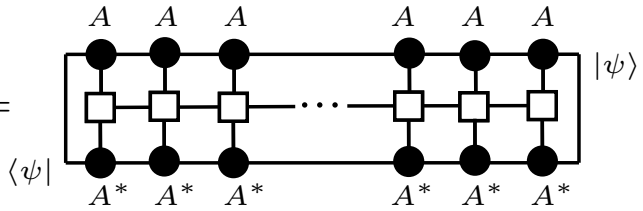

Figure 3.14: Graphical representation of the expectation value $\langle\Psi|\,\hat{O}\,|\Psi\rangle$ in the *MPO* representation.

express the Hamiltonian as a site independent *MPO* represented by a single matrix expressed in Schur's form [68], this is a lower triangular matrix that yields in the Hamiltonian when multiplied iteratively. Given a Hamiltonian that contains only 1-site local terms and nearest-neighbor terms, we can express it as a *MPO* as follows:

$$\hat{H} = \sum_{i=1}^{L} \hat{X}_i \hat{Y}_{i+1} + \sum_{i=1}^{L} \hat{Z}_i = W_0 W_1 \dots W_{L-1} W_{L+1}, \tag{3.20}$$

where W_0 and W_{L+1} were introduced as virtual components for reproducing the final scalar form of

the Hamiltonian, we have:

$$W_0 = \begin{pmatrix} 0 & 0 & \hat{I} \end{pmatrix}, \quad W_i = \begin{pmatrix} \hat{I} & 0 & 0 \\ \hat{Y}_i & 0 & 0 \\ \hat{Z}_i & \hat{X}_i & \hat{I} \end{pmatrix}, \quad \text{and} \quad W_{L+1} = \begin{pmatrix} \hat{I} \\ 0 \\ 0 \end{pmatrix}. \tag{3.21}$$

Each component has dimension d, representing the local degrees of freedom in the system. Generally, the matrices W have dimensions $M \times M$, where M depends on the specific amount of terms in the Hamiltonian. A key advantage of representing these matrices in a Schur lower triangular form is the ability to construct more complex terms from known *MPOs* as internal components. For instance, the resulting *MPO* for a sum of terms is simply the direct sum of the *MPO* component matrices, while for a product of terms is given by the tensor product of those matrices, both of which maintain the lower triangular form, while increasing the virtual dimension of the final representation. Moreover, operators such as correlation functions and local observables can also be expressed in the *MPO* form, which simplifies calculations that would otherwise be computationally demanding in the standard *MPS* approach. For instance, in the *MPS* case, evaluating measurements involving two-site operators, such as the hopping term in Eq. (2.34), requires explicitly constructing the matrix representation in the two-site local basis. In the superfluid regime with $m = 16$ basis states (considering up to two particles per site), this traduces to manually expressing a large matrix of dimension 256×256 for the hopping operator. In contrast, the *MPO* formalism leverages its local-invariant structure: one works only with the local representation (16×16), while the propagation of correlations is naturally handled through the virtual entanglement indices of the *MPO*.

We implemented the *MPS* and *MPO* formulations to compute local observables and correlation functions in different spin models, following the contraction schemes described in the previous sections. These calculations were performed on ground states of different systems obtained using a variational *MPS* method.

3.4 Infinite MPS (iMPS)

There is a particular case of the *MPS*, where it is represented by an infinite array of tensors which are invariant under translation of one cell, reducing a lot the wave function parameters and presenting an even more effective form for calculating observables of the system in the thermodynamic limit as proposed by G. Vidal [45].

Consider the infinite generalization of the *MPS* given by Eq. (3.11), henceforth called *iMPS*, this is:

$$|\Psi\rangle = \sum_{\substack{\{\alpha\}\\\{n\}}} \ldots \Gamma^{n_{i-1}}_{\alpha_{i-1},\,\alpha_i} \lambda_{\alpha_i} \Gamma^{n_i}_{\alpha_i,\,\alpha_{i+1}} \lambda_{\alpha_{i+1}} \Gamma^{n_{i+1}}_{\alpha_{i+1},\,\alpha_{i+2}} \lambda_{\alpha_{i+2}} \Gamma^{n_{i+2}}_{\alpha_{i+2},\,\alpha_{i+3}} \ldots |\vec{n}\rangle\,, \tag{3.22}$$

where λ and Γ are repeated throughout the whole chain for every lattice site. These tensors have bound dimension χ, which plays a role as a refinement parameter for the *MPS*. We can write the *iMPS* in the mixed canonical form and express it as a finite *MPS* with the boundary contracted tensors corresponding to the left and right semi-infinite sub-lattices, as shown in Fig. (3.15). This

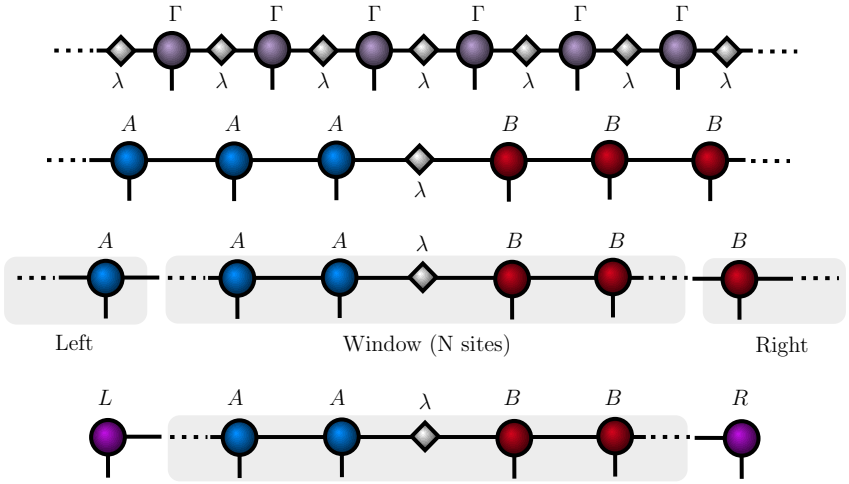

Figure 3.15: Separation scheme for the *IMPS*.

train of ideas allows to decompose the Hamiltonian of the infinite chain into five components, as

$$\hat{H} = \hat{H}_L + \hat{H}_{LW} + \hat{H}_W + \hat{H}_{WR} + \hat{H}_R, \tag{3.23}$$

where $\hat{H}_L$ and $\hat{H}_R$ are the effective Hamiltonians for the left and right semi-infinite sub-lattices, $\hat{H}_{LW}$ and $\hat{H}_{LW}$ are the interaction terms of the sub-lattices with the window and $\hat{H}_W$ is the Hamiltonian for the window with N sites. We can use the boundary conditions of the infinite system to reduce it to a finite one, reducing the information contained in the Hamiltonian to the effective one describing the finite chain.

$$\hat{\tilde{H}} = \hat{\tilde{H}}_L + \hat{\tilde{H}}_{LW} + \hat{H}_W + \hat{\tilde{H}}_{WR} + \hat{\tilde{H}}_R, \tag{3.24}$$

where $\hat{H}_W$ remained unchanged.

The *iMPS* approach enables the study of systems with periodic boundary conditions directly in the thermodynamic limit. However, determining the effective left and right environment effective Hamiltonians requires computing the dominant super-vectors of the corresponding transfer matrices, a task that lies beyond the scope of the present work. Nevertheless, it remains an important direction for future research related to this work. On the following chapter, we focus on the numerical aspects of implementing the *MPO* and *MPS* theoretical formalisms developed along this chapter, expecting the lector grasps the intrinsic complexity that underlies the numerical implementation of this methods the seemingly simple theoretical formulation.

Chapter 4

Numerical implementation

In the last chapter we introduced the theoretical formalism of Matrix Product States and Operators, we now focus on the numerical implementation of the contractions and procedures required to perform calculations involving expectation values described previously, useful for obtaining relevant information of the system, i.e. observables, correlations, ground state energy and time evolution.

4.1 MPS implementation

Lets start by addressing the numerical treatment of the states, for this, a proper storage of the elements $A^{n_s}_{\alpha_s,\,\alpha_{s+1}}$ that constitute the *MPS* is essential for efficient computation. To achieve this, we define a general block matrix $\mathbb{A}$ that systematically arranges the information corresponding to the physical sites of the lattice and the local basis elements. This structure facilitates efficient data access using the so-called *fast indices*, which traverse the vertical and horizontal blocks in steps of the bond (also called virtual) dimension M, and the *slow indices*, which sweep through the internal elements of each A matrix, this is illustrated in Fig. (4.1). An useful analogy is to think of

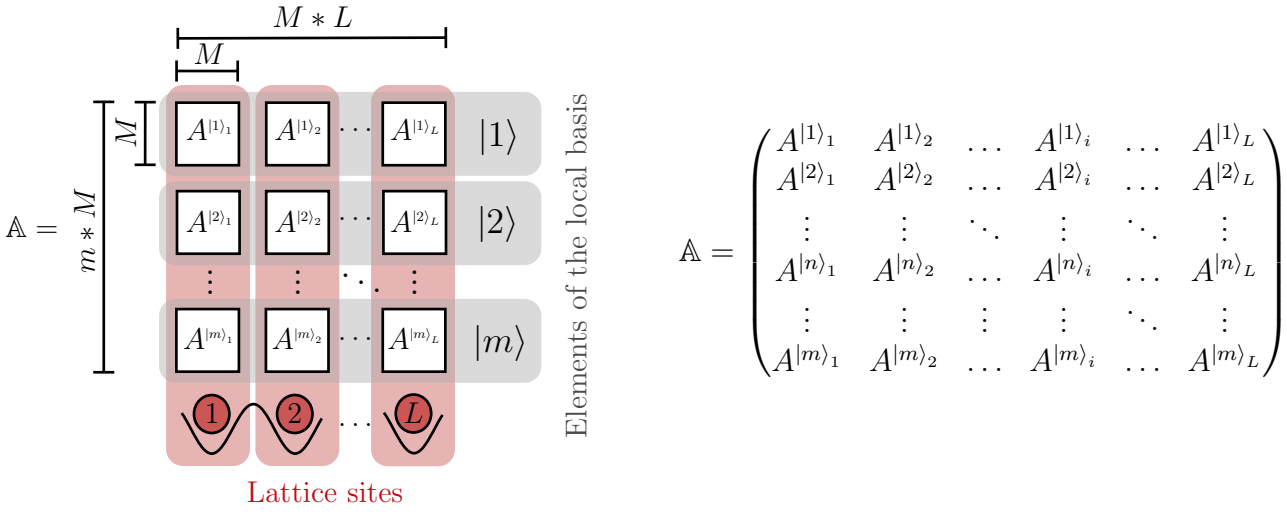

$$\mathbb{A} = \begin{pmatrix} A^{|1\rangle}{}_1 & A^{|1\rangle}{}_2 & \dots & A^{|1\rangle}{}_i & \dots & A^{|1\rangle}{}_L \\ A^{|2\rangle}{}_1 & A^{|2\rangle}{}_2 & \dots & A^{|2\rangle}{}_i & \dots & A^{|2\rangle}{}_L \\ \vdots & \vdots & \ddots & \vdots & \ddots & \vdots \\ A^{|n\rangle}{}_1 & A^{|n\rangle}{}_2 & \dots & A^{|n\rangle}{}_i & \dots & A^{|n\rangle}{}_L \\ \vdots & \vdots & \vdots & \vdots & \ddots & \vdots \\ A^{|m\rangle}{}_1 & A^{|m\rangle}{}_2 & \dots & A^{|m\rangle}{}_i & \dots & A^{|m\rangle}{}_L \end{pmatrix}$$

Figure 4.1: Structure of the general block matrix $\mathbb{A}$.

a library where we are interested in picking a specific book. The *fast indices* act like identifiers for the bookshelf location in the library aisles, while the *slow indices* specify the exact row and column where the book is placed. After looking at the importance of the transfer matrix $\mathbb{T}$ in calculations involving measurements over the state, we can undoubtedly affirm that it constitutes the heart of this technique. From Eq. (3.10), we know that any on-site calculation is ultimately represented by a recursion of a generic expression where the only change between sites is the acting operator and the corresponding element of the state, as seen in Fig. (3.8) and Fig. (3.11), taking care of contracting the adequate indices in the left and right ends of the chain. The computational procedure for calculating the transfer matrix involves an initial reshape of the matrices before and after performing the matrix multiplication in order to match the dimensions for contraction. The numerical scheme for the simplest transfer matrix (Identity as the local operator) for a lattice site k is presented in Fig. (4.2). Note that, in order to match the original structure, E_{-} must be

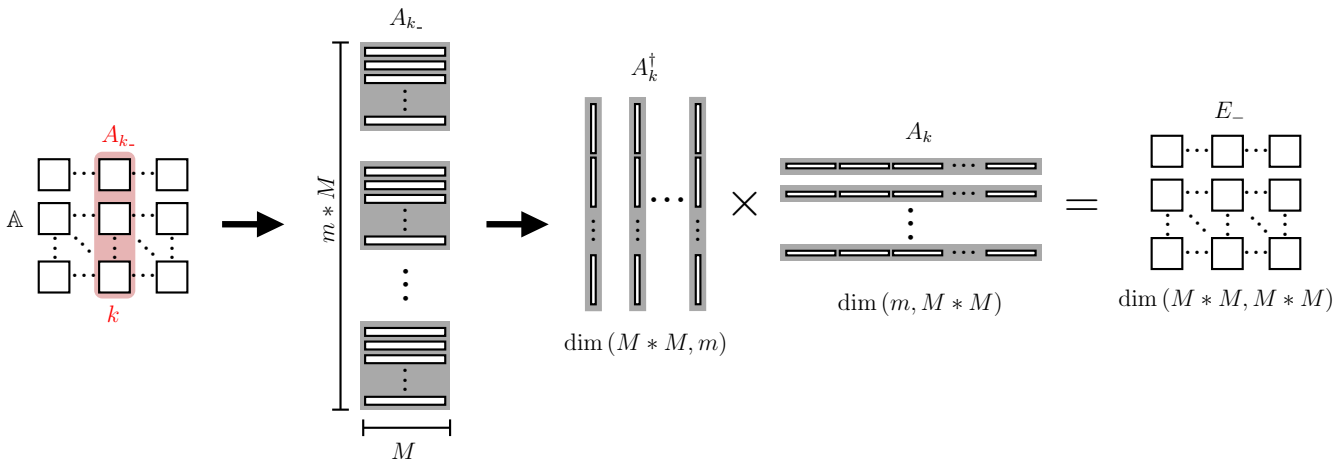

Figure 4.2: Local transfer matrix computation protocol for the identity operator.

reshaped following a *transpose-similar block protocol* as shown in Fig. (4.3). This results in E, which corresponds to the site k transfer matrix with $\hat{O}_k = \hat{I}_k$. The whole transfer matrix numeric procedure is summarized in Appendix C.

Recall from Fig. (3.7) the inclusion of the two auxiliary indices α_1 and α_{L+1} introduced for maintaining the dimension structure of the *MPS* elements in the boundary, this is numerically conducted by using the *correction protocol* represented in Fig. (4.4). Note that only the first of the rows (columns) from the first (last) site matrix is preserved, this ensures $\alpha_1 = \alpha_{L+1} = 1$, the rest of the information is replaced by zeros as expected due to the lack of entanglement of the border sites with its neighbor (left or right) component of the system in the finite *MPS* case. Even if the state

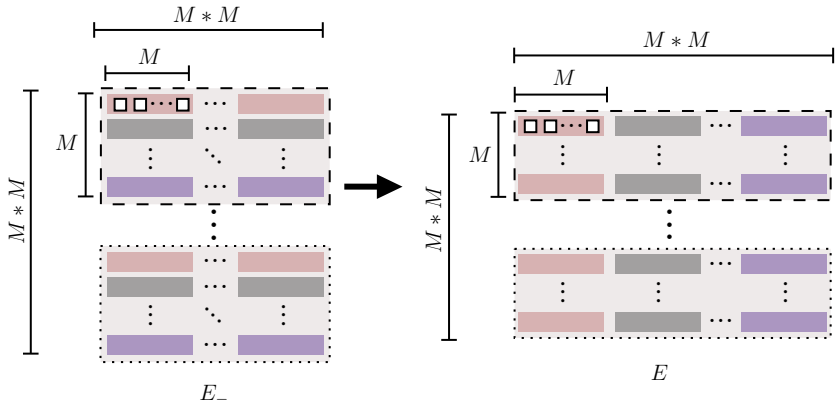

Figure 4.3: Reshaping protocol for E matrix .

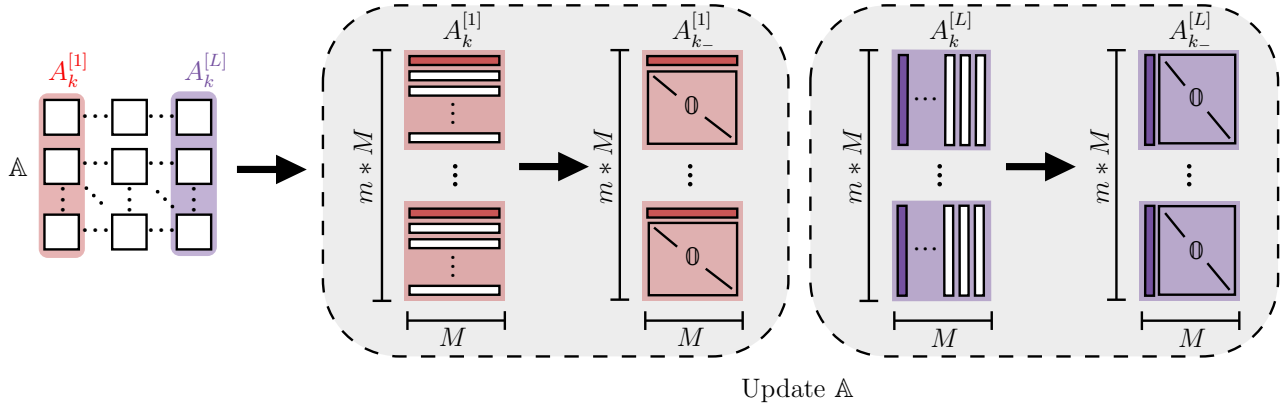

Figure 4.4: Correction protocol for $\mathbb{A}$ matrix .

contains information in the neglected blocks (as in a randomly generated initial state), it is safe to remove it without causing any computational errors. Now that we know how to operate the transfer matrix with the identity operator, we are able to compute the analogue case for any local operator $\hat{O}_k$ acting on site k, for this we follow the same procedure as in Fig. (4.2), with the only difference that we previously apply the matrix representation of the operator on the $A_{k\_}$ matrix containing the information of the ket, this is $\hat{O}_k |\psi\rangle$, and is obtained using the protocol depicted in Fig. (4.5), where the squared operator $\hat{O}$ row elements (complex numbers) are multiplied with the whole $M \times M$ block corresponding to each one of the physical index values (matched with color schemes in figure) and then, the resulting matrices are summed together to result in $\hat{O}A_{k\_}$, which represents the operator applied on the local site k of the many body state $|\psi\rangle$. We now have the capacity to calculate any expectation value involving local operators acting on any physical site of the lattice with the *MPS* expressed in any of the orthogonal forms. After computing the transfer

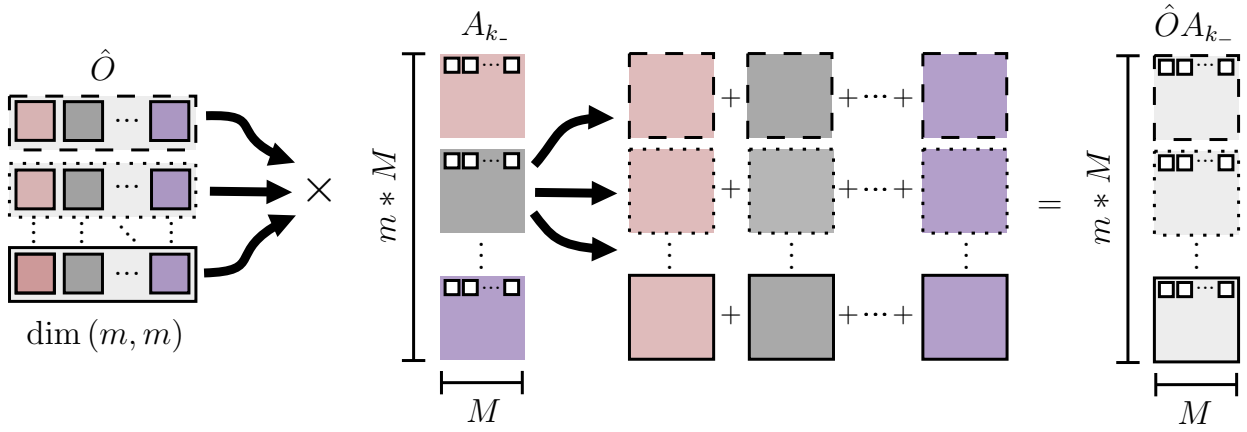

Figure 4.5: Operator to tensor application protocol.

matrices for all the sites of the chain we only need to perform the product between site matrices and trace over the result, as expressed in Eq. (3.16). Note that the condition $\alpha_1 = \alpha_{L+1} = 1$ implies a different trace structure on the first and last lattice sites, this is represented for the left site in Fig. (4.6) and for the right site in Fig. (4.7).

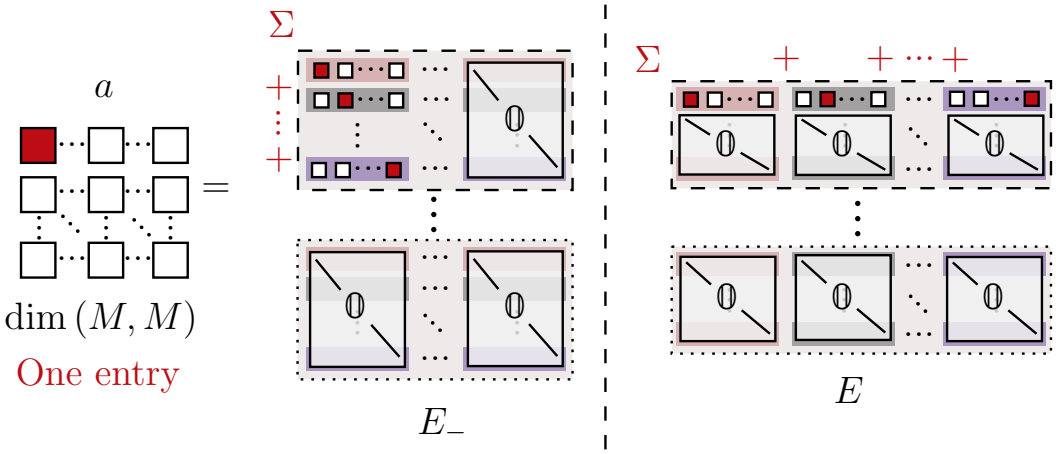

Figure 4.6: Left-trace of the transfer matrix corresponding to the first lattice site .

4.2 MPO implementation

The main contribution of the present work to the theoretical solid state physics research group is to implement the *MPO* formalism numerically in a low-level programming language as **C++** in order

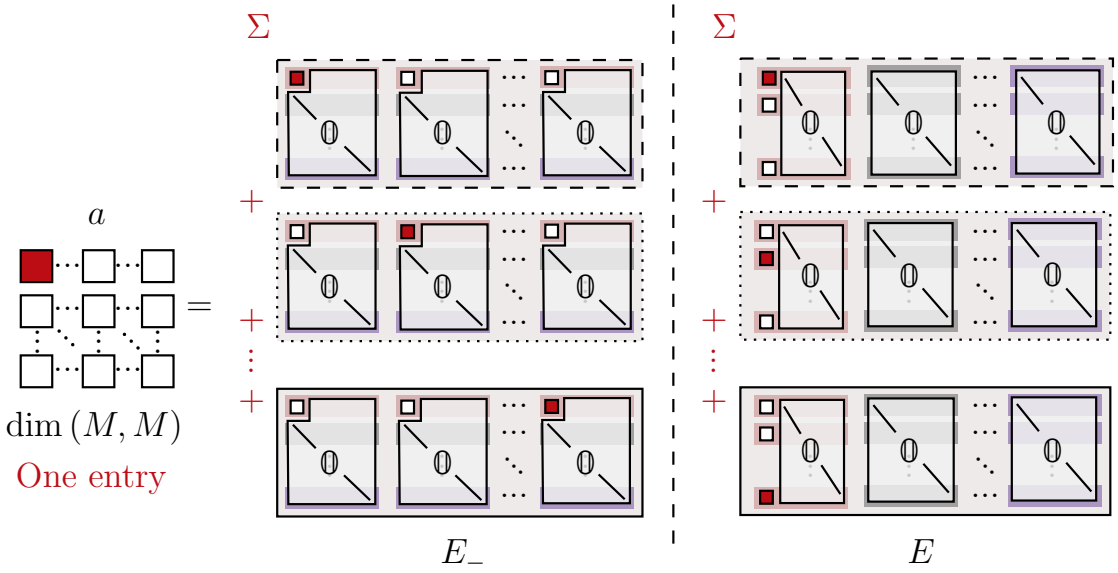

Figure 4.7: Right-trace of the transfer matrix corresponding to the last lattice site .

to exploit the advantage of representation that this technique offers, as it allows to express non-local operators as a tensor train of identical local-acting operators, henceforth allowing to simplify the numerical expression of non-trivial hamiltonians as in the Bose-Hubbard case. This technique also offers the possibility of parallelizing the code due to the homogeneity of the local expressions acting on each site, optimizing the computational effort necessary to compute measurements of correlations, time evolutions and local observables. After having introduced all the relevant numerical protocols employed in the numerical implementation of a system represented by a *MPS*, we can now focus on the Matrix product Operators numerical implementation.

A general *MPO* is represented as shown in Fig. (3.12), with each of its components represented as matrix with dimension $W \times W$, where W is defined as the *MPO* virtual dimension, and depends explicitly on the specific chosen representation of the *MPO* (there's not a unique representation). In analogy to the *MPS* numerical treatment, the *MPO* handling also requires computing the transfer matrix, which in this case includes two extra contracted indices corresponding to the newly introduced virtual dimensions, as shown in Fig. (3.13). This can be achieved by recursively relying on the protocols previously established for *MPS* manipulation, much like nesting elements in a Russian doll.

The *MPO* general transfer matrix computation protocol is illustrated in Fig. (4.8), where first the operator *MPO* representation is flattened in a row structure, posteriorly the local operators are applied to the corresponding *MPS* elements as depicted in Fig. (4.5) and the information is stored

in a major-column array (Note the transposition in the figure), afterwards the local transfer matrix is calculated as in Fig. (4.2) for each operator while keeping the major-column form. Finally, the result is an array of local transfer matrices which can be contracted tracing over the local matrices (α_i) and then tracing over the *MPO* degrees of freedom between sites (w_i) for $i \in [0, L]$, being L the number of sites. Now that we have implemented a method to compute the general transfer matrix

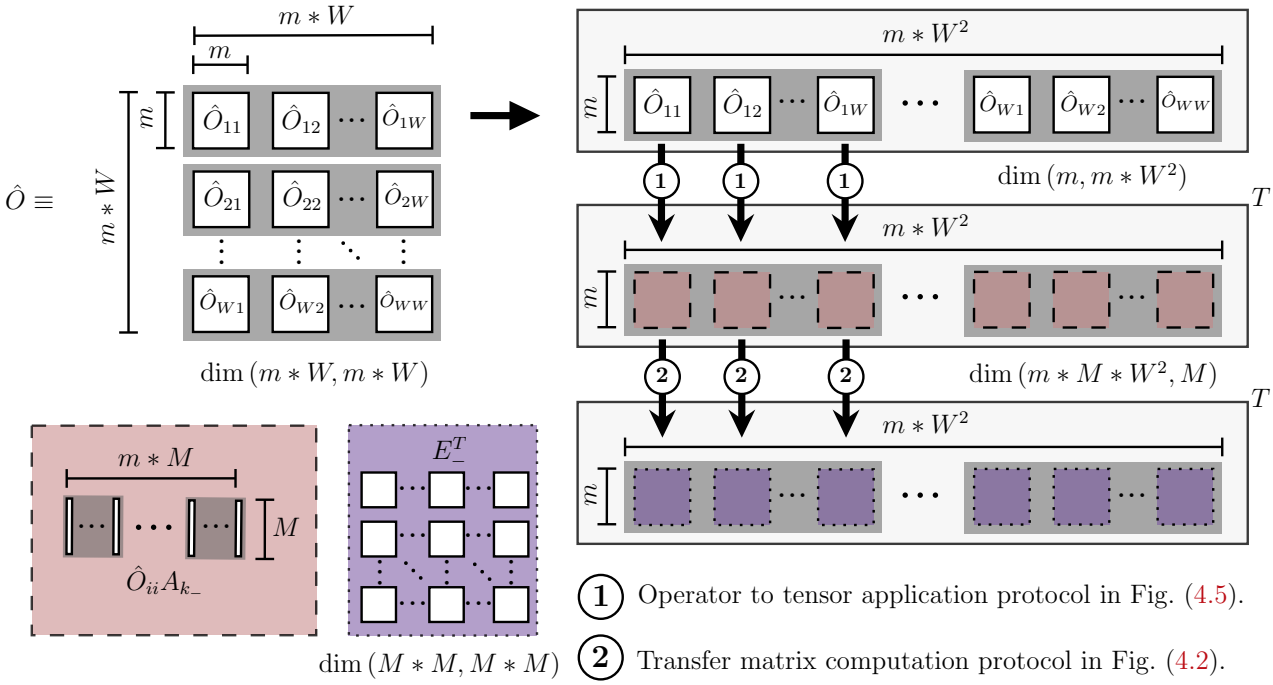

Figure 4.8: *MPO* transfer matrix computation protocol.

for arbitrary Matrix Product Operators, being able to perform calculations involving either local or non-local observables. The developed procedure is general such that it includes the evaluation of correlation functions, the energy of a given state, and Hamiltonians with non-local terms (as hopping), while maintaining a local representation. Having described the numerical technique to work with, we move on to using it with the objective of implementing the observables written in the *MPO* form to characterize states written as *MPS* for a variety of physical systems. Hence, Chapter 5 presents the results obtained by applying the developed numerical techniques in order to characterize properties such as particle number and magnetization in the ground state of two different preliminary models.

Chapter 5

Numerical results in spin systems

Using the theoretical formalisms of Matrix product States (*MPS*) and Operators (*MPO*) developed on Chapter 3 and employing the numerical implementations described in Chapter 4 we are able to characterize multiple states corresponding to two Hamiltonians including relevant features such as external magnetic fields and synthetic spin-orbit couplings.

We started by performing a benchmarking of the results of the code implementation with the *MPO* formalism, performing multiple characterizations over different models such as the Bilinear-Biquadratic Heisenberg model and the generalized Fermi-Hubbard model, ranging over a vast group of states, among them we work with Mott-insulating states with spin-1 bosons and superfluid states with spin-$\frac{1}{2}$ fermions. We varied parameters such as the the number of sites L, the virtual dimension of the *MPS*, namely M and intrinsic physical parameters such as hopping strengths J, quadratic magnetic field strengths D, spin-orbit coupling magnetic field associated to the parameter α, among others.

5.1 Mott Insulator

The first benchmarking results are obtained by characterizing the spin-1 Mott-Insulator ground state within the bilinear-biquadratic Heisenberg model [69] in presence of a quadratic Zeeman field, described by Hamiltonian in Eq. (5.1). To this end, we employed the *MPO* representation of the Hamiltonian and compared our results with previously reported calculations based on the conventional *MPS* approach.

In order to contextualize these simulations, we briefly summarize the main features of the model. In Eq. (5.1), $\langle i, j\rangle$ denotes the sum over the nearest neighbors, J is the hopping strength, D is a quadratic Zeeman field and θ is a function of the interaction energies between bosons per site. In presence of the external quadratic field, several phases appear, this have been subjected to study using different approaches [70, 71, 72]. One case worth to mention due to its experimental relevance is the balanced mixture, where the total magnetization vanishes. This was discussed by *Rodriguez et al.* [73] and the phase diagram is presented in Fig. (5.1).

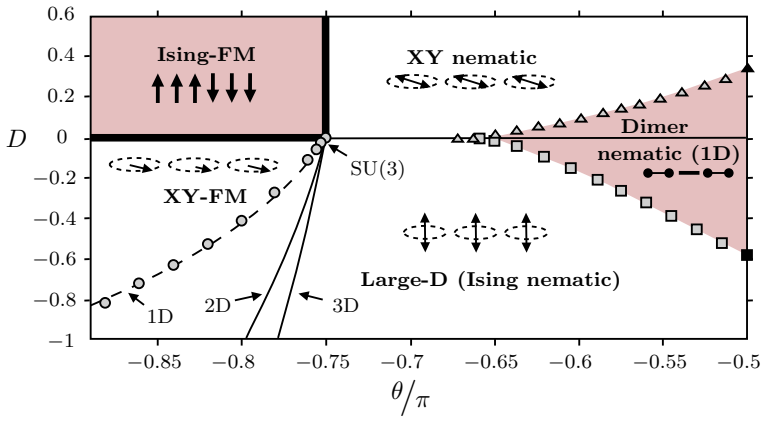

$$\hat{H}_{BBQ} = J \sum_{\langle i,j \rangle} \left[\cos\theta \left(\hat{\vec{S}}_i \cdot \hat{\vec{S}}_J \right) + \sin\theta \left(\hat{\vec{S}}_i \cdot \hat{\vec{S}}_j \right)^2 \right] - JD \sum_i (\hat{S}_i^z)^2, \quad (5.1)$$

Figure 5.1: Magnetic phases of the bilinear-biquadratic Heisenberg model for a one-dimensional spin-1 chain as function of θ and D.

We characterize the Dimer-nematic phase of the bilinear-biquadratic Heisenberg model using the *MPO* numerical implementation and comparing with the *MPS* calculations, presenting measurements of magnetic profiles, local observables and correlation functions while considering parameters $J = 1$, $\hbar = 1$ fixed for all the simulations. The Dimer-nematic phase appears for $\theta \in [-\frac{3\pi}{4}, -\frac{\pi}{4}]$. The simulations were performed considering a restricted Hilbert space of at most one particle per lattice site and an external field with intensity $D = -0.6$, with fixed $\theta = -0.6\pi$ (see Fig [5.1]).

As a first diagnostic, we examined local observables such as the populations of each magnetic projection per site, as shown in Fig. (5.2). In the figure, the open and solid circles correspond to the numerical results obtained with the *MPO* implementation, while the solid lines correspond to the calculations performed with the standard *MPS* algorithm. The excellent agreement between both approaches demonstrates the consistency and reliability of the developed *MPO* measurement protocols.

The magnetic profile reflects the relevant physics of this regime: there is a clear prevalence of the zero magnetic projection across the lattice compared to the $|\pm 1\rangle$ states. This behavior is consistent with the tendency of the dimer-nematic phase to favor the quadrupolar state over the dipolar states in order to minimize its energy. Consequently, the magnetization is essentially zero, with a reported value of $\langle \hat{S}_z \rangle \approx -3.82e-17$, confirming the anti-ferromagnetic character of this phase going along with the balance mixture configuration.

Finally, we computed two-sites correlations in the ground state, shown in Fig. (5.3). The Mott insulating phase is characterized by strong on-site interactions, leading to a finite excitation gap that

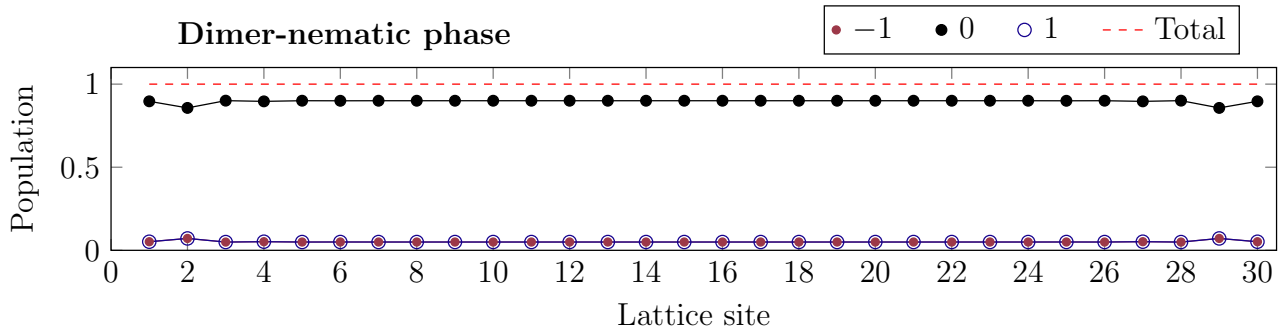

Figure 5.2: Magnetic profile of dimer-nematic phase of the **MI** with $L = 30$, $M = 12$, $\theta = -0.6\pi$ and $D = -0.6$. Characterized using the *MPO* representation **(dots)** in comparison with the standard *MPS* formalism **(solid lines)**.

suppresses particle number fluctuations. This behavior is manifested in the exponential decay of the two-site correlations measured and shown in Fig. (5.3). In this case, the open circles correspond to the *MPO* calculations, while the crosses denote the *MPS* results, showing again a one-to-one correspondence between the results sets for all the measurements. Note that the correlation distance ξ is obtained from the exponential fit of the data (dashed lines) and displayed on the panel showing

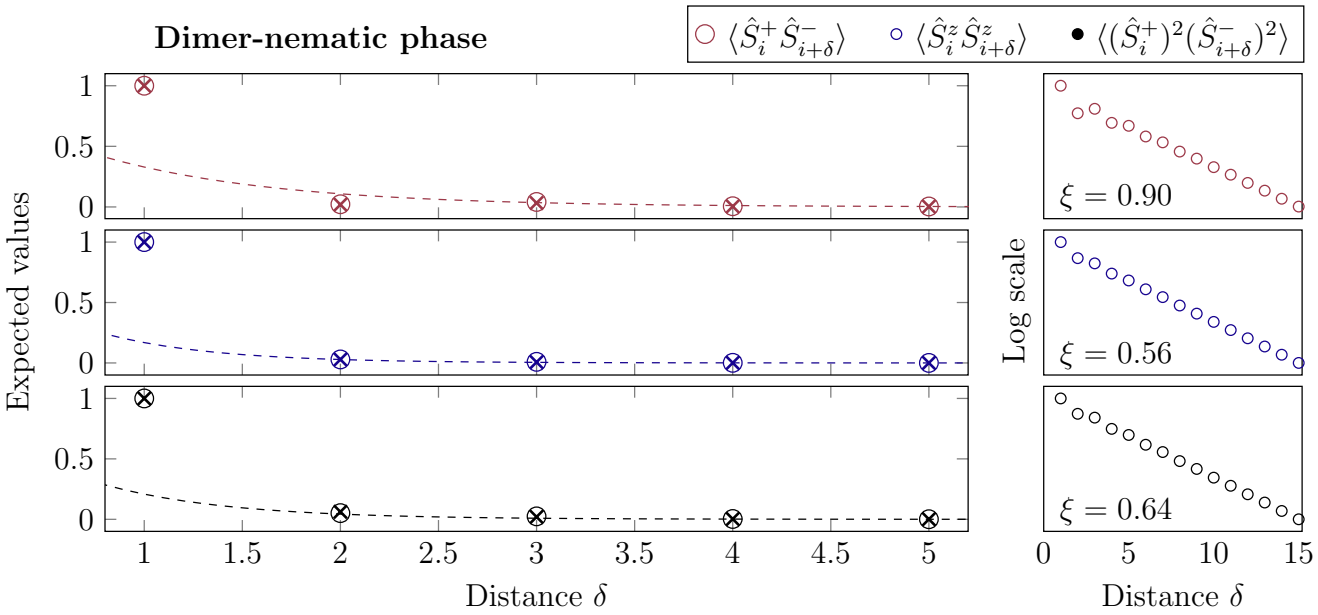

Figure 5.3: Correlation comparative in the ground state of the dimer-nematic phase with $L = 30$ and $M = 12$. Characterized using the *MPO* representation **(dots)** in comparison with the standard *MPS* formalism **(cross)**.

the linearized relation.

The transverse correlator $\langle \hat{S}_k^+ \hat{S}_{k+i}^- \rangle$ quantifies the degree of spin-flip coherence between distant lattice sites. Its exponential decay indicates that the effect of flipping a spin at site i has essentially no influence over site $i+\delta$. This behavior reflects the absence of $m = \pm 1$ magnetic projections in the ground state and confirms the lack of dipolar order.

The longitudinal correlator $\langle \hat{S}_i^z \hat{S}_{i+\delta}^z \rangle$ captures spin fluctuations throughout the chain. In this regime it decays rapidly to zero, consistent with the dominance of the interaction term over the hopping strength $U \gg J$, which prevents particle tunneling between the lattice sites.

Finally, the higher-order correlator $\langle (\hat{S}_i^+)^2 (\hat{S}_{i+\delta}^-)^2 \rangle$ probes the coherence of pairs of spin excitations instead of the individual ones, in other words, it measures whether creating a pair of spin-1 particles on site i is coherent with annihilating a pair on site $i+\delta$. Its exponential decay demonstrates that even pair coherence is suppressed. The system is thus firmly confirmed to be in a localized quadrupolar phase, consistent with the Dimer–nematic regime of the bilinear–biquadratic spin-1 Heisenberg model and indicating the measurements with the *MPO* are reliable.

5.2 Spin-$\frac{1}{2}$ system with spin-orbit coupling (*SOC*)

After benchmarking our results with the *MPS* calculations, we proceeded to explore a spin-$\frac{1}{2}$ system in the presence of an effective spin-orbit coupling given by the Hamiltonian in Eq. (5.2) [74].

$$\begin{aligned} \hat{H} = \sum_i \Big[-\frac{t}{2} \left(\hat{c}_i^\dagger \hat{c}_{i+1} + \text{h.c} \right) - (\mu - t) \hat{c}_i^\dagger \hat{c}_i - \frac{\alpha}{2} \left(i \hat{c}_i^\dagger \sigma_y \hat{c}_{i+1} + \text{h.c} \right) + \Delta \left(\hat{c}_{i,\uparrow} \hat{c}_{i,\downarrow} + \text{h.c} \right) \Big] \\ + U \sum_i \hat{n}_{i,\uparrow} \hat{n}_{i,\downarrow} + V \sum_i \hat{n}_i \hat{n}_{i+1}, \end{aligned} \tag{5.2}$$

where t is the hopping strength, μ the chemical potential, α the spin orbit coupling strength, B an external magnetic field, Δ the pair correlated term, U an on-site interaction, V is a nearest neighbor interaction and $\hat{c}_{i,\alpha}^{(\dagger)}$ are the spin-$\frac{1}{2}$ annihilation (creation) operators obeying the anti-commutation relation $\left\{ \hat{c}_{i,\alpha}^\dagger, \hat{c}_{j,\beta} \right\} = \delta_{i,j} \delta_{\alpha,\beta}$. In this case we measure observables on different ground states obtained using a *MPS* variational method with fixed values for the bond dimension $M = 25$, $L = 100$ lattice sites, and the physical parameters $\mu = 0.1$, $\alpha = 0.3$, $\Delta = 0.1$, $V = \frac{U}{2}$, while varying U to study the change on the magnetic profile and the behavior of multiple correlation functions of interest.

After considering a single site basis given by $|\emptyset\rangle, |\downarrow\rangle, |\uparrow\rangle, |\downarrow\uparrow\rangle$ the magnetic population profile of the ground state obtained by the simulations is presented in Fig. (5.4). Again, the measurements obtained with the *MPO* are in agreement with the standards *MPS* calculations. In this case, the

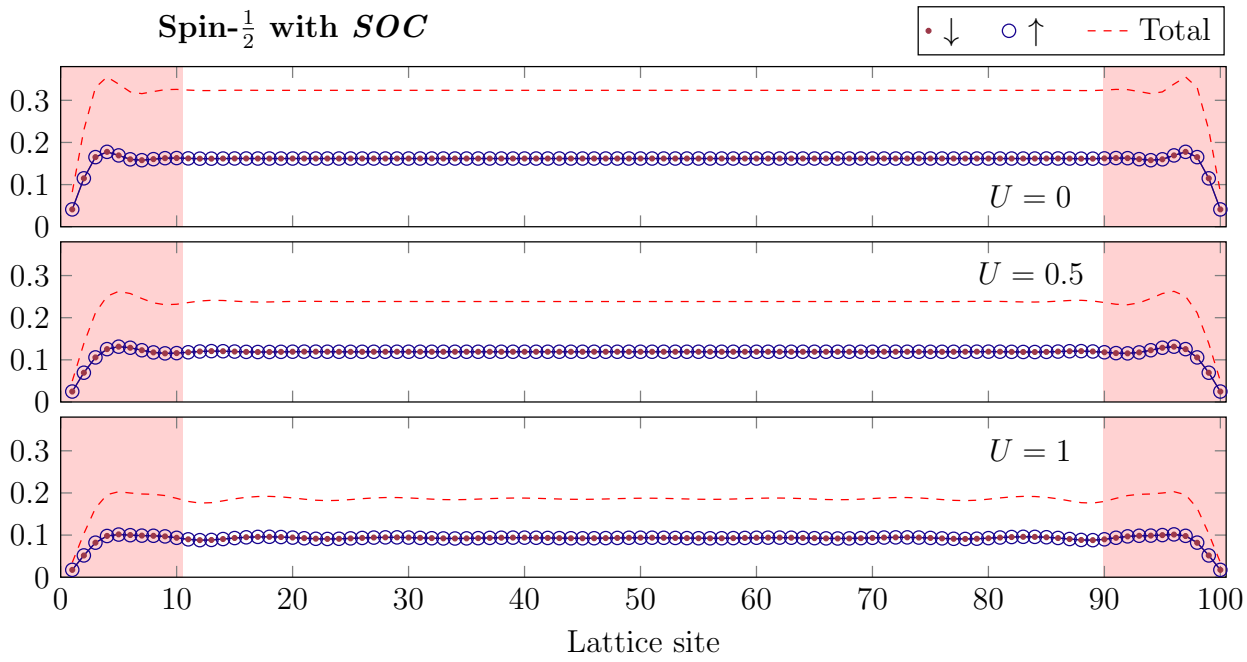

Figure 5.4: Magnetic profile of the spin-$\frac{1}{2}$ system of the **MI** with $L = 100$ and $M = 25$ characterized using the *MPO* representation. Where the **solid and open circles** correspond to the *MPO* measurements, and the **solid lines** correspond to the *MPS* calculations.

effects of the boundary conditions are reflected in the magnetic populations (see red highlighted region in Fig. (5.4)), being zero in the boundaries and rapidly increasing until reaching the stable regime observed in the middle of the lattice.

In this system, we define the superconducting (pair) operator as $\hat{\Delta}_i = \langle \hat{c}_{i,\uparrow}\hat{c}_{i,\downarrow}\rangle$, which annihilates a local Cooper pair on site i [75]. Its expectation value $\langle\hat{\Delta}_i\rangle$ is known as the superconducting order parameter, and is directly associated to the simultaneous breaking of the global $U(1)$ symmetry. The expectation value $\langle\hat{\Delta}_i\rangle \neq 0$ in the ground state, shows that the particle-number conservation in the ground state is not strictly fulfilled anticipating the presence of the formation of pairs.

We define the pair-pair correlator as $G_{\text{SC}} = \langle \Delta_i \Delta^{\dagger}_{i+\delta}\rangle$, which quantifies the coherence between annihilating a Cooper pair at site i and creating one at site $i + \delta$, with δ denoting the correlation distance. To minimize boundary effects, we evaluate the correlator by fixing i at the center of

the chain ($i = 49$) and varying $\delta \in [0, L)$, while discarding data points close to the lattice edges. The corresponding results are shown in Fig. [5.5]. Panel **(a)** displays the pair-pair correlator for weak interacting strength compared with hopping energy ($t = 1$ energy units), while panel **(b)** presents the pair-pair correlator for strongly interacting fermions. The dots represent the *MPO* calculations and the solid lines correspond to the *MPS* results. An excellent agreement between both approaches is observed.

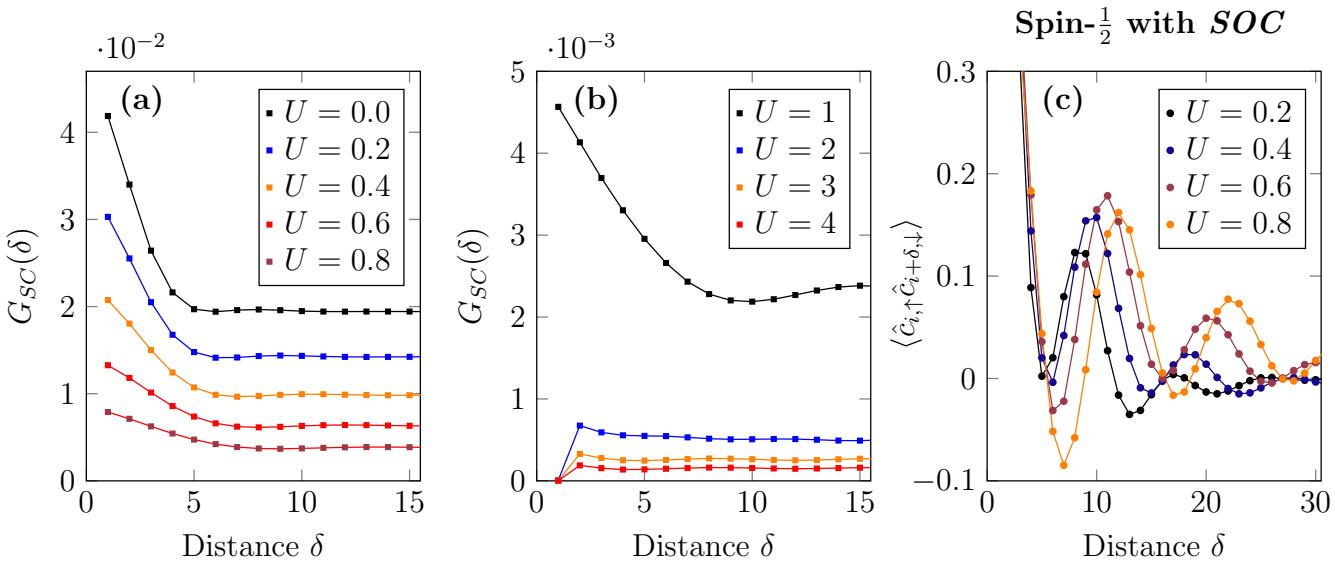

Figure 5.5: Pair-pair correlator (panels **(a)** and **(b)**) $G_{\mathrm{SC}}(\delta)$ and pairing correlator (panel **(c)**) as function of distance δ for different U values with $L = 100$, $M = 25$, $\Delta = 0.1$, $\alpha = 0.3$, $B = 0$ and $V = 0.5U$. Characterized using the *MPO* representation **(dots)** in comparison with the standard *MPS* formalism **(solid lines)**.

It is observed that $G_{\mathrm{SC}}(\delta)$ initially decays in the first sites, after which it reaches a saturation value. This asymptotic value decreases as the interaction strength U increases. To highlight this tendency, we compute the average value of $G_{\mathrm{SC}}(\delta)$ over the non-decaying region in Fig. (5.5) upper panel, denoted as $\bar{G}_{\mathrm{SC}}$ and plot it in addition with the density fluctuations $\langle \hat{n}_i^2 \rangle - \langle \hat{n}_i \rangle^2$ as function of U in Fig. (5.6) lower panel, observing again a high fidelity of the results in comparison with the *MPS* calculations.

The initial decay of $G_{\mathrm{SC}}(\delta)$ reflects how local Cooper pairs lose coherence while propagating through the lattice. The subsequent saturation to a plateau can be understood in terms of quantum fluctuation in the ground state, which generally suppress long-range order in one-dimensional

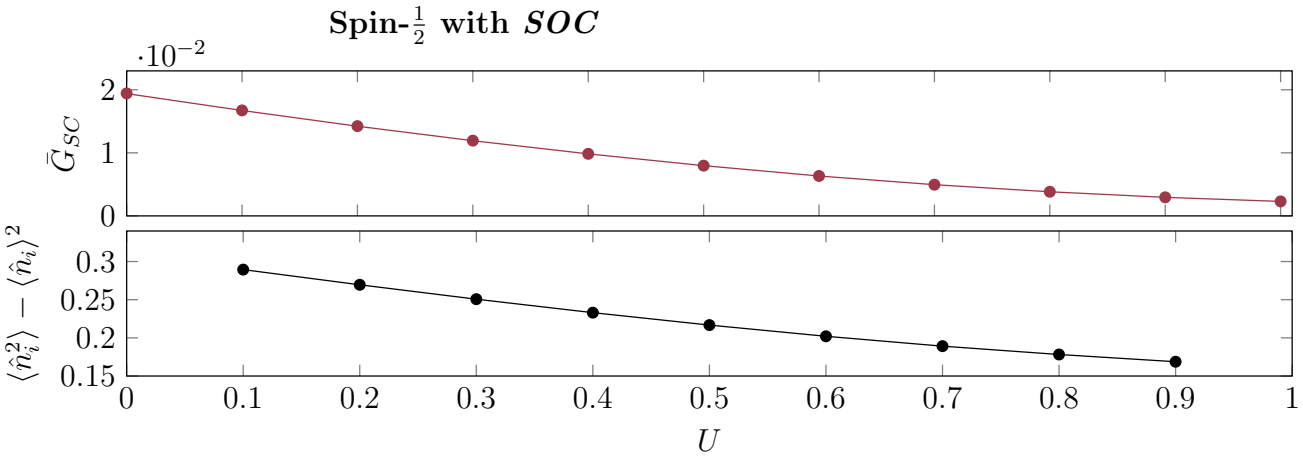

Figure 5.6: Upper panel presents the pair-pair correlator $\bar{G}$ average value over the non-decaying region as function of parameter U. Lower panel presents the density fluctuations $\langle \hat{n}_i^2 \rangle - \langle \hat{n}_i \rangle^2$ as function of parameter U. Characterized using the *MPO* representation **(dots)** in comparison with the standard *MPS* formalism **(solid lines)**.

systems. Nevertheless, the presence of a finite asymptotic value of the pair-pair correlator signals the existence of superconducting pairing terms in the ground state. The essence of this physics is completely captured by the *MPO* calculations.

As U increases, the energetic cost of forming local Cooper pairs grows due to the on-site interaction, which penalizes double occupancy at a lattice site i. This behavior is reflected in Fig. (5.6). At sufficiently large U, the formation of local pairs is completely suppressed, and the superconducting order vanishes, as shown in Fig. (5.5) for $U > 1$, meaning that the *MPO* calculations allow us to characterize states ranging from the superfluid regime to the insulating regime faithfully.

The behavior of the density fluctuations $\langle \hat{n}_i^2 \rangle - \langle \hat{n}_i \rangle^2$, as a function of U shows that particle number fluctuations across the lattice are progressively suppressed as the interaction strength increases, signaling the transition from a superconducting regime, where mobile Cooper pairs allow for larger fluctuations, to a more localized regime characterized by reduced charge dynamics. This reduction of density fluctuations thus provides additional evidence for the loss of superconducting order at large U.

The magnetization $\langle \hat{S}_z \rangle$ is found to vanish across the explored U values, indicating the ground state remains spin-balanced between the $m = +1$ and $m = -1$ magnetic projections without any magnetic ordering, consistent with a spin-singlet superconducting phase.

Finally, Fig. (5.4) shows that the normalized pairing correlator $\langle \hat{c}_{i,\uparrow} \hat{c}_{i+\delta,\downarrow} \rangle$ decays to zero at large distances while displaying oscillations, indicating spatial modulation of the pairing amplitude or finite-momentum pairing tendencies.

Chapter 6

Conclusions and perspectives

This work achieved the numerical implementation of the Matrix Product Operator *MPO* formalism in a *C++* library, extending the capabilities of the previously developed *MPS* framework. The library represents a lasting tool for the Solid State theoretical physics group, enabling the study of strongly correlated system with greater efficiency and flexibility for performing high-complexity calculations such as correlation functions and handling non-trivial Hamiltonians. As a first application, we applied this framework to multiple systems, successfully benchmarking the *MPO* approach against standard *MPS* calculations. This chapter begins with the conclusions of the results obtained during the development of this work, highlighting key points and relevant aspects that might motivate further scientific production. Then we present the perspectives on future work based on the obtained results to improve numerical aspects of the simulations and introduce novel features to the formalisms.

6.1 Summary and conclusions

In Chapter 2 we started by introducing the spinless Bose-Hubbard model, which was later expressed in its second quantization form, were we detailed relevant physical properties of the system such as the spin-changing and preserving collisions and described the phases of the system in the parameter space . We followed by introducing the effective spin-orbit coupling *(SOC)* and the Hamiltonian in terms of the new helical basis, delving into the effects of the introduced magnetic field in the energy spectrum, causing a splitting of the band structure for each magnetic projection when the *SOC* strength parameter α is varied.

Chapter 3 is the main core of the present work, here we presented the Matrix Product States *(MPS)* and operators *(MPO)* theoretical formalism, specifying the process for calculating expectation values of local operators such as the energy or number of particles, neighboring sites operators such as the hopping and long range correlations. We developed a generalization of the four-index transfer matrix used in the *MPS* formalism to the six-index version required for the *MPO* case, with a considerable increment in complexity. We also proposed an efficient way of representing operators in the *MPO* form in compatible way with the previously implemented *MPS* formalism

while solving some open problems such as the boundary contraction optimization and exploring new contraction protocols (forward, backward and decentralized order) in order to test computational efficiency in the algorithm. This lead us to our first two conclusions: firstly, that it is possible to express non-local operators such as the Hamiltonian or long-range correlations in a local-invariant form, making the algorithm site independent, which opens a new window of opportunities for parallelization and further optimizations. Moreover, that the local-invariant form reduces the local basis elements required to express any operator involving two sites such as the Hopping, from m^2 to m, which represents a reduction in the squared matrix representation from m^2 to $w * m$, where m is the dimension of the local basis and w is the virtual dimension of the *MPO*, which in general follows $w < m$. This reduces the numerical complexity of performing calculations for larger m such as in the case of the superfluid regime, where $m = 16$ when considering up to two particles per site.

Chapter 4 focused mainly on the numerical implementation of the previously developed formalism, giving insights on the detailed algorithms followed as a pedagogical showcase of the intricate and complex form underlying the field of tensor networks.

Finally, in chapter 5 we tested the developed **C++** library against calculations performed with the standard *MPS* approach across a variety of models with different characteristics, covering both a fermionic system and a system described by an angular momentum Hamiltonian as a way of benchmarking the results obtained by means of the newly introduced *MPO* formalism. Specifically, we characterized the ground state of the bilinear-biquadratic Heisenberg model within the dimer-Mott phase, using a local basis of three states which, due to the numerical requirements of the method, was extended to four states by including the vacuum. Simulations were performed on lattices of up to $L = 30$ sites. In addition, we studied a spin-$\frac{1}{2}$ fermionic system with a local basis of four states in presence of an effective spin-orbit coupling *(SOC)*. In this case, the *MPO* implementation significantly simplified the manipulation of fermionic operators. By varying the interaction from weak to strong, we captured the transition from the superfluid to the Mott phase, thus testing the robustness of the *MPO*-measure method.

The contrast of the obtained results in measurements of observables such as the energy, number of particles, magnetization, parity and various correlations, allowed to confirm the validity of the numerical implementation. After assuring the fidelity of the results, we performed characterization of the superfluid regime in presence of the effective orbit coupling, studying the behavior of some long-range correlations and calculating relevant local and global parameters such as the pair-pair

correlator and the magnetic projections population profile.

The behavior of the correlations allowed us to make conclusions about the physical properties of each characterized ground state.

It is important to remark the advantage of the *MPO* representation when dealing with a rapidly increasing dimension of the local Hilbert space with the size of the system and the internal degrees of freedom. The simplification in representation, makes not only easier to obtain the theoretical expression for non-trivial hamiltonians and operators, but also reduces the computational resources necessary to perform complex calculations.

The present work is expected to be the starting point for future students to carry on the research on the field of tensor networks in the Solid State theoretical physics group, being this and the work of my partner S. Gómez the first ones in this field in the group. In the next section we will present an outline of future perspectives that might be taken into consideration for giving continuation to the work started in this thesis.

6.2 Perspectives

Due to time constraints, the developed numerical methods were tested only on the spin-1 Bose–Hubbard model without including spin–orbit coupling, as reported in the thesis project of my research colleague J. Gomez. As a next step, we aim to extend the implementation to systems with spin–orbit coupling in order to characterize its effects.

One of the following directions is to implement the newly introduced *MPO* formalism with other the methods to find the ground-state of a system such as the imaginary time evolution block decimation (*iTEBD*) or the variational method, exploiting the local-invariant form to parallelize this processes, reducing the computation time required to find the ground state of complex systems with increasing number of lattice sites.

Another possibility is to introduce periodic boundary conditions to the system by using Vidal's proposed infinite *MPS(IMPS)* [45] in order reduce finite size effects on the lattice.

The initial implementation of the one-dimensional *MPS-MPO* case is the building block for constructing tensor network simulations in higher dimensions or with arbitrary tensor geometries, such as *PEPS* [47].

Additionally, further improvements on the numerical algorithms might be done by following

optimized tensor contraction protocols found in the literature, along with a sparse matrix optimized treatment.

Appendix A

Spin 1 Calculations

In this appendix, we demonstrate the procedure to convert the interaction potential from projector operators to spin operators, considering the addition of angular momenta in the spin-one case . Then we use the spin-including interaction potential to express the whole Hamiltonian in second quantization.

A.1 Interaction Potential

For the purpose of modeling the interaction with the inclusion of the spin degree of freedom, we consider a system of two interacting particles with its corresponding spin operators $\hat{S}_1$ and $\hat{S}_2$ acting on their different Hilbert subspaces of the system's total Hilbert space, we can define the total spin operator that characterizes the system as $\hat{\boldsymbol{F}} = \hat{\boldsymbol{S}}_1 + \hat{\boldsymbol{S}}_2$. With this new operator we can describe the spin-one system in terms of two sets of mutually compatible observables with their respective set of eigenstates, as follows: where $\hat{\boldsymbol{S}}_i^2$ are the squares of the individual spin operators,

Basis	**Operators**	**Eigenstates**	
		Long	Short
Uncoupled	$\hat{\boldsymbol{S}}_1^2, \hat{\boldsymbol{S}}_2^2, \hat{S}_1^z, \hat{S}_2^z$	$\lvert s_1, s_2, \sigma_1, \sigma_2\rangle$	$\lvert \sigma_1, \sigma_2\rangle$
Coupled	$\hat{\boldsymbol{S}}_1^2, \hat{\boldsymbol{S}}_2^2, \hat{\boldsymbol{F}}^2, \hat{F}^z$	$\lvert s_1, s_2, F, M\rangle$	$\lvert F, M\rangle$

$\hat{\boldsymbol{F}}^2$ is the square of the total spin operator for the coupled system, and $\hat{F}^z$ is the total magnetic projection on the z-axis. We have $|s_1 - s_2| \leq F \leq s_1 + s_2$ and $-F \leq M \leq F$.

The relation between the coupled and uncoupled basis is given by the unitary transformation that connects both bases:

$$|s_1, s_2, F, M\rangle = \sum_{\sigma_1} \sum_{\sigma_2} |s_1, s_2, \sigma_1, \sigma_2\rangle \underbrace{\langle s_1, s_2, \sigma_1, \sigma_2 | s_1, s_2, F, M\rangle}_{\textbf{Glebsch-Gordan coefficients}} \tag{A.1}$$

Since the total spin F remains unaltered when two particles interact, the interaction Hamiltonian can be expressed in terms of the projector $\hat{P}_F = |F, M\rangle\langle F, M|$ for the different spin channels

as:

$$\hat{V}_{\text{int}} = \sum_F g_F \hat{P}_F \delta(x - x'), \quad \text{with} \quad g_F = \frac{4\pi\hbar^2 a_F}{m}. \tag{A.2}$$

The scattering processes are independent in each channel. Due to the anti-symmetrical nature of the $F = 1$ channel it will be discarded, thus the available channels for our bosonic case are $F = \{0, 2\}$. Under this consideration, the interaction yields in:

$$\hat{V}_{\text{int}} = \left(g_0 \hat{P}_0 + g_2 \hat{P}_2\right) \delta(x - x'), \tag{A.3}$$

We can express the effective potential in terms of the spin operators, using the total spin relation we have:

$$\hat{\boldsymbol{F}}^2 = \left(\hat{\boldsymbol{S}}_1 + \hat{\boldsymbol{S}}_2\right)^2 = \hat{\boldsymbol{S}}_1^2 + 2\hat{\boldsymbol{S}}_1 \cdot \hat{\boldsymbol{S}}_2 + \hat{\boldsymbol{S}}_2^2,$$

$$\hat{\boldsymbol{S}}_1 \cdot \hat{\boldsymbol{S}}_2 = \frac{1}{2}\left(\hat{\boldsymbol{F}}^2 - \hat{\boldsymbol{S}}_1^2 - \hat{\boldsymbol{S}}_2^2\right). \tag{A.4}$$

Operators $\hat{P}_0$ and $\hat{P}_2$ are linearly independent and form a complete set, thus we can implement them as a basis for expressing any of the linear operators of the space, expressing the last operator as a superposition of the elements on the basis:

$$\hat{\boldsymbol{S}}_1 \cdot \hat{\boldsymbol{S}}_2 = \lambda_0 \hat{P}_0 + \lambda_2 \hat{P}_2, \tag{A.5}$$

Applying $\hat{\boldsymbol{S}}_1 \cdot \hat{\boldsymbol{S}}_2$ to the elements of the coupled basis according to the identity in Eq. (A.4) and expressing in terms of their eigenvalues (neglecting $\hbar$), we obtain:

$$\hat{\boldsymbol{S}}_1 \cdot \hat{\boldsymbol{S}}_2 |F, M\rangle = \frac{1}{2}\left(F(F+1) - s_1(s_1+1) - s_2(s_2+1)\right)|F, M\rangle, \tag{A.6}$$

since both particles have spin one $s_1 = s_2 = 1$:

$$\hat{\boldsymbol{S}}_1 \cdot \hat{\boldsymbol{S}}_2 |F, M\rangle = \frac{1}{2}\left(F(F+1) - 4\right)|F, M\rangle, \tag{A.7}$$

thus

$$\hat{\boldsymbol{S}}_1 \cdot \hat{\boldsymbol{S}}_2 \, \hat{P}_F = \frac{1}{2}\left(F(F+1) - 4\right)\hat{P}_F = \lambda_F \hat{P}_F, \tag{A.8}$$

it is straight forward to see that $\lambda_0 = -2$ and $\lambda_2 = 1$.

Considering the completeness relation for the basis elements we can express $\hat{I} = \hat{P}_0 + \hat{P}_2$, giving us

the following system of equations:

$$\hat{I} = \hat{P}_0 + \hat{P}_2, \quad \hat{\boldsymbol{S}}_1 \cdot \hat{\boldsymbol{S}}_2 = -2\hat{P}_0 + \hat{P}_2, \tag{A.9}$$

then, solving the system of equations for the projectors, we get:

$$\hat{P}_0 = \frac{\hat{I} - \hat{\boldsymbol{S}}_1 \cdot \hat{\boldsymbol{S}}_2}{3}, \quad \hat{P}_2 = \frac{2\hat{I} + \hat{\boldsymbol{S}}_1 \cdot \hat{\boldsymbol{S}}_2}{3}, \tag{A.10}$$

finally allowing us to express Eq. (A.3) as:

$$\hat{V}_{\text{int}} = \left(c_0 + c_2 \hat{\boldsymbol{S}}_1 \cdot \hat{\boldsymbol{S}}_2\right) \delta(x - x') \quad \text{with:} \quad c_0 = \frac{g_0 + 2g_2}{3} \quad \text{and} \quad c_2 = \frac{g_2 - g_0}{3}. \tag{A.11}$$

A.2 Second Quantization

We start by defining the new fields operators $\hat{\Psi}_\alpha(x)$ including the spin 1 degree of freedom

$$\hat{\Psi}_\alpha(x) = \sum_i W_i(x) \hat{b}_{i,\alpha}, \tag{A.12}$$

these satisfy the same commutation relations as the previous spinless ones, with the addition of the spin factor:

$$\left[\hat{\Psi}^\dagger_\alpha(x), \hat{\Psi}^\dagger_\beta(x')\right] = \left[\hat{\Psi}_\alpha(x), \hat{\Psi}_\beta(x')\right] = 0, \quad \left[\hat{\Psi}_\alpha(x), \hat{\Psi}^\dagger_\beta(x')\right] = \delta_{\alpha\beta}\delta(x - x').$$

In order to derive the model we start from the Hamiltonian for one particle, which reads,

$$\hat{H} = \frac{\hat{p}^2}{2m} + \hat{V}_{\text{ext}} + \hat{V}_{\text{int}}, \tag{A.13}$$

in the second quantization formalism with the addition of spin-1 degree of freedom the hopping term would be

$$\begin{aligned}
\hat{H}_J &= \sum_{\alpha,\beta} \int \mathrm{d}x\ \hat{\Psi}^\dagger_\alpha(x)\langle\alpha| \left(-\frac{\hbar^2\nabla^2}{2m} + V_{\text{ext}}(x)\right) |\beta\rangle \hat{\Psi}_\beta(x), \\
&= \sum_{i,j}\sum_{\alpha,\beta} \int \mathrm{d}x\ W_i^*(x) \left(-\frac{\hbar^2\nabla^2}{2m} + V_{\text{ext}}(x)\right) W_j(x) \underbrace{\langle\alpha|\beta\rangle}_{\delta_{\alpha,\beta}} \hat{b}^\dagger_{i,\alpha}\hat{b}_{j,\beta}, \\
&= -J\sum_{i,\sigma}\left(\hat{b}^\dagger_{i+1,\sigma}\hat{b}_{i,\sigma} + \hat{b}^\dagger_{i,\sigma}\hat{b}_{i+1,\sigma}\right), \qquad \text{(A.14)}
\end{aligned}$$

where we have considered the tight-binding approximation.

For the interaction potential defined in Eq. (A.11), we get,

$$\begin{aligned}
\hat{V}_{\text{int}} &= \frac{1}{2}\sum_{\alpha,\gamma,\beta,\sigma} \int \mathrm{d}x\ \mathrm{d}x' \hat{\Psi}^\dagger_\alpha(x)\hat{\Psi}^\dagger_\gamma(x')\langle\alpha,\gamma|\hat{V}_{\text{int}}|\beta,\sigma\rangle\hat{\Psi}_\beta(x')\hat{\Psi}_\sigma(x), \\
&= \sum_{\alpha,\beta,\gamma,\sigma} \int \mathrm{d}x \left(\frac{c_0}{2}\hat{\Psi}^\dagger_\alpha(x)\hat{\Psi}^\dagger_\beta(x)\hat{\Psi}_\beta(x)\hat{\Psi}_\alpha(x) + \frac{c_2}{2}\hat{\Psi}^\dagger_\alpha(x)\hat{\Psi}^\dagger_\gamma(x)[\hat{\boldsymbol{S}}]_{\alpha\beta}\cdot[\hat{\boldsymbol{S}}]_{\gamma\sigma}\hat{\Psi}_\gamma(x)\hat{\Psi}_\sigma(x)\right), \\
&= \frac{U_0}{2}\sum_{i,\alpha,\beta}\hat{b}^\dagger_{i,\alpha}\hat{b}^\dagger_{i,\beta}\hat{b}_{i,\beta}\hat{b}_{i,\alpha} + \frac{U_2}{2}\sum_{i,\alpha,\beta,\gamma,\sigma,\nu}\hat{b}^\dagger_{i,\alpha}\hat{b}^\dagger_{i,\gamma}[\hat{S}^\nu]_{\alpha\beta}[\hat{S}^\nu]_{\gamma\sigma}\hat{b}_{i,\sigma}\hat{b}_{i,\beta}, \\
&= \sum_{i,\alpha,\beta}\hat{b}^\dagger_{i,\alpha}(\hat{b}_{i,\alpha}\hat{b}^\dagger_{i,\beta} - \delta_{\alpha\beta})\hat{b}_{i,\beta} + \frac{U_2}{2}\sum_{i,\nu}\left\{\left(\hat{F}^\nu_i\right)^2 - \sum_{\alpha,\beta,\sigma}\hat{b}^\dagger_{i,\alpha}[\hat{S}^\nu]_{\alpha\beta}[\hat{S}^\nu]_{\beta\sigma}\hat{b}_{i,\sigma}\right\}, \\
&= \frac{U_0}{2}\sum_{i,\sigma}\hat{n}_{i,\sigma}\left(\hat{n}_{i,\sigma} - 1\right) + \frac{U_2}{2}\sum_i\left(\hat{\boldsymbol{F}}^2_i - 2\sum_\sigma\hat{n}_{i,\sigma}\right), \qquad \text{(A.15)}
\end{aligned}$$

where

$$\begin{aligned}
J &= \int dx\ W_i^*(x)\left(-\frac{\hbar^2\nabla^2}{2m} + V_{\text{lat}}(x)\right)W_j(x), \\
U_0 &= c_0\int dx\ |W(x)|^4 = \frac{g_0+2g_2}{3}\int dx\ |W(x)|^4, \\
U_2 &= c_2\int dx\ |W(x)|^4 = \frac{g_2-g_0}{3}\int dx\ |W(x)|^4, \\
\hat{\boldsymbol{F}}_i &= \left(\hat{F}^x_i, \hat{F}^y_i, \hat{F}^z_i\right), \quad \hat{F}^\nu_i = \sum_{\sigma,\sigma'}\hat{b}^\dagger_{i,\sigma}[\hat{S}^\nu]_{\sigma\sigma'}\hat{b}_{i,\sigma'}.
\end{aligned}$$

So finally, the Bose-Hubbard Hamiltonian for spin-1 particles, in second quantization and in the grand canonical ensemble, is given by,

$$\hat{H} = -J\sum_{i,\sigma}\left(\hat{b}^{\dagger}_{i+1,\sigma}\hat{b}_{i,\sigma} + \text{h.c.}\right) + \frac{U_0}{2}\sum_{i,\sigma}\hat{n}_{i,\sigma}\left(\hat{n}_{i,\sigma}-1\right) + \frac{U_2}{2}\sum_{i}\hat{\boldsymbol{F}}_i^2 - (\mu+U_2)\sum_{i,\sigma}\hat{n}_{i,\sigma}. \quad \text{(A.16)}$$

A.3 Explicit form of the interaction terms

We take the interaction term in Eq (A.3) and represent in second quantization without re-writing the projection operators $\hat{P}_0$ and $\hat{P}_2$ in terms of the spin operators, as follows:

$$\begin{aligned}
\hat{V}_{\text{int}} &= \frac{1}{2}\sum_{\alpha,\gamma,\beta,\sigma}\int \mathrm{d}x\ \mathrm{d}x'\ \hat{\Psi}^{\dagger}_{\alpha}(x)\hat{\Psi}^{\dagger}_{\gamma}(x')\langle\alpha,\gamma|\hat{V}_{\text{int}}|\beta,\sigma\rangle\hat{\Psi}_{\beta}(x')\hat{\Psi}_{\sigma}(x)\\
&= \frac{1}{2}\sum_{\alpha,\gamma,\beta,\sigma}\int \mathrm{d}x\ \mathrm{d}x'\ \hat{\Psi}^{\dagger}_{\alpha}(x)\hat{\Psi}^{\dagger}_{\gamma}(x')\ \langle\alpha,\gamma|\left[\left(g_0\hat{P}_0 + g_2\hat{P}_2\right)\delta(x-x')\right]|\beta,\sigma\rangle\ \hat{\Psi}_{\beta}(x')\hat{\Psi}_{\sigma}(x)\\
&= \frac{1}{2}\sum_{\alpha,\gamma,\beta,\sigma}\int \mathrm{d}x\ \hat{\Psi}^{\dagger}_{\alpha}(x)\hat{\Psi}^{\dagger}_{\gamma}(x)\ \langle\alpha,\gamma|\left[\Big(\underbrace{g_0\hat{P}_0}_{\textbf{(a)}} + \underbrace{g_2\hat{P}_2}_{\textbf{(b)}}\Big)\right]|\beta,\sigma\rangle\ \hat{\Psi}_{\beta}(x)\hat{\Psi}_{\sigma}(x)
\end{aligned} \quad \text{(A.17)}$$

First, we express the term of the $\hat{P}_0$ projector in the coupled basis, yielding in:

$$\textbf{(a)} = \frac{g_0}{2}\sum_{\alpha,\gamma,\beta,\sigma}\int \mathrm{d}x\ \hat{\Psi}^{\dagger}_{\alpha}(x)\hat{\Psi}^{\dagger}_{\gamma}(x)\ \langle\alpha,\gamma|\underbrace{\left(|0,0\rangle\ \langle 0,0|_c\right)}_{\hat{P}_0}|\beta,\sigma\rangle\ \hat{\Psi}_{\beta}(x)\hat{\Psi}_{\sigma}(x), \quad \text{(A.18)}$$

where $|0,0\rangle_c = \frac{1}{\sqrt{3}}\left(|1,-1\rangle - |0,0\rangle + |-1,1\rangle\right)$ in terms of the decoupled basis. Inserting this in equation Eq. (A.18) and using the orthogonality of the basis elements while considering the representation of the field operators given in Eq. (A.12) results in:

$$\begin{aligned}
\textbf{(a)} = \frac{g_0}{6}U\ \Big(&\hat{b}^{\dagger}_1\hat{b}^{\dagger}_{-1}\hat{b}_1\hat{b}_{-1} - \hat{b}^{\dagger}_1\hat{b}^{\dagger}_{-1}\hat{b}_0\hat{b}_0 + \hat{b}^{\dagger}_1\hat{b}^{\dagger}_{-1}\hat{b}_{-1}\hat{b}_1 - \hat{b}^{\dagger}_0\hat{b}^{\dagger}_0\hat{b}_1\hat{b}_{-1} + \hat{b}^{\dagger}_0\hat{b}^{\dagger}_0\hat{b}_0\hat{b}_0 - \hat{b}^{\dagger}_0\hat{b}^{\dagger}_0\hat{b}_{-1}\hat{b}_1\\
&+ \hat{b}^{\dagger}_{-1}\hat{b}^{\dagger}_1\hat{b}_1\hat{b}_{-1} - \hat{b}^{\dagger}_{-1}\hat{b}^{\dagger}_1\hat{b}_0\hat{b}_0 + \hat{b}^{\dagger}_{-1}\hat{b}^{\dagger}_1\hat{b}_{-1}\hat{b}_1\Big),
\end{aligned}$$

with $U = \int \mathrm{d}x|W(x)|^4$. Following the same procedure for $\hat{P}_2 = \sum_m |2,m\rangle_c$ with $m \in [-2,2]$ yields in:

$$\begin{aligned}\textbf{(b)} = \frac{g_2}{2}U \Big(&\hat{b}_1^\dagger\hat{b}_1^\dagger\hat{b}_1\hat{b}_1 + \frac{1}{2}\hat{b}_1^\dagger\hat{b}_0^\dagger\hat{b}_1\hat{b}_0 + \frac{1}{2}\hat{b}_1^\dagger\hat{b}_0^\dagger\hat{b}_0\hat{b}_1 + \frac{1}{2}\hat{b}_0^\dagger\hat{b}_1^\dagger\hat{b}_1\hat{b}_0 + \frac{1}{2}\hat{b}_0^\dagger\hat{b}_1^\dagger\hat{b}_0\hat{b}_1 + \frac{1}{6}\hat{b}_1^\dagger\hat{b}_{-1}^\dagger\hat{b}_1\hat{b}_{-1} + \frac{1}{3}\hat{b}_1^\dagger\hat{b}_{-1}^\dagger\hat{b}_0\hat{b}_0 \\ &+ \frac{1}{6}\hat{b}_1^\dagger\hat{b}_{-1}^\dagger\hat{b}_{-1}\hat{b}_1 + \frac{1}{3}\hat{b}_0^\dagger\hat{b}_0^\dagger\hat{b}_1\hat{b}_{-1} + \frac{2}{3}\hat{b}_0^\dagger\hat{b}_0^\dagger\hat{b}_0\hat{b}_0 + \frac{1}{3}\hat{b}_0^\dagger\hat{b}_0^\dagger\hat{b}_{-1}\hat{b}_1 + \frac{1}{6}\hat{b}_{-1}^\dagger\hat{b}_1^\dagger\hat{b}_1\hat{b}_{-1} + \frac{1}{3}\hat{b}_{-1}^\dagger\hat{b}_1^\dagger\hat{b}_0\hat{b}_0 \\ &+ \frac{1}{6}\hat{b}_{-1}^\dagger\hat{b}_1^\dagger\hat{b}_{-1}\hat{b}_1 + \frac{1}{2}\hat{b}_{-1}^\dagger\hat{b}_0^\dagger\hat{b}_{-1}\hat{b}_0 + \frac{1}{2}\hat{b}_{-1}^\dagger\hat{b}_0^\dagger\hat{b}_0\hat{b}_{-1} + \frac{1}{2}\hat{b}_0^\dagger\hat{b}_{-1}^\dagger\hat{b}_{-1}\hat{b}_0 + \frac{1}{2}\hat{b}_0^\dagger\hat{b}_{-1}^\dagger\hat{b}_0\hat{b}_{-1} + \hat{b}_{-1}^\dagger\hat{b}_{-1}^\dagger\hat{b}_{-1}\hat{b}_{-1}\Big).\end{aligned}$$

After adding **(a)** with **(b)** and grouping terms, Eq. (A.17) is expressed in second quantization formalism as:

$$\begin{aligned}\hat{V}_{int} =&U\left(\frac{g_0+2g_2}{6}\right)\hat{b}_0^\dagger\hat{b}_0^\dagger\hat{b}_0\hat{b}_0 + U\left(\frac{2g_0+g_2}{3}\right)\hat{b}_1^\dagger\hat{b}_{-1}^\dagger\hat{b}_1\hat{b}_{-1} + \left(\frac{g_2-g_0}{3}\right)\left(\hat{b}_1^\dagger\hat{b}_{-1}^\dagger\hat{b}_0\hat{b}_0 + \hat{b}_0^\dagger\hat{b}_0^\dagger\hat{b}_{-1}\hat{b}_1\right) \\ &+ \frac{g_2}{2}\left(\hat{b}_1^\dagger\hat{b}_1^\dagger\hat{b}_1\hat{b}_1 + 2\hat{b}_1^\dagger\hat{b}_0^\dagger\hat{b}_1\hat{b}_0 + 2\hat{b}_{-1}^\dagger\hat{b}_0^\dagger\hat{b}_{-1}\hat{b}_0 + \hat{b}_{-1}^\dagger\hat{b}_{-1}^\dagger\hat{b}_{-1}\hat{b}_{-1}\right),\end{aligned}$$

where the spin preserving and changing interaction processes described in Fig. (2.2) are explicitly readable from this form of the interaction Hamiltonian. Note that expressing in terms of the helical states is as simple as relabeling $\{-1,0,1\} \to \{\circlearrowleft,|,\circlearrowright\}$ due to the commutation properties of the bosonic operators and the unitarity of the transformation.

Appendix B

Spin-Orbit Coupling

In this appendix, we detail the effects the *SOC* has in our model. First we proceed expressing the hopping Hamiltonian in $\hat{S}^y$ basis, introducing the new helical states. We then perform a Fourier transform into momentum space in order to elucidate the behaviour of the dispersion relation.

B.1 Hopping term

It was shown that the hopping term can be written as:

$$\hat{H}_0 = -J \sum_{i,\sigma} \left(\hat{b}^\dagger_{i,\sigma} \mathbb{R}^{\sigma,\sigma'}_{i,i+1} \hat{b}_{i+1,\sigma} + \text{h.c.} \right), \tag{B.1}$$

with $\mathbb{R}^{\sigma,\sigma'}_{i,i+1}$ given by Eq. (2.18).

Change from $\hat{S}_z$ to $\hat{S}_y$ basis.

We can construct the basis transformation matrix $\mathbb{U}$ with the eigenvectors of the hopping matrix due to its proportionality to $\hat{S}^y$ operator, it is easy to check that under this consideration we have

$$\mathbb{U} = \begin{bmatrix} -\frac{1}{2} & -\frac{i\sqrt{2}}{2} & \frac{1}{2} \\ \frac{1}{\sqrt{2}} & 0 & \frac{1}{\sqrt{2}} \\ -\frac{1}{\sqrt{2}} & \frac{i\sqrt{2}}{2} & \frac{1}{2} \end{bmatrix}, \quad \text{and} \quad \mathbb{U}^\dagger = \begin{bmatrix} -\frac{1}{2} & \frac{1}{\sqrt{2}} & -\frac{1}{2} \\ \frac{i\sqrt{2}}{2} & 0 & -\frac{i\sqrt{2}}{2} \\ \frac{1}{2} & \frac{1}{\sqrt{2}} & \frac{1}{2} \end{bmatrix}, \tag{B.2}$$

which performs the change from the $\hat{S}^z$ basis to the $\hat{S}^y$ basis. Applying the transformation to Eq. (B.1) :

$$\begin{aligned}
\hat{H}_0 &= -J\sum_{i,\sigma}\left(\hat{b}^\dagger_{i,\sigma}\left(\mathbb{U}^\dagger\mathbb{U}\right)\mathbb{R}^{\sigma,\sigma'}_{i,i+1}\left(\mathbb{U}^\dagger\mathbb{U}\right)\hat{b}_{i+1,\sigma}+\text{h.c.}\right)\\
&= -J\sum_{i}\left[\begin{pmatrix}\hat{b}^\dagger_{i,\circlearrowleft}\\ \hat{b}^\dagger_{i,|}\\ \hat{b}^\dagger_{i,\circlearrowright}\end{pmatrix}^T\begin{pmatrix}\cos(\alpha)-\sqrt{2}\sin(\alpha) & 0 & 0\\ 0 & \cos(\alpha) & 0\\ 0 & 0 & \cos(\alpha)+\sqrt{2}\sin(\alpha)\end{pmatrix}\begin{pmatrix}\hat{b}_{i+1,\circlearrowleft}\\ \hat{b}_{i+1,|}\\ \hat{b}_{i+1,\circlearrowright}\end{pmatrix}+\text{h.c.}\right]\\
&= -J\sum_{i,\bar{\sigma}}\left(\hat{b}^\dagger_{i,\bar{\sigma}}\mathbb{D}^{\bar{\sigma}}_{i,i+1}\hat{b}_{i+1,\bar{\sigma}}+\text{h.c.}\right),
\end{aligned}$$

where we have defined a new set of bosonic operators called *helical states* in terms of the magnetic operators as:

$$\hat{b}_{l,\circlearrowleft}=\frac{-\hat{b}_{l,1}+i\sqrt{2}\hat{b}_{l,0}+\hat{b}_{l,-1}}{2},\quad \hat{b}_{l,|}=\frac{\hat{b}_{l,1}+\hat{b}_{l,-1}}{\sqrt{2}},\quad \text{and}\quad \hat{b}_{l,\circlearrowright}=\frac{-\hat{b}_{l,1}-i\sqrt{2}\hat{b}_{l,0}+\hat{b}_{l,-1}}{2},$$

with the corresponding helical projections ($\bar{\sigma}$), with value 1 for the left state ($\circlearrowleft$), 0 for the linear state ($|$) and -1 for the right state ($\circlearrowright$).

Fourier transform

The term in Eq. (2.20) can be expressed as:

$$\begin{aligned}
\hat{H}_0 &= -J\sum_{l}\left(\cos(\alpha)-i\sqrt{2}\sin(\alpha)\right)\hat{b}^\dagger_{l,\circlearrowleft}\hat{b}_{l+1,\circlearrowleft}+\cos(\alpha)\hat{b}^\dagger_{l,|}\hat{b}_{l+1,|}+\left(\cos(\alpha)+i\sqrt{2}\sin(\alpha)\right)\hat{b}^\dagger_{l,\circlearrowright}\hat{b}_{l+1,\circlearrowright}\\
&\qquad\qquad\qquad\qquad\qquad\qquad\qquad\qquad\qquad\qquad\qquad\qquad\qquad\qquad\qquad\qquad+\text{h.c.}\\
&= -J\sum_{k,k'}\left(\cos(\alpha)-i\sqrt{2}\sin(\alpha)\right)\underbrace{\left(\frac{1}{L}\sum_{l}e^{il(k-k')}\right)}_{\delta_{k,k'}}e^{-ilk'}\hat{b}^\dagger_{k,\circlearrowleft}\hat{b}_{k',\circlearrowleft}+\cos(\alpha)\underbrace{\left(\frac{1}{L}\sum_{l}e^{il(k-k')}\right)}_{\delta_{k,k'}}\\
&\quad e^{-ilk'}\hat{b}^\dagger_{k,|}\hat{b}_{k',|}+\left(\cos(\alpha)+i\sqrt{2}\sin(\alpha)\right)\underbrace{\left(\frac{1}{L}\sum_{l}e^{il(k-k')}\right)}_{\delta_{k,k'}}e^{-ilk'}\hat{b}^\dagger_{k,\circlearrowright}\hat{b}_{k',\circlearrowright}+\text{h.c.}
\end{aligned}$$

$$
\begin{aligned}
&= -J \sum_k \cos(\alpha) \left(e^{ilk} + e^{-lk}\right) \hat{b}^\dagger_{k,\circlearrowleft} \hat{b}_{k,\circlearrowleft} + i\sqrt{2} \sin(\alpha) \left(e^{ilk} - e^{-lk}\right) \hat{b}^\dagger_{k,\circlearrowleft} \hat{b}_{k,\circlearrowleft} \\
&\quad + \cos(\alpha) \left(e^{ilk} + e^{-lk}\right) \hat{b}^\dagger_{k,|} \hat{b}_{k,|} \\
&\quad + \cos(\alpha) \left(e^{ilk} + e^{-lk}\right) \hat{b}^\dagger_{k,\circlearrowleft} \hat{b}_{k,\circlearrowleft} + i\sqrt{2} \sin(\alpha) \left(e^{ilk} - e^{-lk}\right) \hat{b}^\dagger_{k,\circlearrowleft} \hat{b}_{k,\circlearrowleft} \\
&= -2J \sum_k \Big(\cos(\alpha)\cos(k) - \sqrt{2}\sin(\alpha)\sin(k)\Big) \hat{b}^\dagger_{k,\circlearrowleft} \hat{b}_{k,\circlearrowleft} + \cos(\alpha)\cos(k) \hat{b}^\dagger_{k,|} \hat{b}_{k,|} \\
&\quad + \Big(\cos(\alpha)\cos(k) + \sqrt{2}\sin(\alpha)\sin(k)\Big) \hat{b}^\dagger_{k,\circlearrowleft} \hat{b}_{k,\circlearrowleft} \\
&= -2J \sum_{k,\bar{\sigma}} \hat{b}^\dagger_{k,\bar{\sigma}} \mathbb{D}^{\bar{\sigma}}_k \hat{b}_{k,\bar{\sigma}},
\end{aligned}
$$

with $\mathbb{D}^{\bar{\sigma}}_k$ given by Eq. (2.24)

Appendix C

Matrix Product States and operators calculations

In this appendix we present some explicit calculations associated to the orthogonalization process of the MPS, we also present the explicit procedure of the construction of the*MPO*, both in a general case and for the specific spin-one Bose-Hubbard model.

C.1 Orthogonalization process

We start with the *MPS* in Fig.(3.7), performing the Schmidt decomposition on the first matrix from the left side and grouping:

$$
\begin{aligned}
|\Psi\rangle &= \sum_{\substack{\alpha_2 \ldots \alpha_L \\ n_1 \ldots n_L}} \left(\sum_{\alpha_2'} U^{n_1}_{\alpha_1,\,\alpha_2'} D_{\alpha_2'} V^{*}_{\alpha_2',\,\alpha_2} \right) A^{n_2}_{\alpha_2,\,\alpha_3} \ldots A^{n_L}_{\alpha_L,\,\alpha_{L+1}} |n_1, \ldots, n_L\rangle \\
&= \sum_{\substack{\alpha_2' \ldots \alpha_L \\ n_1 \ldots n_L}} U^{n_1}_{\alpha_1,\,\alpha_2'} \left(\sum_{\alpha_2} D_{\alpha_2'} V^{*}_{\alpha_2',\,\alpha_2} A^{n_2}_{\alpha_2,\,\alpha_3} \right) \ldots A^{n_L}_{\alpha_L,\,\alpha_{L+1}} |n_1, \ldots, n_L\rangle \\
&= \sum_{\substack{\alpha_2' \ldots \alpha_L \\ n_1 \ldots n_L}} U^{n_1}_{\alpha_1,\,\alpha_2'} \bar{A}^{n_2}_{\alpha_2',\,\alpha_3} \ldots A^{n_L}_{\alpha_L,\,\alpha_{L+1}} |n_1, \ldots, n_L\rangle
\end{aligned}
$$

Then, applying the *SVD* over the $\bar{A}^{n_2}_{\alpha_2',\,\alpha_3}$ matrix and grouping with the next matrix.

$$
|\Psi\rangle = \sum_{\substack{\alpha_2', \alpha_3' \ldots \alpha_L \\ n_1 \ldots n_L}} U^{n_1}_{\alpha_1,\,\alpha_2'} U^{n_2}_{\alpha_2',\,\alpha_3'} \bar{A}^{n_2}_{\alpha_3',\,\alpha_4} \ldots A^{n_L}_{\alpha_L,\,\alpha_{L+1}} |n_1, \ldots, n_L\rangle \tag{C.1}
$$

Repeating the same procedure until reaching kth-site results in:

$$
|\Psi\rangle = \sum_{\substack{\alpha_2' \ldots \alpha_k' \\ \alpha_{k+1} \ldots \alpha_{L+1} \\ n_1 \ldots n_L}} U^{n_1}_{\alpha_1,\,\alpha_2'} \ldots U^{n_{k-1}}_{\alpha_{k-1}',\,\alpha_k'} \bar{A}^{n_k}_{\alpha_k',\,\alpha_{k+1}} \ldots A^{n_L}_{\alpha_L,\,\alpha_{L+1}} |n_1, \ldots, n_L\rangle \tag{C.2}
$$

We start the same procedure from the last matrix, applying *SVD* on the right-hand matrix:

$$
\begin{aligned}
|\Psi\rangle &= \sum_{\substack{\alpha_2 \ldots \alpha_L \\ n_1 \ldots n_L}} A^{n_1}_{\alpha_1,\,\alpha_2} \ldots A^{n_{L-1}}_{\alpha_{L-1},\,\alpha_L} \left(\sum_{\alpha'_L} U_{\alpha_L,\,\alpha'_L} D_{\alpha'_L} V^{n_L *}_{\alpha'_L,\,\alpha_{L+1}} \right) |n_1, \ldots, n_L\rangle \\
&= \sum_{\substack{\alpha_2 \ldots \alpha'_L \\ n_1 \ldots n_L}} A^{n_1}_{\alpha_1,\,\alpha_2} \ldots \left(\sum_{\alpha_L} A^{n_{L-1}}_{\alpha_{L-1},\,\alpha_L} U_{\alpha_L,\,\alpha'_L} D_{\alpha'_L} \right) V^{n_L *}_{\alpha'_L,\,\alpha_{L+1}} |n_1, \ldots, n_L\rangle \\
&= \sum_{\substack{\alpha_2 \ldots \alpha'_L \\ n_1 \ldots n_L}} A^{n_1}_{\alpha_1,\,\alpha_2} \ldots \bar{A}^{n_{L-1}}_{\alpha_{L-1},\,\alpha'_L} V^{n_L *}_{\alpha'_L,\,\alpha_{L+1}} |n_1, \ldots, n_L\rangle
\end{aligned}
$$

Repeating the procedure until reaching kth-site leads to the orthogonalized *MPS*, as follows:

$$
|\psi\rangle = \sum_{n_k, \alpha_k, \alpha_{k+1}} A^{n_k}_{\alpha_k, \alpha_{k+1}} |\alpha_k\rangle |n_k\rangle \left|\omega_{\alpha_{k+1}}\right\rangle , \tag{C.3}
$$

where

$$
|\alpha_k\rangle = \sum_{\alpha_1 \ldots \alpha_{k-1}} \prod_{s=1}^{k-1} U^{n_s}_{\alpha_s, \alpha_{s+1}} |n_s\rangle , \tag{C.4}
$$

and

$$
\left|\omega_{\alpha_{k+1}}\right\rangle = \sum_{\alpha_{k+2} \ldots \alpha_{L+1}} \prod_{s=k+1}^{L} V^{n_s *}_{\alpha_s, \alpha_{s+1}} |n_s\rangle . \tag{C.5}
$$

Due to the left and right unitary properties of matrices U and V, we have $\langle \alpha_k | \alpha'_k \rangle = \delta_{\alpha_k, \alpha'_k}$ and $\langle \omega_{\alpha_k} | \omega'_{\alpha_k} \rangle = \delta_{\omega_{\alpha_k}, \omega'_{\alpha_k}}$, therefore state $|\Psi\rangle$ is orthogonalized.

C.2 Numerical procedure for transfer matrix calculation

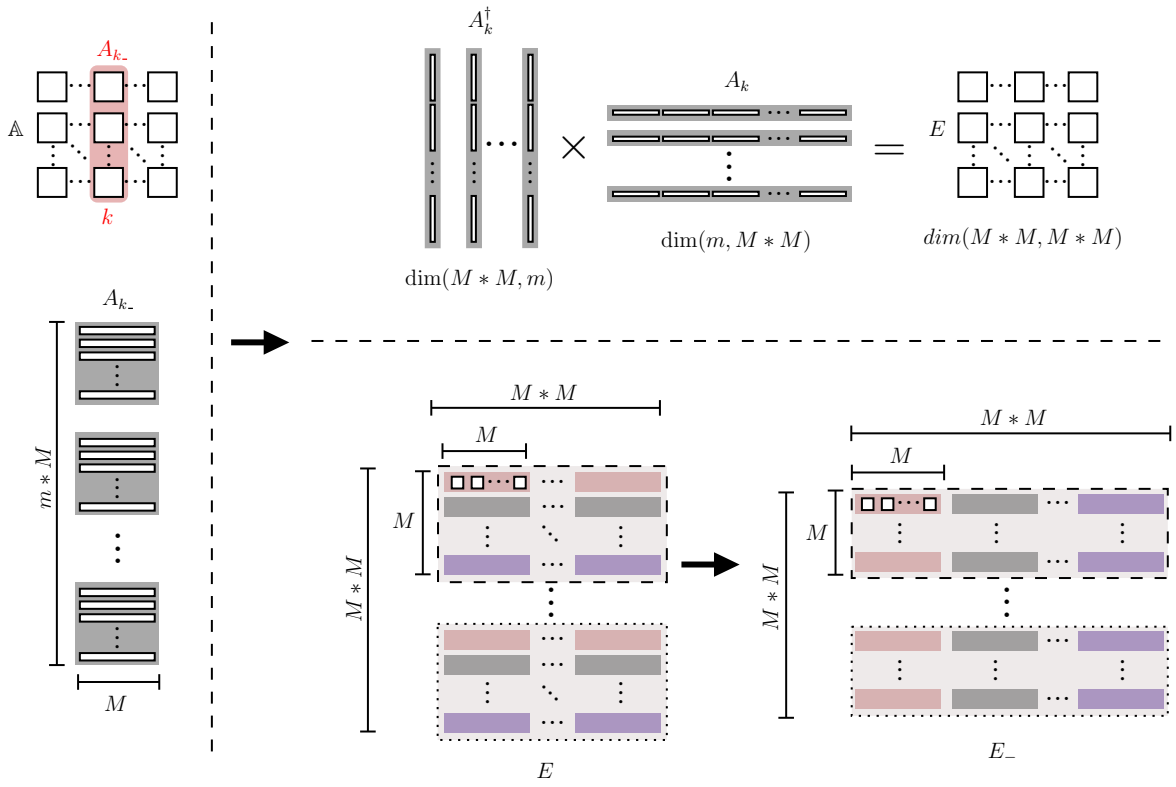

Figure C.1: Complete procedure used for transfer matrix calculation.

C.3 Bose-Hubbard Spin-1 matrix product operator derivation

We start from the Hamiltonian for the spin-1 Bose-Hubbard model in the helical states basis:

$$\hat{H} = -J\sum_{i,\bar{\sigma}}\left(\hat{b}^\dagger_{i,\bar{\sigma}}\mathbb{D}^{\bar{\sigma}}_{i,i+1}\hat{b}_{i+1,\bar{\sigma}} + \text{h.c.}\right) + U\left(\frac{g_0+2g_2}{6}\right)\hat{b}^\dagger_{i,|}\hat{b}^\dagger_{i,|}\hat{b}_{i,|}\hat{b}_{i,|} + U\left(\frac{2g_0+g_2}{3}\right)\hat{b}^\dagger_{i,\circlearrowleft}\hat{b}^\dagger_{i,\circlearrowleft}\hat{b}_{i,\circlearrowleft}\hat{b}_{i,\circlearrowleft}$$
$$+\left(\frac{g_0+2g_2}{3}\right)\left(\hat{b}^\dagger_{i,\circlearrowleft}\hat{b}^\dagger_{i,\circlearrowleft}\hat{b}_{i,|}\hat{b}_{i,|} + \hat{b}^\dagger_{i,|}\hat{b}^\dagger_{i,|}\hat{b}_{i,\circlearrowleft}\hat{b}_{i,\circlearrowleft}\right) \tag{C.6}$$
$$+\frac{g_2}{2}\left(\hat{b}^\dagger_{i,\circlearrowleft}\hat{b}^\dagger_{i,\circlearrowleft}\hat{b}_{i,\circlearrowleft}\hat{b}_{i,\circlearrowleft} + 2\hat{b}^\dagger_{i,\circlearrowleft}\hat{b}^\dagger_{i,|}\hat{b}_{i,\circlearrowleft}\hat{b}_{i,|} + 2\hat{b}^\dagger_{i,\circlearrowleft}\hat{b}^\dagger_{i,|}\hat{b}_{i,\circlearrowleft}\hat{b}_{i,|} + \hat{b}^\dagger_{i,\circlearrowleft}\hat{b}^\dagger_{i,\circlearrowleft}\hat{b}_{i,\circlearrowleft}\hat{b}_{i,\circlearrowleft}\right). \tag{C.7}$$

We will decompose the actuation of the Hamiltonian focusing on a local site i, centered on this site we can distinguish between local operators acting just on site i like the interaction terms and non-local terms acting in site i and neighboring sites $i-1$ or $i+1$ as in the hopping term. Based

on this we can express the hopping operators as the tensor product of identity operators acting on all the system sites except for the involved tunneling sites indices making a distinction between the left and right neighbors actuation with respect to the central site, as follows

$$\begin{aligned}\hat{b}^\dagger_{i,\bar{\sigma}}\hat{b}_{i+1,\bar{\sigma}} &\to \hat{I}_1 \otimes \cdots \otimes \hat{I}_{i-1} \otimes \hat{b}^\dagger_{i,\bar{\sigma}} \otimes \hat{b}_{i+1,\bar{\sigma}} \otimes \hat{I}_{i+2} \otimes \cdots \otimes \hat{I}_L \\ &\to \hat{I}_1 \otimes \cdots \otimes \hat{I}_{i-2} \otimes \hat{b}^\dagger_{i-1,\bar{\sigma}} \otimes \hat{b}_{i,\bar{\sigma}} \otimes \hat{I}_{i+1} \otimes \cdots \otimes \hat{I}_L \\ \hat{b}^\dagger_{i+1,\bar{\sigma}}\hat{b}_{i,\bar{\sigma}} &\to \hat{I}_1 \otimes \cdots \otimes \hat{I}_{i-1} \otimes \hat{b}_{i,\bar{\sigma}} \otimes \hat{b}^\dagger_{i+1,\bar{\sigma}} \otimes \hat{I}_{i+2} \otimes \cdots \otimes \hat{I}_L \\ &\to \hat{I}_1 \otimes \cdots \otimes \hat{I}_{i-2} \otimes \hat{b}_{i-1,\bar{\sigma}} \otimes \hat{b}^\dagger_{i,\bar{\sigma}} \otimes \hat{I}_{i+1} \otimes \cdots \otimes \hat{I}_L.\end{aligned}$$

While interaction terms can be grouped in $\hat{H}_{int}$ acting on local site i as

$$\hat{H}_{int} \to \hat{I}_1 \otimes \cdots \otimes \hat{I}_{i-1} \otimes \hat{H}^i_{int} \otimes \hat{I}_{i+1} \otimes \cdots \otimes \hat{I}_L. \tag{C.8}$$

Fixing i as the center of our system, it is possible to decompose the actuation of the Hamiltonian between the left and right subsystems as well as the center, with this distinction is possible to write a matrix representation of the Hamiltonian using a virtual basis defined by the combination of these three type of actuation for each operator, this process is depicted in Eq. (C.9)

$\leftarrow$ full	$\hat{I}$	0	0	0	0	0	0	0
$\leftarrow \hat{b}_{i-1,\circlearrowleft}$	$\mathbb{G}_{\circlearrowleft}\ \hat{b}^\dagger_{i,\circlearrowleft}$	0	0	0	0	0	0	0
$\leftarrow \hat{b}_{i-1,\vert}$	$\mathbb{G}_{\vert}\ \hat{b}^\dagger_{i,\vert}$	0	0	0	0	0	0	0
$\leftarrow \hat{b}_{i-1,\circlearrowright}$	$\mathbb{G}_{\circlearrowright}\ \hat{b}^\dagger_{i,\circlearrowright}$	0	0	0	0	0	0	0
$\leftarrow \hat{b}^\dagger_{i-1,\circlearrowleft}$	$\mathbb{G}_{\circlearrowleft}\ \hat{b}_{i,\circlearrowleft}$	0	0	0	0	0	0	0
$\leftarrow \hat{b}^\dagger_{i-1,\vert}$	$\mathbb{G}_{\vert}\ \hat{b}_{i,\vert}$	0	0	0	0	0	0	0
$\leftarrow \hat{b}^\dagger_{i-1,\circlearrowright}$	$\mathbb{G}_{\circlearrowright}\ \hat{b}_{i,\circlearrowright}$	0	0	0	0	0	0	0
$\leftarrow \hat{I}$	$\hat{H}^{\text{int}}_i$	$\hat{b}_{i,\circlearrowleft}$	$\hat{b}_{i,\vert}$	$\hat{b}_{i,\circlearrowright}$	$\hat{b}^\dagger_{i,\circlearrowleft}$	$\hat{b}^\dagger_{i,\vert}$	$\hat{b}^\dagger_{i,\circlearrowright}$	$\hat{I}$
	$\hat{I} \to$	$\hat{b}^\dagger_{i+1,\circlearrowleft} \to$	$\hat{b}^\dagger_{i+1,\vert} \to$	$\hat{b}^\dagger_{i+1,\circlearrowright} \to$	$\hat{b}_{i+1,\circlearrowleft} \to$	$\hat{b}_{i+1,\vert} \to$	$\hat{b}_{i+1,\circlearrowright} \to$	full $\to$

(C.9)

Where we defined $\mathbb{G}_{\bar{\sigma}} \equiv -J\mathbb{D}^{\bar{\sigma}}_{i,i+1}$ with $\bar{\sigma} \in \{\circlearrowleft, \vert, \circlearrowright\}$. Note that $\leftarrow$ full (full $\to$) corresponds to the collection of any local or non-local operators acting on any site of the left (right) subsystem. The term on the inferior left corner corresponds to the group of all local terms on the Hamiltonian.

The matrix in Ec. (C.9) corresponds to the local *MPO* element W_i for the Hamiltonian of our system. The interested reader is invited to perform the product $W_0 \times W_1 \times \cdots \times W_L \times W_{L+1}$ to

confirm it effectively reduces to the Hamiltonian of Ec. (2.35), remembering to take the auxiliary *MPO* elements, namely

$$W_0 = \begin{pmatrix} 0 & \cdots & \hat{I} \end{pmatrix}, \quad \text{and} \quad W_{L+1} = \begin{pmatrix} \hat{I} \\ \vdots \\ 0 \end{pmatrix}. \tag{C.10}$$

Bibliography

[1] Paul Dirac. *The Principles of Quantum Mechanics*. Oxford, Clarendon Press, 1930.

[2] E. Schrödinger. "Discussion of Probability Relations between Separated Systems." In: *Mathematical Proceedings of the Cambridge Philosophical Society* 31.4 (1935), pp. 555–563.

[3] E. Schrödinger. "An Undulatory Theory of the Mechanics of Atoms and Molecules." In: *Phys. Rev.* 28 (6 Dec. 1926), pp. 1049–1070. URL: https://link.aps.org/doi/10.1103/PhysRev.28.1049.

[4] A. Einstein. "Quantentheorie des einatomigen idealen Gases." In: *Albert Einstein: Akademie-Vorträge*. John Wiley Sons, Ltd, 2005, pp. 237–244. URL: https://onlinelibrary.wiley.com/doi/abs/10.1002/3527608958.ch27.

[5] E. A. Cornell and C. E. Wieman. "Nobel Lecture: Bose-Einstein condensation in a dilute gas, the first 70 years and some recent experiments." In: *Rev. Mod. Phys.* 74 (3 Aug. 2002), pp. 875–893. URL: https://link.aps.org/doi/10.1103/RevModPhys.74.875.

[6] K. B. Davis, M. -O. Mewes, M. R. Andrews, N. J. van Druten, D. S. Durfee, D. M. Kurn, and W. Ketterle. "Bose-Einstein Condensation in a Gas of Sodium Atoms." In: *Phys. Rev. Lett.* 75 (22 Nov. 1995), pp. 3969–3973. URL: https://link.aps.org/doi/10.1103/PhysRevLett.75.3969.

[7] Markus P. Hehlen. "Review of condensed matter laser cooling using electric-dipole-allowed transitions." In: *Journal of Luminescence* 252 (2022), p. 119270. URL: https://www.sciencedirect.com/science/article/pii/S0022231322005452.

[8] T.W. Hänsch and A.L. Schawlow. "Cooling of gases by laser radiation." In: *Optics Communications* 13.1 (1975), pp. 68–69. URL: https://www.sciencedirect.com/science/article/pii/0030401875901595.

[9] E. L. Raab, M. Prentiss, Alex Cable, Steven Chu, and D. E. Pritchard. "Trapping of Neutral Sodium Atoms with Radiation Pressure." In: *Phys. Rev. Lett.* 59 (23 Dec. 1987), pp. 2631–2634. URL: https://link.aps.org/doi/10.1103/PhysRevLett.59.2631.

[10] Shi-Guo Peng, Shina Tan, and Kaijun Jiang. "Manipulation of p-Wave Scattering of Cold Atoms in Low Dimensions Using the Magnetic Field Vector." In: *Phys. Rev. Lett.* 112 (25 June 2014), p. 250401. URL: https://link.aps.org/doi/10.1103/PhysRevLett.112.250401.

[11] Tomasz Sowiński and Miguel Ángel García-March. "One-dimensional mixtures of several ultracold atoms: a review." In: *Reports on Progress in Physics* 82.10 (Sept. 2019), p. 104401. URL: https://dx.doi.org/10.1088/1361-6633/ab3a80.

[12] V. S. Letokhov. "Generation of Light by a Scattering Medium with Negative Resonance Absorption." In: *Soviet Journal of Experimental and Theoretical Physics* 26 (Apr. 1968), p. 835.

[13] P.S. Jessen and I.H. Deutsch. "Optical Lattices." In: *Optical Lattices*. Ed. by Benjamin Bederson and Herbert Walther. Vol. 37. Advances In Atomic, Molecular, and Optical Physics. Academic Press, 1996, pp. 95–138. URL: https://www.sciencedirect.com/science/article/pii/S1049250X08600993.

[14] David R. Meacher. "Optical lattices-crystalline structures bound by light." In: *Contemporary Physics* 39.5 (1998), pp. 329–350. URL: https://doi.org/10.1080/001075198181847.

[15] C. Kittel. *Introduction to Solid State Physics*. Wiley, 2004. URL: https://books.google.co.jp/books?id=kym4QgAACAAJ.

[16] Subir Sachdev. "Quantum phase transitions." In: *Physics World* 12.4 (Apr. 1999), p. 33. URL: https://dx.doi.org/10.1088/2058-7058/12/4/23.

[17] Valeriia Bilokon, Elvira Bilokon, Mari Carmen Bañuls, Agnieszka Cichy, and Andrii Sotnikov. "Many-body correlations in one-dimensional optical lattices with alkaline-earth(-like) atoms." In: *Scientific Reports* 13.1 (June 2023). URL: http://dx.doi.org/10.1038/s41598-023-37077-1.

[18] Tomasz Sowi ński, Omjyoti Dutta, Philipp Hauke, Luca Tagliacozzo, and Maciej Lewenstein. "Dipolar Molecules in Optical Lattices." In: *Phys. Rev. Lett.* 108 (11 Mar. 2012), p. 115301. URL: https://link.aps.org/doi/10.1103/PhysRevLett.108.115301.

[19] Zijian Wang, Xu-Dong Dai, He-Ran Wang, and Zhong Wang. *Topologically Ordered Steady States in Open Quantum Systems*. 2023. URL: https://arxiv.org/abs/2306.12482.

[20] C. Broholm, R. J. Cava, S. A. Kivelson, D. G. Nocera, M. R. Norman, and T. Senthil. "Quantum spin liquids." In: *Science* 367.6475 (2020), eaay0668. URL: https://www.science.org/doi/abs/10.1126/science.aay0668.

[21] Piers Coleman. *Introduction to Many-Body Physics*. Cambridge University Press, 2015.

[22] Zhiyuan Wang and Kaden R. A. Hazzard. "Particle exchange statistics beyond fermions and bosons." In: *Nature* 637.8045 (Jan. 2025), pp. 314–318. URL: https://doi.org/10.1038/s41586-024-08262-7.

[23] J. J. Sakurai and Jim Napolitano. *Modern Quantum Mechanics*. 3rd ed. Cambridge University Press, 2020.

[24] T. D. Kühner and H. Monien. "Phases of the one-dimensional Bose-Hubbard model." In: *Phys. Rev. B* 58 (22 Dec. 1998), R14741–R14744. URL: https://link.aps.org/doi/10.1103/PhysRevB.58.R14741.

[25] Thomas G. Kiely and Erich J. Mueller. "Superfluidity in the one-dimensional Bose-Hubbard model." In: *Phys. Rev. B* 105 (13 Apr. 2022), p. 134502. URL: https://link.aps.org/doi/10.1103/PhysRevB.105.134502.

[26] Markus Greiner, Olaf Mandel, Tilman Esslinger, Theodor W. Hänsch, and Immanuel Bloch. "Quantum phase transition from a superfluid to a Mott insulator in a gas of ultracold atoms." In: *Nature* 415.6867 (Jan. 2002), pp. 39–44. URL: https://doi.org/10.1038/415039a.

[27] Ehud Altman, Kenneth R. Brown, Giuseppe Carleo, Lincoln D. Carr, Eugene Demler, Cheng Chin, Brian DeMarco, Sophia E. Economou, Mark A. Eriksson, Kai-Mei C. Fu, Markus Greiner, Kaden R.A. Hazzard, Randall G. Hulet, Alicia J. Kollár, Benjamin L. Lev, Mikhail D. Lukin, Ruichao Ma, Xiao Mi, Shashank Misra, Christopher Monroe, Kater Murch, Zaira Nazario, Kang-Kuen Ni, Andrew C. Potter, Pedram Roushan, Mark Saffman, Monika Schleier-Smith, Irfan Siddiqi, Raymond Simmonds, Meenakshi Singh, I.B. Spielman, Kristan Temme, David S. Weiss, Jelena Vu čkovi ć, Vladan Vuleti ć, Jun Ye, and Martin Zwierlein. "Quantum Simulators: Architectures and Opportunities." In: *PRX Quantum* 2 (1 Feb. 2021), p. 017003. URL: https://link.aps.org/doi/10.1103/PRXQuantum.2.017003.

[28] Maciej Lewenstein, Anna Sanpera, Veronica Ahufinger, Bogdan Damski, Aditi Sen(De), and Ujjwal Sen. "Ultracold atomic gases in optical lattices: mimicking condensed matter physics and beyond." In: *Advances in Physics* 56.2 (2007), pp. 243–379. URL: https://doi.org/10.1080/00018730701223200.

[29] Bryce Gadway and Bo Yan. "Strongly interacting ultracold polar molecules." In: *Journal of Physics B: Atomic, Molecular and Optical Physics* 49.15 (June 2016), p. 152002. URL: https://dx.doi.org/10.1088/0953-4075/49/15/152002.

[30] G Wendin. "Quantum information processing with superconducting circuits: a review." In: *Reports on Progress in Physics* 80.10 (Sept. 2017), p. 106001. URL: https://dx.doi.org/10.1088/1361-6633/aa7e1a.

[31] Kirubel Amsalu and Sivaprakasam Palani. "A review on photonics and its applications." In: *Materials Today: Proceedings* 33 (2020). International Conference on Nanotechnology: Ideas, Innovation and Industries, pp. 3372–3377. URL: https://www.sciencedirect.com/science/article/pii/S2214785320337457.

[32] C. Monroe, W. C. Campbell, L.-M. Duan, Z.-X. Gong, A. V. Gorshkov, P. W. Hess, R. Islam, K. Kim, N. M. Linke, G. Pagano, P. Richerme, C. Senko, and N. Y. Yao. "Programmable quantum simulations of spin systems with trapped ions." In: *Rev. Mod. Phys.* 93 (2 Apr. 2021), p. 025001. URL: https://link.aps.org/doi/10.1103/RevModPhys.93.025001.

[33] David J. Griffiths and Darrell F. Schroeter. *Introduction to Quantum Mechanics*. 3rd ed. Cambridge University Press, 2018.

[34] Yufang FENG and Yuyu ZHANG. "AN EFFECTIVE MAGNETIC FIELD OF SPIN-ORBIT COUPLING." In: *Physics and Engineering* 34.1 (2024), pp. 62–66. URL: https://www.sciopen.com/article/10.26599/PHYS.2024.9320110.

[35] Jonathan Schirmer, J. K. Jain, and C. -X. Liu. "Topological superconductivity induced by spin-orbit coupling, perpendicular magnetic field, and superlattice potential." In: *Phys. Rev. B* 109 (13 Apr. 2024), p. 134518. URL: https://link.aps.org/doi/10.1103/PhysRevB.109.134518.

[36] S.I. Mistakidis, A.G. Volosniev, R.E. Barfknecht, T. Fogarty, Th. Busch, A. Foerster, P. Schmelcher, and N.T. Zinner. "Few-body Bose gases in low dimensions—A laboratory for quantum dynamics." In: *Physics Reports* 1042 (2023). Few-body Bose gases in low dimensions—A laboratory for quantum dynamics, pp. 1–108. URL: https://www.sciencedirect.com/science/article/pii/S0370157323003162.

[37] Siddhesh C. Ambhire. *Symmetries in the many-body problems, a method to find its analytical solution, and Helium atom spectrum*. 2025. URL: https://arxiv.org/abs/2401.15019.

[38] Cintia T Willemyns and Claude Semay. "Some specific solutions to the translation-invariant N-body harmonic oscillator Hamiltonian." In: *Journal of Physics Communications* 5.11 (Nov. 2021), p. 115002. URL: https://dx.doi.org/10.1088/2399-6528/ac314e.

[39] Steven R. White. "Density matrix formulation for quantum renormalization groups." In: *Phys. Rev. Lett.* 69 (19 Nov. 1992), pp. 2863–2866. URL: https://link.aps.org/doi/10.1103/PhysRevLett.69.2863.

[40] Yuxuan Du, Xinbiao Wang, Naixu Guo, Zhan Yu, Yang Qian, Kaining Zhang, Min-Hsiu Hsieh, Patrick Rebentrost, and Dacheng Tao. *Quantum Machine Learning: A Hands-on Tutorial for Machine Learning Practitioners and Researchers*. 2025. URL: https://arxiv.org/abs/2502.01146.

[41] Yu-Hsueh Chen, Ke Hsu, Wei-Lin Tu, Hyun-Yong Lee, and Ying-Jer Kao. "Variational tensor network operator." In: *Phys. Rev. Res.* 4 (4 Nov. 2022), p. 043153. URL: https://link.aps.org/doi/10.1103/PhysRevResearch.4.043153.

[42] R. Penrose and W. Rindler. *Spinors and Space-time*. Cambridge monographs on mathematical physics 1. Cambridge University Press, 1984. URL: https://books.google.co.jp/books?id=CzhhKkf1xJUC.

[43] J. Ignacio Cirac, David Pérez-García, Norbert Schuch, and Frank Verstraete. "Matrix product states and projected entangled pair states: Concepts, symmetries, theorems." In: *Rev. Mod. Phys.* 93 (4 Dec. 2021), p. 045003. URL: https://link.aps.org/doi/10.1103/RevModPhys.93.045003.

[44] B. Pirvu, G. Vidal, F. Verstraete, and L. Tagliacozzo. "Matrix product states for critical spin chains: Finite-size versus finite-entanglement scaling." In: *Phys. Rev. B* 86 (7 Aug. 2012), p. 075117. URL: https://link.aps.org/doi/10.1103/PhysRevB.86.075117.

[45] Ho N. Phien, Guifré Vidal, and Ian P. McCulloch. "Infinite boundary conditions for matrix product state calculations." In: *Phys. Rev. B* 86 (24 Dec. 2012), p. 245107. URL: https://link.aps.org/doi/10.1103/PhysRevB.86.245107.

[46] Román Orús. "Advances on tensor network theory: symmetries, fermions, entanglement, and holography." In: *The European Physical Journal B* 87.11 (Nov. 2014), p. 280. URL: https://doi.org/10.1140/epjb/e2014-50502-9.

[47] Román Orús. "A practical introduction to tensor networks: Matrix product states and projected entangled pair states." In: *Annals of Physics* 349 (2014), pp. 117–158. URL: https://www.sciencedirect.com/science/article/pii/S0003491614001596.

[48] Edwin Stoudenmire and David J Schwab. "Supervised Learning with Tensor Networks." In: *Advances in Neural Information Processing Systems*. Ed. by D. Lee, M. Sugiyama, U. Luxburg, I. Guyon, and R. Garnett. Vol. 29. Curran Associates, Inc., 2016. URL: https://proceedings.neurips.cc/paper_files/paper/2016/file/5314b9674c86e3f9d1ba25ef9bb32895-Paper.pdf.

[49] Tin-Lun Ho. "Bose-Einstein Condensation in Dilute Gases." In: *Physics Today* 56.6 (June 2003), pp. 62–63. URL: https://doi.org/10.1063/1.1595060.

[50] Ramesh V. Pai, K. Sheshadri, and Rahul Pandit. "Phases and transitions in the spin-1 Bose-Hubbard model: Systematics of a mean-field theory." In: *Phys. Rev. B* 77 (1 Jan. 2008), p. 014503. URL: https://link.aps.org/doi/10.1103/PhysRevB.77.014503.

[51] Adilet Imambekov, Mikhail Lukin, and Eugene Demler. "Spin-exchange interactions of spin-one bosons in optical lattices: Singlet, nematic, and dimerized phases." In: *Phys. Rev. A* 68 (6 Dec. 2003), p. 063602. URL: https://link.aps.org/doi/10.1103/PhysRevA.68.063602.

[52] K. W. Mahmud and E. Tiesinga. "Dynamics of spin-1 bosons in an optical lattice: Spin mixing, quantum-phase-revival spectroscopy, and effective three-body interactions." In: *Phys. Rev. A* 88 (2 Aug. 2013), p. 023602. URL: https://link.aps.org/doi/10.1103/PhysRevA.88.023602.

[53] Sadamichi Maekawa, Takashi Kikkawa, Hiroyuki Chudo, Jun'ichi Ieda, and Eiji Saitoh. "Spin and spin current—From fundamentals to recent progress." In: *Journal of Applied Physics* 133.2 (Jan. 2020), p. 020902. URL: https://doi.org/10.1063/5.0133335.

[54] Amit Jamadagni and Hendrik Weimer. "Operational definition of topological order." In: *Phys. Rev. B* 106 (8 Aug. 2022), p. 085143. URL: https://link.aps.org/doi/10.1103/PhysRevB.106.085143.

[55] Tomohiro Hashizume, Jad C. Halimeh, and Ian P. McCulloch. "Hybrid infinite time-evolving block decimation algorithm for long-range multidimensional quantum many-body systems." In: *Phys. Rev. B* 102 (3 July 2020), p. 035115. URL: https://link.aps.org/doi/10.1103/PhysRevB.102.035115.

[56] Ashley Milsted, Jutho Haegeman, and Tobias J. Osborne. "Matrix product states and variational methods applied to critical quantum field theory." In: *Phys. Rev. D* 88 (8 Oct. 2013), p. 085030. URL: https://link.aps.org/doi/10.1103/PhysRevD.88.085030.

[57] B Pirvu, V Murg, J I Cirac, and F Verstraete. "Matrix product operator representations." In: *New Journal of Physics* 12.2 (Feb. 2010), p. 025012. URL: https://dx.doi.org/10.1088/1367-2630/12/2/025012.

[58] M. B. Hastings. "Entropy and entanglement in quantum ground states." In: *Phys. Rev. B* 76 (3 July 2007), p. 035114. URL: https://link.aps.org/doi/10.1103/PhysRevB.76.035114.

[59] Hans-Martin Rieser, Frank Köster, and Arne Peter Raulf. "Tensor networks for quantum machine learning." In: *Proceedings of the Royal Society A: Mathematical, Physical and Engineering Sciences* 479.2275 (2023), p. 20230218. URL: https://royalsocietypublishing.org/doi/abs/10.1098/rspa.2023.0218.

[60] Hua-Yu Dai, Jia-Rui Sun, and Yuan Sun. "On the emergence of gravitational dynamics from tensor networks." In: *Communications in Theoretical Physics* 75.8 (July 2023), p. 085402. URL: https://dx.doi.org/10.1088/1572-9494/acdd61.

[61] Y.-Y. Shi, L.-M. Duan, and G. Vidal. "Classical simulation of quantum many-body systems with a tree tensor network." In: *Phys. Rev. A* 74 (2 Aug. 2006), p. 022320. URL: https://link.aps.org/doi/10.1103/PhysRevA.74.022320.

[62] Ulrich Schollwöck. "The density-matrix renormalization group in the age of matrix product states." In: *Annals of Physics* 326.1 (2011). January 2011 Special Issue, pp. 96–192. URL: https://www.sciencedirect.com/science/article/pii/S0003491610001752.

[63] Lars Grasedyck and Wolfgang Hackbusch. In: *Computational Methods in Applied Mathematics* 11.3 (2011), pp. 291–304. URL: https://doi.org/10.2478/cmam-2011-0016.

[64] Toshiya Hikihara, Hiroshi Ueda, Kouichi Okunishi, Kenji Harada, and Tomotoshi Nishino. "Automatic structural optimization of tree tensor networks." In: *Phys. Rev. Res.* 5 (1 Jan. 2023), p. 013031. URL: https://link.aps.org/doi/10.1103/PhysRevResearch.5.013031.

[65] Steven L. Brunton and J. Nathan Kutz. "Singular Value Decomposition (SVD)." In: *Data-Driven Science and Engineering: Machine Learning, Dynamical Systems, and Control*. Cambridge University Press, 2019, pp. 3–46.

[66] Paulin de Schoulepnikoff, Oriel Kiss, Sofia Vallecorsa, Giuseppe Carleo, and Michele Grossi. "Hybrid ground-state quantum algorithms based on neural Schrödinger forging." In: *Phys. Rev. Res.* 6 (2 Apr. 2024), p. 023021. URL: https://link.aps.org/doi/10.1103/PhysRevResearch.6.023021.

[67] Angus J. Dunnett and Alex W. Chin. "Efficient bond-adaptive approach for finite-temperature open quantum dynamics using the one-site time-dependent variational principle for matrix product states." In: *Phys. Rev. B* 104 (21 Dec. 2021), p. 214302. URL: https://link.aps.org/doi/10.1103/PhysRevB.104.214302.

[68] Maarten Van Damme, Jutho Haegeman, Ian McCulloch, and Laurens Vanderstraeten. "Efficient higher-order matrix product operators for time evolution." In: *SciPost Phys.* 17 (2024), p. 135. URL: https://scipost.org/10.21468/SciPostPhys.17.5.135.

[69] Annika Völl and Stefan Wessel. "Spin dynamics of the bilinear-biquadratic $S = 1$ Heisenberg model on the triangular lattice: A quantum Monte Carlo study." In: *Phys. Rev. B* 91 (16 Apr. 2015), p. 165128. URL: https://link.aps.org/doi/10.1103/PhysRevB.91.165128.

[70] G. De Chiara, M. Lewenstein, and A. Sanpera. "Bilinear-biquadratic spin-1 chain undergoing quadratic Zeeman effect." In: *Phys. Rev. B* 84 (5 Aug. 2011), p. 054451. URL: https://link.aps.org/doi/10.1103/PhysRevB.84.054451.

[71] M S Bulakhov, A S Peletminskii, S V Peletminskii, and Yu V Slyusarenko. "Magnetic phases and phase diagram of spin-1 condensate with quadrupole degrees of freedom." In: *Journal of Physics A: Mathematical and Theoretical* 54.16 (Mar. 2021), p. 165001. URL: https://dx.doi.org/10.1088/1751-8121/abed16.

[72] A.S. Peletminskii, S.V. Peletminskii, and Yu.V. Slyusarenko. "SU(3) symmetry in theory of a weakly interacting gas of spin-1 atoms with Bose-Einstein condensate." In: *Physics Letters A* 384.31 (2020), p. 126798. URL: https://www.sciencedirect.com/science/article/pii/S0375960120306654.

[73] K. Rodríguez, A. Argüelles, A. K. Kolezhuk, L. Santos, and T. Vekua. "Field-Induced Phase Transitions of Repulsive Spin-1 Bosons in Optical Lattices." In: *Phys. Rev. Lett.* 106 (10 Mar. 2011), p. 105302. URL: https://link.aps.org/doi/10.1103/PhysRevLett.106.105302.

[74] Eran Sela, Alexander Altland, and Achim Rosch. "Majorana fermions in strongly interacting helical liquids." In: *Phys. Rev. B* 84 (8 Aug. 2011), p. 085114. URL: https://link.aps.org/doi/10.1103/PhysRevB.84.085114.

[75] Masataka Kakoi, Tatsuya Kaneko, Hirofumi Sakakibara, Masayuki Ochi, and Kazuhiko Kuroki. "Pair correlations of the hybridized orbitals in a ladder model for the bilayer nickelate

$La_3Ni_2O_7$." In: *Phys. Rev. B* 109 (20 May 2024), p. L201124. URL: https://link.aps.org/doi/10.1103/PhysRevB.109.L201124.